COMPUTATIONAL STUDY OF REACTIVE AND COKE-RESISTANT CATALYSTS

FOR THE DRY REFORMING REACTION OF METHANE

A Dissertation

by

SUPAREAK PRASERTHDAM

Submitted to the Office of Graduate and Professional Studies of
Texas A&M University
in partial fulfillment of the requirements for the degree of

DOCTOR OF PHILOSOPHY

Chair of Committee,	Perla B. Balbuena
Committee Members,	Jorge M. Seminario
	Benjamin A. Wilhite
	Hong-Cai Zhou
Head of Department,	M. Nazmul Karim

August 2018

Major Subject: Chemical Engineering

ABSTRACT

The dry reforming reaction of methane (DRR) is one of the solutions utilized to deal with the global warming via the catalyzed reaction of the main greenhouse gas: carbon dioxide (CO_2) with methane (CH_4), to produce the syngas of carbon monoxide (CO) and hydrogen (H_2). Although it is a promising process, catalyst deactivation via coking shortens the life of catalysts and increases the cost of catalyst regeneration/replacement, both of which are important concerns. Hence, the search for catalysts of high activity and coke-resistance is the main goal. In this work, we feature a two-step procedure comprising the analysis and design of active and coke-resistant Ni-based DRR catalysts by employing computational techniques. These techniques include density functional theory (DFT) coupled to the ratings concept developed as a catalysts screening tool. The approach aims to investigate reaction and coking schemes prior to the setup of design criteria for such catalysts. The ratings concept is introduced as a screening tool to identify active and stable DRR catalysts via the interpretation of stability and reactivity ratings (RT-S and RT-R). The concept was then extended for practical applications, where reliable predictions of coke formation and removal rates are demonstrated. Such predictions emerge from the interpretation of experimental apparent activation energy values of Pt and Rh supported catalysts. The predicted trend of coking agrees well with the trend of coke deposition measured via temperature-programmed hydrogenation and temperature-programmed oxidation of these catalysts. Furthermore, optimal operating conditions are determined. Four strategies are proposed based on four types of DRR catalysts. In addition, the surface transformation entailing the interchange between Ni metallic, oxide and carbide during the DRR is studied

since the control over these transformations is proposed to be the key factor for tuning the performance of DRR catalysts. Ternary contour plots are used for determining reactive and coke-resistant surface compositions. It is concluded that the surface composition for coke-resistant Ni-based DRR catalysts should consist of less than 10 % carbide and at least 75 % metallic. Finally, the design procedure and criteria for high performance DRR catalysts are discussed, where the control synthesis towards the Ni(111) as the dominant surface together with the control of surface transformation from metallic to carbide is proposed to be the main key.

DEDICATION

For my hardworking dad, cheerful mom, lovely aunt, adorable girlfriend, and *mi mejor profesora*.

ACKNOWLEDGEMENTS

First of all, I would like to express my gratitude to my kind advisor, Prof. Perla B. Balbuena who has guided me through this route of Ph.D. study since I first came to the group in 2014. Moreover, this dissertation would not be complete without supports from the thesis committee: Prof. Jorge M. Seminario and Dr. Benjamin A. Wilhite from the department of chemical engineering and Prof. Hongcai Zhou from the department of chemistry.

For always being supportive either directly or indirectly, I would like to say "thank you" and "I love you" a thousand times to the most important people of my life my dad, Prof. Piyasan, my mom, Asso. Prof. Vichitra, my aunt, Asso. Prof. Malinee and my girlfriend, Miss Jiaranai. Without my dad, I would end up studying medicine or architecture and would not come this far in this Ph.D. route heading towards an academic job in Thailand. Without my mom inspiring me with various kinds of musical instrument, I would have lost my creativity and mental flexibility. Without my aunt training me with discipline, the perspective in "working hard enough" would have been abandoned. Without my girlfriend, the world would be just black and white, hence, I have learned the art of selflessness and forgiveness. I would like to thank all of my friends from the chemical engineering department, Prof. Balbuena's research group (Mr. Luis Eduardo Camacho Forero and Mr. Saul Perez Beltran for his teaching on simulation software), Thai friends in the Thai Student Association at Texas A&M University (TSA) (Miss Chaiyaporn Suranetinai for her guidance on the dissertation format and Mr. Phakpoom Chinprutthiwong for his consultation on how to code loops and iterations), and finally and the department faculty and staff for writing another memorable page of my book of life at Texas A&M University.

CONTRIBUTORS AND FUNDING SOURCES

NOMENCLATURE

DRR	Dry Reforming Reaction of methane
DFT	Density Functional Theory
VASP	Vienna ab initio simulation package
PAW	Projected Augmented Wave pseudopotentials
GGA	Generalized Gradient Approximation
PBE	Perdew-Burke-Ernzerhof
cNEB	Climbing Nudge Elastic Band method
TST	Transition State Theory
ZPE	Zero-point energy
PSSH	Pseudo Steady State Hypothesis
mari	most abundant reactive intermediate
k_i	rate constant of elementary step i
k_{app}	apparent rate constant for selected reaction
θ_i	Surface coverage of species i
P_i	Partial pressure of gaseous species i
y_i	mole fraction of gaseous species i
k_B	Boltzmann constant
h	Planck constant
T	Temperature
%RT	percent rating unit in the rating scale
RT-S	stability rating (%RT)

RT-R	reactivity rating (%RT)
RT-S_i	Stability Rating of elementary step i
RT-R_i	Reactivity Rating of elementary step i
RT-S_{avg}	Average Stability Rating of elementary step i
RT-R_{avg}	Average Reactivity Rating of elementary step i
Φ	Rating scale ratio in the unit of eV / %RT
SS	Stability Surface
RS	Reactivity Surface
E_{ads}	Adsorption Energy
E_a	Activation Energy (barrier)
$E_{a,app}$	Apparent Activation Energy (barrier)
$E_{a,app,CH4}$	Apparent activation energy of the CH_4 decomposition reaction
$\log(r_{CH4})$	log rate of CH_4 consumption reaction
$\log(r_{Cgen,total})$	log rate of coke formation from CH, CO and Boudouard reaction
$\log(r_{Cgen,CH})$	log rate of coke formation from CH
$\log(r_{Cgen,CO})$	log rate of coke formation from CO
$\log(r_{Cgen,BD})$	log rate of coke formation from Boudouard reaction
TCP	Ternary contour plot

TABLE OF CONTENTS

LIST OF FIGURES

LIST OF TABLES

1. INTRODUCTION

1.1. Dissertation organization

The main goal of this dissertation is to provide the design guidelines of high performance Ni-based catalysts for the dry reforming reaction of methane based on the analysis of such catalysts via computational methods. The dissertation was organized into two parts: the analysis and design of the catalyst. Prior to these two parts, the background knowledge and computational techniques used in this study were laid out in chapter 1 and 2, respectively. In chapter 1, the nature of the dry reforming reaction of methane (DRR) was brought up, where the catalysts used in the process together with the obstacles arising from catalyst deactivation via coking were also discussed. Furthermore, the characteristics of coke, which is the main deactivation substance, and coking process that caused catalyst deactivation were described in detail. By the end of the chapter, the objective was stated. In the 2nd chapter, all computational methods employed were illustrated from theory to application; also, the construction of catalyst models was depicted in the chapter. The analysis part began in chapter 3 which introduced the ratings concept developed as the catalyst screening tool, in which its derivation and application were described. The extension of this concept for the interpretation of experimental data is demonstrated subsequently in chapter 4. Next, chapter 5 discussed the effects of reaction conditions proposed for the optimal operating conditions of four main types of a DRR catalyst, whereas chapter 6 studied the surface transformation of the catalyst during the DRR, in which this transformation was shown to be the key controlling the catalyst performance. The catalyst design part was summarized in chapter 7, wherein all the strategies towards active-stable DRR catalysts

discussed in previous chapters were used to set up the design criteria and to propose the guidelines for the design of active and coke-resistant Ni-based DRR catalysts. In the last chapter, conclusions were made in addition to the recommendation of possible improvements that can be achieved in future works.

1.2. The dry reforming reaction of methane

The dry reforming reaction of methane (DRR) is of high interest due to the conversion of CO_2, one of the most harmful greenhouse gases causing global warming, via the reaction with methane to generate syngas products of CO and H_2 of ratio 1:1 illustrated in the equation below.

$$CH_4(g) + CO_2(g) \rightleftarrows 2CO(g) + 2H_2(g) \qquad \text{Equation 1}$$

$$CH_4(g) + 2* \rightleftarrows CH_3* + H* \qquad \text{Equation 2}$$

$$CH_3* + * \rightleftarrows CH_2* + H* \qquad \text{Equation 3}$$

$$CH_2* + * \rightleftarrows CH* + H* \qquad \text{Equation 4}$$

$$CH* + * \rightleftarrows C* + H* \qquad \text{Equation 5}$$

$$CO_2(g) + 2* \rightleftarrows CO* + O* \qquad \text{Equation 6}$$

$$C* + O* \rightleftarrows CO* + * \qquad \text{Equation 7}$$

$$H* + H* \rightleftarrows H_2(g) + 2* \qquad \text{Equation 8}$$

$$CO* \rightleftarrows CO(g) + * \qquad \text{Equation 9}$$
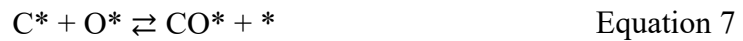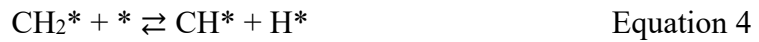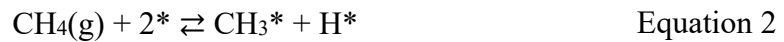
These products are reactants for an important process, the Fischer-Tropsch (FT) which is used in the production of higher hydrocarbons[1, 2]. In general, a mechanism of the dry reforming reaction of methane (DRR) involves the activation of reactants, which are CH_4 (Equation 2) and CO_2 (Equation 6), CH_x dissociation (Equation 3 to Equation 5) and the CO formation from atomic C and O (Equation 7)[3-6]. However, CH_x coupling with O or OH are possible but can be neglected since they are found to be thermodynamically and kinetically less favorable [3, 6], while the CH-O coupling reaction is ignored in this work to simplify the model leaving alone only the oxidation of the carbon atom (Equation 7). Therefore, a mechanism for the DRR is considered to proceed in 8 steps shown in Equation 2 to Equation 9.

The main problem for the DRR is catalyst deactivation via coking causing active site blockage leading to pore blockage of catalyst and reactor, respectively[1]. Hence, the life of the DRR catalysts is shortened adding the cost for their regeneration and/or replacement. As a result, the identification of reactive and coke-resistant DRR catalysts is crucial and challenging. The Ni-based catalysts are considered to be one of the good DRR candidates, showing a promising reactivity and moderate stability in the DRR, where various approaches have been attempted to improve its stability since the coking level was found to be high [7-11]. In general, to describe reactivity, the conversion of a selected reactant for an interested reaction is measured[12, 13]. On stability, the determination of coke-resistant properties is not well verified. For example, the measurement of the total amount of coke deposition obtained from the temperature programmed oxidation (TPO) technique[14] is not an appropriate representative for coke-resistance because not all kinds of deposited coke deactivate the catalyst and the differentiation of non-deactivating and deactivating cokes is

3

complicated[15]. For these reasons, Bartholomew proposed that coke-resistance should be described by the deactivation rate defined as the net rate of any coke formation elementary reactions competing with coke removal elementary reactions (e.g., CH* + * $\rightleftarrows$ C* + H* versus C* + O* $\rightleftarrows$ CO* + *)[16], where the coke-resistant catalyst should possess higher rate of coke removal than coke formation. Although the method would be useful for the evaluation, gathering of experimental data needs a lot of time and effort. Accordingly, computational methods are proposed as complements for characterization and screening tools for reactive and stable catalysts[17-19]. The next subsection discusses the deactivation substance in the coking process, the coke together with its deactivation processes.

1.3. Coke and deactivation via coking

The main catalyst deactivation scheme found in the DRR is coking, which is caused by the "coke", a carbonaceous substance of various sizes: it can range from as small as an atomic carbon to the heavy polyaromatic forms (e.g., whisker, carbon nanotube-like, or film) and origins (it can be generated either from the decomposition of hydrocarbons or the CO-disproportionation reaction (Boudouard reaction))[20]. On the type of coke during DRR, α-coke (C_α) is formed either by CH_4 or CO_2 dissociations[3-6]. Moreover, on Ni-based catalysts, C_α is considered a starting point towards the formation of heavier hydrocarbons, larger coke such as amorphous film (C_β), whiskers (C_V), graphitic carbon (C_C) or lead to carbide ($C\gamma$) formation[20-22]. Thus, the higher coke formation can be illustrated from the following equation (C* is the adsorbed carbon atom on the surface representing α-coke (C_α), while (C-C)* is the higher coke comprising 2 atoms of carbon formed via reaction in Equation 10, and * is the vacant active site).

4
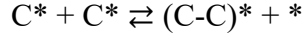
$$C^* + C^* \rightleftarrows (C\text{-}C)^* + * \qquad\qquad \text{Equation 10}$$

On the catalyst deactivation caused by coking, diverse types of coke affect the catalyst differently. In the case of amorphous film type (C_β), it would gradually deactivate the catalyst by blocking the active sites as it grows[20]. In the case of whisker type coke (C_v), although the surface is not deactivated, a more severe situation was found where the whisker grows and causes the catalyst breakdown [16].

1.4. Objective

Due to the serious deactivation issues arising from coking, the search for coke-resistant and still reactive Ni-based catalysts is of high interest. In this work, we employed computational techniques for the determination and screening of reactive and coke-resistant catalysts for improved DRR process performance. An approach combining DFT calculations with the ratings concept which was developed as a screening tool for high-performance DRR catalysts is proposed. The ratings concept is based on the interpretation of the stability and reactivity ratings (RT-S and RT-R), to analyze for reactivity and coke-resistant properties of catalysts. The study was carried out and organized into two parts: the analysis and the design. For the analysis section, the development of the ratings concept was performed together with the application of the concept. For the practical use of the concept, the extension of the concept for the direct utilization of the experimental parameters was demonstrated and used to predict the trend of coke formation rate. In addition, for the identification of the optimal DRR operating conditions, four strategies were proposed based on classifications of DRR catalysts via the ratings concept. Furthermore, the catalyst surface transformation that is proposed to be the key that governs the reactivity and stability of the Ni-based DRR

catalysts, was studied in order to understand the relationship between such transformation and DRR performance. In the design part, criteria and strategies towards the control over reactivity and coke-resistance are constructed based on the conclusions from the analysis section.

2. METHODOLOGY AND COMPUTATIONAL DETAILS

2.1. Density functional theory (DFT)

2.1.1. History of DFT

According to the fact proposed by Louis de Broglie[23] that all matter (molecules, atoms, nuclei or electrons) can act both as wave and particle, the description of any material by an equation that describes the behavior of wave should be possible. Thus, the "wave equation" was derived by Erwin Schrödinger[24] as shown in the following equation ($\hat{H}$ = Hamiltonian operator, Ψ = wave function, and E = energy of the system) in order to describe the wave-like behavior of any system.

$$\hat{H}\Psi = E\Psi \qquad\qquad \text{Equation 11}$$

The equation captures the quantum behavior of the system by describing the evolution of the wave function (Ψ) over time. In addition, a useful form of the equation is the time-independent form shown in the equation below, in which the Born-Oppenheimer approximation is held considering that the mass nuclei are much heavier than electrons, hence, the positions of the nuclei can be assumed fixed and the wave function (Ψ) only depends on the positions of electrons ($\mathbf{r}$).

$$\hat{H}(\mathbf{r})\Psi(\mathbf{r}) = E\Psi(\mathbf{r}) \qquad\qquad \text{Equation 12}$$

Solving this equation for simple systems such as the hydrogen atom is possible, but for applications to materials science and other related fields, the large number of atoms in the system would cause the equation to be too complex to solve. As a result, many first-principles methods were introduced to deal with this "many-body problem", e.g., Hartree-Fock (HF) but still, they are limited to small or too simplified systems far from

describing the actual materials[25]. With respect to this, the concept of utilizing the electron density as the main variable instead of treating electrons individually was proposed and shown to make calculations for larger systems possible[26]. The method lies on two theorems proposed by Hohenberg and Kohn which can be described as follows[27].

Theorem 1: the ground-state energy obtained from the Schrödinger's equation is a functional of the electron density

Theorem 2: the full solution to the Schrödinger's equation is the electron density that minimizes the overall functional

Note that a functional is a function of a function since it takes a function as an input argument. The first theorem implies that the electron density at ground state can determine both the energy and the wavefunction of the ground-state. Hence, in order to solve the Schrödinger's equation, one must find the right electron density where the solution is the energy functional of the system. Thereafter, the second theorem provides the definition of the right electron density which is the electron density that minimizes the energy functional of the system.

Although up to now there is a definition for the right electron density, the question arises: how to obtain the right electron density? Fortunately, this was made possible by Kohn and Sham, who proposed an iterative procedure to solve a set of equations, where each of which yields a solution of a one-electron wave function depending on only three spatial variables. The equation is referred to as the Kohn-Sham equation shown below.

$$\left[-\frac{\hbar^2}{2m}\nabla^2+V(\mathbf{r})+V_H(\mathbf{r})+V_{XC}(\mathbf{r})\right]\psi_i(\mathbf{r})=\varepsilon_i\psi_i(\mathbf{r}) \qquad \text{Equation 13}$$

8

V is the interaction between an electron and the atomic nuclei, V_H is a Coulomb repulsion between the electron considered in the Kohn-Sham equation and the total electron density and also to itself as the electron itself is also included in the total electron density, and the final term V_{XC} is the exchange and correlation contributions which include all the quantum effects, that must usually be approximated since its actual form is not known. Their proposed procedure to obtain the electron density can be summarized as follows.

1. Input the initial guessed electron density ($n(\mathbf{r})$)

2. Solve the Kohn-Sham equation for the wave function ($\psi_i(\mathbf{r})$)

3. Calculate the Kohn-Sham electron density ($n_{KS}(\mathbf{r})$) from the solved wave function ($\psi_i(\mathbf{r})$) via the following equation, where the factor of 2 appears to represent the electron spins (up and down or +0.5 and -0.5) according to Pauli exclusion principle[28].

$$n_{KS}(\mathbf{r}) = 2 \sum_i \psi_i^*(\mathbf{r})\psi_i(\mathbf{r}) \qquad \text{Equation 14}$$

4. Check if the solved Kohn-Sham electron density ($n_{KS}(\mathbf{r})$) converges to the value of the guessed electron density ($n(\mathbf{r})$). If converged, this Kohn-Sham electron density is the ground-state electron density

Nevertheless, an important point needed to be clarified in the Kohn-Sham equation is the exchange-correlation term ($V_{XC}(\mathbf{r})$). Since its exact form of exchange-correlation functional is unknown, this term could only be estimated, and various functionals have been proposed. One of them is the local density approximation (LDA) which considers the density of the electron gas to be spatially uniform at all locations and to be same as the local electron density illustrated via the following equation.

$$V_{XC}^{LDA}(\mathbf{r})=V_{XC}^{electron\ gas}[n(\mathbf{r})] \hspace{2cm} \text{Equation 15}$$

Although yielding satisfactory results, the valence electron density in various bulk materials is not constant but vary along the direction pointing outward the center of the atom. Thus, the generalized gradient approximation (GGA) was introduced, adding the gradient in the electron density ($\nabla n(\mathbf{r})$) term representing the variation of the electron density as a function of the distance described in the equation below.

$$V_{XC}^{GGA}(\mathbf{r})=V_{XC}[n(\mathbf{r}), \nabla n(\mathbf{r})] \hspace{2cm} \text{Equation 16}$$

A final note to the exchange-correlation functional is that, since our work applied the DFT in the field of catalysis, we chose GGA functional as it includes the non-uniformity of electron density found in most bulk materials, thus this should represent well the catalysts.

Now that all the ingredients for the DFT setup have been prepared, in the next subsection, we will show the components needed to complete a DFT calculation of a system.

2.1.2.   Components of DFT calculations

In this section, we define the components needed for a successful DFT calculation, in other words, a well-converged DFT calculation, where the solution obtained numerically can approximate the real solution of the Schrödinger's equation. For the catalyst's surface comprise many metal atoms, it is convenient to reduce the calculation size by taking the advantage of the periodicity of the solids, by which the following steps are followed[25].

1. The bulk system is reduced to a "supercell" comprised of several unit cells; then, periodic boundary conditions are applied to replicate the supercell representing the actual material surface.

2. Transform the supercell from the real space into the "reciprocal space", defined in the first Brillouin zone. In this zone, the wave vector (**k**) and reciprocal lattice vector (**G**) are used to represent the wave function ($\phi_k(\mathbf{r})$) which satisfies the Bloch equation shown below.

$$\Phi_k(\mathbf{r})=\exp(i\mathbf{k}\cdot\mathbf{r})u_k(\mathbf{r}) \qquad \text{Equation 17}$$

In addition, the $u_k(\mathbf{r})$ is the cell periodic with the same periodicity as the potential, while the $\exp(i\mathbf{k}\cdot\mathbf{r})$ is the plane wave and the **k** is the wave vector of the reciprocal space, thus solving sets of the Schrödinger's equation for each value of **k** is regarded as the plane-wave calculation.

3. The irreducible Brillouin zone (IBZ) is obtained by reducing the first Brillouin zone via symmetry operation of rotation and inversion.

4. A finite number of **k**-points are selected on the IBZ before all the properties are obtained. Note on this **k**-point sampling that, one of the most used methods is the Monkhorst-Pack method which generates an evenly spaced k-point grid on the entire IBZ, and the method is generally incorporated into many DFT codes.

The next step for the DFT calculation is the selection of the energy cutoff value. As the cell periodic term in the Bloch's equation includes the plane wave of various energies, the wave function solutions would be infinite, hence, the consideration of the plane wave with energy lower than some specific energy called "cutoff energy" is applied and shown to be reliable since the low energy plane waves are more important to the solution than the higher ones as we would describe the system at ground-state not excited-state.

The last component is the use of the pseudopotential approach on the system. First, electrons are classified into core and valence electrons, in which the electronic structure of

core electrons is assumed unchanged at all times, thus the wave function of the core electrons is smoothened by substituting the strong ionic potential in core zone by the pseudopotential. Now that the oscillatory behavior of the core electron wave function has been smoothened, the plane-wave calculation can be carried out. In this work, the projector augmented wave method (PAW) is utilized since it is more suitable for extended solids [29].

2.1.3. Computational details for DFT calculations in this work

The spin-polarized periodic DFT calculations were performed via the Vienna ab initio simulation package (VASP)[30-33], in which self-consistent algorithms were used to solve the Kohn-Sham equations. The Projector Augmented Wave pseudopotentials (PAW)[29] was utilized to construct basis functions describing the core electrons, while the valence electrons were described by plane wave basis sets of a cutoff energy of 450 eV for all systems. The exchange-correlation functional was described within the generalized gradient approximation (GGA) by Perdew, Burke, and Ernzerhof (PBE)[34, 35]. The Brillouin zone integration was constructed through a Monkhorst-Pack [36] grid of 4x4x1 sampling for all slab models. The first order Methfessel-Paxton smearing method [37] of 0.2 eV smearing width was applied for the partial occupancies with convergence criteria of 10^{-4} and 10^{-3} eV for successive electronic and ionic steps, respectively. For the Ni oxide, the Hubbard-U correction approach[38] was utilized onto the GGA-PBE above, where the difference between the Hubbard parameter (U) and the exchange parameter (J) is defined as U_{eff}, in which this work U_{eff} of 5.4 eV was used referring to the suggested value for NiO[38-43]. For the partially oxidized slab model, which has both the metallic and oxide parts of Ni, the metallic part is treated with normal GGA-PBE, while the oxide part is treated

with GGA-PBE plus the Hubbard U correction. Note that the U correction is done on the Ni atoms that bond to the nearby oxygen.

2.2. Determination of the activation energy

In order to determine the activation energy for an elementary reaction, one must first obtain the structures of reactant and product by the optimization via DFT calculation. Next, the minimum energy pathway (MEP) for the reaction of interest must be verified, in which the search for MEP utilizes the technique of the nudged elastic band calculation (NEB)[25]. The technique starts by mapping initial guessed structures of the images between the first and final structure of the reaction of interest onto the potential energy surface (PES). The PES describes the reaction energy pathway between reactants and products. Thereafter, these images are moved by applying a force that pushes them towards their zero-force configurations, while the fictitious spring force is applied to each image in order to evenly spaced them. This is done until the MEP is found and the transition state is assigned to the image situated at the saddle point. However, sometimes the calculation converges but there is no image at the saddle point. Due to this, the revised version of the technique was proposed by Henkelman et al.[44, 45] which is called "climbing nudge elastic band method (cNEB)", where one image is chosen to be at the saddle point by inverting the true force along the tangent of the highest energy image. In this work, the cNEB technique [44, 45] was applied using 6 images between the initial and final images to obtain the activation energy for the selected elementary steps. The setup is the same as in our previous work of a cluster model[46] where the initial and final images were obtained from the adsorbates at their most stable adsorption sites.

2.3. Slab model construction
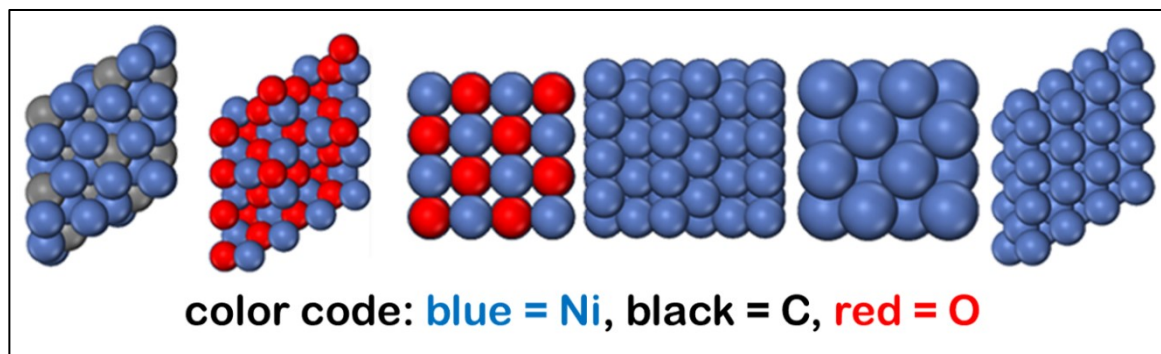
Figure 1 Slab models in top-view from left to right representing Ni₃C(001), O-terminated NiO(111)-p(2x2), NiO(100), Ni(211), Ni(100), and Ni(111) of Ni DRR catalyst

The slab models (Figure 1) representing the Ni catalyst during the DRR are constructed as metallic, carbide and oxide phases of Ni. The metallic Ni is modeled via Ni(111), Ni(211) and Ni(100) facets. Slabs consist of 5 layers cleaved from the optimized bulk Ni reported elsewhere[47, 48]. For the carbide, a Ni-terminated Ni₃C(001) of a 9-Ni-C-layer slab was constructed, where the surface was cleaved from the optimized Rhombohedral R-3Ch (hexagonal) bulk system[49, 50]. The oxide phase is represented by NiO(100) and NiO(111)-p(2x2), an O-terminated 6-Ni-O-layer slab with the assumption of the octopolar reconstructed surface that is reported to be the most stable NiO(111) surface[51-53].

14

2.4. Microkinetic modeling

Table 1 Elementary steps and rate equations of the 8-step DRR mechanism

Step i	Elementary step i	Rate equation of step i
1	$CH_{4(g)} + 2* \rightleftarrows CH_3* + H*$	$r1 = k_1 y_{CH4}\theta_*^2 - k_{-1}\theta_{CH3}\theta_H$
2	$CH_3* + * \rightleftarrows CH_2* + H*$	$r2 = k_2\theta_{CH3}\theta_* - k_{-2}\theta_{CH2}\theta_H$
3	$CH_2* + * \rightleftarrows CH* + H*$	$r3 = k_3\theta_{CH2}\theta_* - k_{-3}\theta_{CH}\theta_H$
4	$CH* + * \rightleftarrows C* + H*$	$r4 = k_4\theta_{CH}\theta_* - k_{-4}\theta_C\theta_H$
5	$CO_{2(g)} + 2* \rightleftarrows CO* + O*$	$r5 = k_5 y_{CO2}\theta_* - k_{-5}\theta_{CO}\theta_O$
6	$C* + O* \rightleftarrows CO* + *$	$r6 = k_6\theta_C\theta_O - k_{-6}\theta_{CO}\theta$
7	$H* + H* \rightleftarrows H_{2(g)} + 2*$	$r7 = k_7\theta_H^2 - k_{-7}y_{H2}\theta^2$
8	$CO* \rightleftarrows CO_{(g)} + *$	$r8 = k_8\theta_{CO} - k_{-8}y_{CO}\theta$
DRR	$CH_{4(g)} + CO_{2(g)} \rightleftarrows 2H_{2(g)} + 2CO_{(g)}$	$r_{DRR} = r_1+r_2+r_3+r_4+r_5+r_6+2r_7+2r_8$

Table 2 Elementary steps and rate equations of the 3-step Boudouard (RBD) and reverse-Boudouard reaction (RBD)

Step i**	Elementary step i	Rate equation of step i
8 reverse	$CO_{(g)} + * \rightarrow CO*$	$r_{8R} = k_{-8}y_{CO}\theta_*$
6 reverse	$CO* + * \rightarrow C* + O*$	$r_{6R} = k_{-6}\theta_{CO}\theta_*$
5 reverse	$CO* + O* \rightarrow CO_{2(g)} + 2*$	$r_{5R} = k_{-5}\theta_{CO}\theta_O$
8 forward	$CO* \rightarrow CO_{(g)} + *$	$r_{8F} = k_8\theta_{CO}$
6 forward	$C* + O* \rightarrow CO* + *$	$r_{6F} = k_6\theta_C\theta_O$
5 forward	$CO_{2(g)} + 2* \rightarrow CO* + O*$	$r_{5F} = k_5 y_{CO2}\theta_*^2$
Boudouard	$2CO_{(g)} + * \rightarrow CO_{2(g)} + C*$	$r_{BD} = 2(r_{8R}) + r_{6R} + r_{5R}$
reverse-Boudouard	$CO_{2(g)} + C* \rightarrow 2CO_{(g)} + *$	$r_{RBD} = 2(r_{8F}) + r_{6F} + r_{5F}$

Note that step i refers to the forward and reverse step of DRR step in Table 1, where r_i equals to r_{iF} - r_{iR} (for example, $r_5 = r_{5F} - r_{5R}$), k_i is the rate constant of step i (negative i

means reverse of step i), y_i is the mole fraction of gaseous species i equals its partial pressure over total pressure (p_i/p_{total}), and θ_i is the surface coverage of surface species i, where for the subscript, the * (asterisk) designated free site on the surface, while others are as designated.

The Matlab software was utilized in solving all sets of equations, where the 8-step mechanism shown in Table 1 was considered. In this study, the DRR mechanism includes the Boudouard and reverse-Boudouard reactions illustrated in Table 2 as additional coke formation and removal reactions[54]. In addition, the assumptions that the surface reaction is the rate limiting step and the mass transfer of reactants and their diffusion through the catalyst pore together with the adsorption and desorption steps is fast were followed. The derivation of the mechanism and assumptions were already discussed in the Introduction. The transition state theory (TST) was applied on each elementary step to determine the forward and reverse rate constants: k_i and k_{-i}, respectively from the Eyring equation [55] shown in Equation 18.

$$k_i = \frac{k_B T}{h} e^{\frac{-\Delta G^{\ddagger,\circ}}{k_B T}}$$
Equation 18

The term k_i is the rate constant of the elementary step i, k_B is the Boltzmann constant equals to 8.617×10^{-5} eV•K^{-1}, h is the Planck constant which is equal to 4.135×10^{-15} eV•s, T is the reaction temperature (K), and $\Delta G^{\ddagger,\circ}$ is standard molar Gibbs free energy changes from the initial state of elementary step i to its transition state which can be calculated via $\Delta G^{\ddagger,\circ} = \Delta G^{\circ}$ (Transition state) - ΔG° (reactant). In this work, the zero-point energy (ZPE), entropy (S) and internal energy (U) contributions were considered. From the Eyring equation, $\Delta G^{\ddagger,\circ}$ is the change of standard molar Gibbs free energy between the transition state (TS) and the initial state (IS) or the reactant, that can be represented in another form as illustrated in the equation below.

$$\Delta G^{\ddagger,\circ} = \Delta E_{DFT} + \Delta E_{ZPE} + \Delta U^\circ - T\Delta S^\circ \qquad \text{Equation 19}$$

The term ΔE_{DFT} is the activation energy of the desired elementary step obtained directly from the DFT calculation, ΔE_{ZPE} is the zero-point energy calculated by the following equation.

$$\Delta E_{ZPE} = \sum \frac{h\nu_i}{2} \qquad \text{Equation 20}$$

The ν_i is the vibrational frequency obtained via the vibrational frequency calculation, h is the Planck's constant, ΔU° is the standard molar internal energy which includes standard molar vibrational, translational and rotational internal energies, finally, ΔS° is the standard molar entropy which includes standard molar vibrational, translational and rotational entropies. The equation for the calculation of the standard molar translational, rotational and vibrational internal energies and entropy can be found in references [3, 6, 56].

The pseudo steady-state hypothesis (PSSH) was applied to determine surface coverages, in which the absence of "most abundant reactive surface species" (mari) is considered resulting in the following site balance equation.

$$\theta_{CH3} + \theta_{CH2} + \theta_{CH} + \theta_H + \theta_{CO} + \theta_C + \theta_O + \theta_* = 1 \qquad \text{Equation 21}$$

For $CO_{(g)}$ and $H_{2(g)}$, they are assumed to be in the adsorption-desorption equilibrium as reported elsewhere[6, 57], where surface coverages for H and CO can be derived as follows.

$$\theta_H = \theta_* \sqrt{y_{H_2} \frac{k_{-7}}{k_7}} \qquad \text{Equation 22}$$

17

$$\theta_{CO}=\theta_* y_{CO} \frac{k_{-8}}{k_8} \qquad \text{Equation 23}$$

For catalyst's reactivity, the total rate of the DRR was chosen as shown in Equation 24, while for stability, coking reactions described by coke formation from CH and CO shown in Equation 25 and coke removal via H and O in Equation 26, respectively.

$$r_{DRR} = r_1 + r_2 + r_3 + r_4 + r_5 + r_6 + (2)(r_7) + (2)(r_8) \qquad \text{Equation 24}$$

$$r_{Cgen} = (k_4\theta_{CH}\theta_*) + (k_{-6}\theta_{CO}\theta) + (k_{-8}y_{CO}\theta_* + k_{-6}\theta_{CO}\theta_* + k_{-5}\theta_{CO}\theta_O) \qquad \text{Equation 25}$$

$$r_{Crem} = (k_{-4}\theta_C\theta_H) + (k_6\theta_C\theta_O) + (k_8\theta_{CO} + k_6\theta_C\theta_{O*} + k_5y_{CO2}\theta_*^2) \qquad \text{Equation 26}$$

The reaction condition used in this work is 1000 K and CO_2/CH_4 feed ratio of 1.0. To avoid over-counting in the mechanism, these assumptions were followed. For step 5, 6 and 8 in Table 1 (DRR mechanism), they are shared by both the DRR and the Boudouard reactions, where each of the steps is assumed to contribute equally to both reactions. Hence, the following rates for DRR, Boudouard, and reverse-Boudouard reactions can be expressed in Equation 27, Equation 28 and Equation 29, accordingly.

$$r_1 + r_2 + r_3 + r_4 + [(0.5)(r_5)] + [(0.5)(r_6)] + 2r_7 + [(0.5)(2r_8)] \qquad \text{Equation 27}$$

$$[(0.5)(r_{5R})] + [(0.5)(r_{6R})] + [(0.5)(2r_{8R})] \qquad \text{Equation 28}$$

$$[(0.5)(r_{5F})] + [(0.5)(r_{6F})] + [(0.5)(2r_{8F})] \qquad \text{Equation 29}$$

3. CATALYST PERFORMANCE EVALUATION VIA AN APPLICATION OF THE RATINGS CONCEPT[*]

3.1. Derivation of the ratings concept

In order to explore high-performance DRR catalysts, one needs to be able to screen various catalysts based on some specific criteria associated only with the dry reforming reaction of methane. As a result, the ratings concept is introduced as a screening tool for reactive and stable DRR catalysts based on the comparison of catalyst performance. Fundamentally, in any comparison, three main components that should be considered are (1) the parameters to be compared, (2) the scale where parameters are compared on, and (3) single or multiple points of reference used in the scale setup. Thus, the comparison of the DRR catalyst performance via the ratings concept can be illustrated via the setup of a scale analogous to a thermometer scale. In the Celsius thermometer scale, the components used in the setup are: (1) the temperature of a system (a parameter), (2) the Celsius scale (the scale) which reads temperatures in degrees Celsius (°C) on a 2-reference point scale of constant step size of 100°C/100 steps (or 1°C/step), and (3) the freezing point of $H_2O_{(l)}$ at 0°C and the boiling point of $H_2O_{(l)}$ at 100°C as the lower and upper references points, respectively. Likewise, the setup of our ratings concept has (1) the performance of the DRR catalysts as a parameter in the comparison, (2) the scale called "the ratings scale" that interprets the performance of the DRR catalysts in the unit of percent rating (%RT) with constant step size, in which the value of step size is further discussed later in the report and (3) the

---

reference point is the performance of the reference catalysts set to 100 %RT to which other catalysts are benchmarked. In this way, the catalysts with ratings above 100 are considered to be better than the reference catalyst.

However, the description of the performance should not only include reactivity but also the stability since coking is one of the main factors affecting the DRR performance. Hence, the ratings concept determines how reactive and stable the catalyst should be in order to achieve a high rate of reaction while suppressing coke formation via two parameters: reactivity rating (RT-R) and stability rating (RT-S) derived from the following procedure.

1. Select the reference catalyst which will be the benchmark for others to compare with. In our work, the Ni(111) surface was chosen and represented by the slab model.

2. Designate the reactivity (set Y) and stability (X1 and X2) sets having activation energies of specific elementary steps accounting for reactivity and stability of the catalyst of interest as follows:

    2.1. Set X1, the coke removal reaction set integrated by the activation energies of:

    2.1.1. reverse elementary step 4 ($C^* + H^* \rightarrow CH^* + *$)

    2.1.2. forward elementary step 6 ($C^* + O^* \rightarrow CO^* + *$)

    2.2. Set X2, the coke formation reaction set integrated by the activation energies of:

    2.2.1. forward elementary step 4 ($CH^* + * \rightarrow C^* + H^*$)

    2.2.2. reverse elementary step 6 ($CO^* + * \rightarrow C^* + O^*$)

    2.3. Set Y, the reactivity set integrated by the activation energies of:

    2.3.1. forward elementary step 1 ($CH_{4(g)} + 2^* \rightarrow CH_3^* + H^*$)

    2.3.2. forward elementary step 5 ($CO_{2(g)} + 2^* \rightarrow CO^* + O^*$)

2.3.3.   forward elementary step 7 ($H* + H* \rightarrow H_{2(g)} + 2*$)

3. Rate each set of the selected catalysts with respect to the reference catalyst via either the direct or reverse rating scale calculated via the following equations.

$$\text{direct rating scale (for set X2): } \frac{E_a - E_{a,0}}{RT - RT_0} = +|\Phi| \qquad \text{Equation 30}$$

$$\text{reverse rating scale (for sets X1 and Y): } \frac{E_a - E_{a,0}}{RT - RT_0} = -|\Phi| \qquad \text{Equation 31}$$

The value of Φ is the rating scale ratio which is the step size of the rating scale which is set to 0.015 eV / 1 %RT. For set X1 (coke removal) and Y (reactivity), the lower the E_a for these sets the easier for the system to remove coke and activate reactants, while for set X2 (coke formation), the higher the E_a the more difficult for the system to form coke. As a result, higher reactivity rating (RT-R) would result from lower E_a of set Y (reactivity), while higher stability rating (RT-S) came from lower E_a of set X1 (coke removal) yet higher E_a of set X2 (coke formation). Hence, the direct rating scale is used on set X2, while the reverse rating scale is used on set X1 and Y. Then, the rating (RT) of the selected catalyst is determined. (RT of the reference system are assigned to be 100 %)

4. Calculate the average reactivity rating (RT-R_{avg}) from the arithmetic mean of stability rating in set Y and for average stability ratings (RT-S_{avg}), stability ratings in set X1∪X2 are averaged as the following equations (n = number of all elementary reactions in set Y and m = number of all elementary reactions in set X1∪X2):

$$\text{RT-R}_{avg} = \frac{1}{n} \sum_{i=1}^{n} \text{RT-R}_i \qquad \text{Equation 32}$$

$$RT\text{-}S_{avg} = \frac{1}{m} \sum_{i=1}^{m} RT\text{-}S_i \qquad \qquad \text{Equation 33}$$

Table 3 Ranking of screened catalysts

Rank	Rate of reaction on RS*	Location on SS**	Rate in coke removal/formation zone on SS**
1st	High	Coke removal	High
2nd	Low	Coke removal	High
3rd	High	Coke removal	Low
4th	Low	Coke removal	Low
5th	High	Coke formation	Low
6th	Low	Coke formation	Low
7th	High	Coke formation	High
8th	Low	Coke formation	High
*RS = reactivity surface as in Figure 2(a)			
**SS = stability surface as in Figure 2(b) and (c)			

5. Construct the reactivity surface (RS) and stability surface (SS) shown in Figure 2, where the reactivity surface (RS) is the plot of rate of total rate of DRR as a function of $RT\text{-}R_{avg}$ and $RT\text{-}S_{avg}$, while the stability surfaces (SS) are the plots of rate of coke formation and coke removal both as functions of $RT\text{-}R_{avg}$ and $RT\text{-}S_{avg}$. Additionally, Figure 2(b) depicts the coke formation zone, which has coke formation rate higher than coke removal rate, while Figure 2(c) illustrates the coke removal zone, where the coke formation is less than the removal.

22
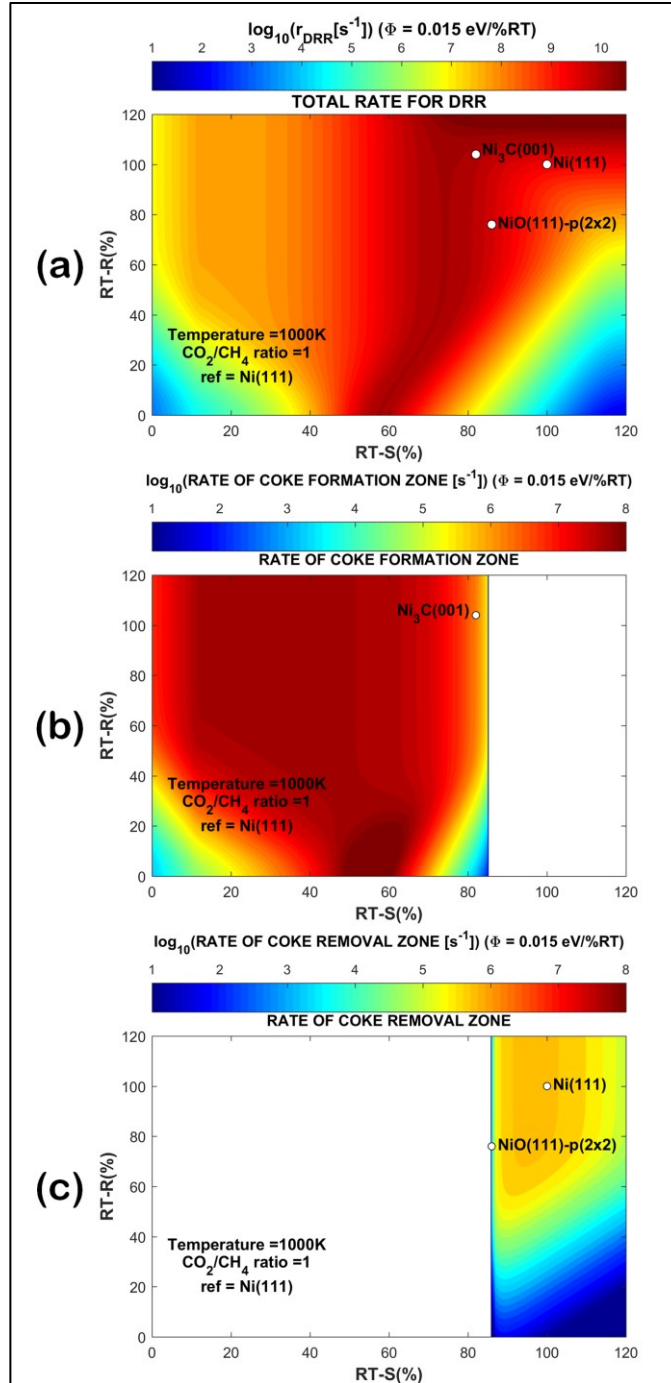
Figure 2 Log plot of (a) reactivity surface (RS) which is the total rate of DRR (Equation 24), (b) stabiltiy surface (SS) describing the rate of all coke formation reactions in coke formation zone (Equation 25 - Equation 26) and (c) stabiltiy surface (SS) describing the rate of all coke removal reactions in the coke removal zone (Equation 26 - Equation 25) as a function of reactivity rating (RT-R) and stability rating (RT-S) at T = 1000 K, P_{CH4} = P_{CO2} = 1 bar, P_{H2} = P_{CO} = 0.1 bar

6. Plot x and y coordinate of the selected catalysts onto RS and SS as x = RT-S$_{avg}$ and y = RT-R$_{avg}$. Note that for both RS and SS, the RT-S$_{avg}$ and RT-R$_{avg}$ of the reference catalyst are set to 100 %RT as described previously.

7. Analyze the reactivity surface (RS) for the rate of reaction and screen for reactive catalysts, where a high rate of reaction means high reactivity.

8. Analyze the stability surfaces (SS) and locate if the selected catalyst is in the coke formation zone or in the coke removal zone together with its coke formation/coke removal rate at the location. For the stable catalyst criteria, the catalyst should locate in the coke removal zone exhibiting a rate of coke removal higher than the formation.

9. Rank the performance of the screened catalysts as shown in Table 3 based on reactivity and stability criteria.

The catalyst reactivity interpreted from the reactivity surface (RS), Figure 2(a) can be summarized as follows. The increase in stability rating (x-axis: RT-S) would increase the rate of reaction, where the rate reaches the first maximum region at RT-S around 60 %RT for any value of reactivity rating (y-axis: RT-R). But, if RT-S is too high, the rate of reaction will decline unless a higher reactivity rating (RT-R) value could be achieved, in which case the rate of reaction will rise again to the second maximum point at RT-R $\in$ [110, 120] and RT-S $\in$ [70, 120]. The results suggest that RT-S should not be too low or high for the system to have higher reactivity, while RT-R should be high to avoid low reaction rate whether RT-S is high or not. The meaning of the RT-S and RT-R indexes on reactivity can be understood as follows:

1. As RT-S reflects coke formation and coke removal steps, the suggested value of RT-S should be not too low or high, such that when compared to the reference

catalyst of Ni(111), the activation barrier for coke formation should be lower, while the coke removal should be more difficult in order to promote reaction.

2. For RT-R representing the ability to activate CH_4 and CO_2, the suggested high RT-R value could be interpreted as easy activation of these DRR reactants increasing the rate of reaction.

For analyses on the stability of the catalyst via the stability surfaces (SS), Figure 2(b) and (c), the following observations were found.

1. Coke formation zone is located at low stability rating (x-axis: RT-S < 85). The highest coke formation rate could be found at RT-S $\in$ [50, 60] and RT-R $\in$ [0, 20]. This explains that to arrive at low coke formation rate, either very high or very low stability rating (RT-S) combined with low reactivity rating (RT-R) is needed to drive the system into the low coke formation at the bottom left and right corner of this coke formation zone. Furthermore, to avoid coke formation at all, high enough RT-S is needed to push the system into the coke removal zone where the rate of coke formation of this zone is inhibited by high coke removal rate. This denotes that a very difficult activation of CH_4 and CO_2 (corresponds to the RT-R) would lower the rate of coke formation only if the E_a for coke formation and removal steps are either too high or low resulting in the lowest coke formation rate at the bottom left and right corner.

2. Coke removal zone can be found at high stability rating (x-axis: RT-S > 85), where the coke removal rate increases as the reactivity rating (RT-R) increases up to the maximum coke removal at RT-S $\in$ [90, 100] and RT-R $\in$ [70, 120]. This suggests that for the system to be in the coke removal zone, coke formation steps should be

difficult while coke removal should be easy, in which the E_a of both steps corresponds to the RT-S of more than 85 %RT. In addition, when the RT-S is high enough that a system is in the coke removal zone, easier activation of CH_4 and CO_2 (RT-R increases) would enhance the stability by promoting the rate of coke removal, where the maximum rate could be achieved when RT-S $\in$ [90, 100] and RT-R is more than 70 %RT.

The analysis of both reactivity and stability to determine the region where the system has high reaction rate while attaining high coke-resistant property is discussed. The first location where the most reactive catalyst could be found is at the first maximum rate of reaction area at RT-S $\approx$ 60 %RT for any value of RT-R. At this point although the rate of reaction is maximum, the rate of coke formation is also the highest as illustrated in Figure 2(b).
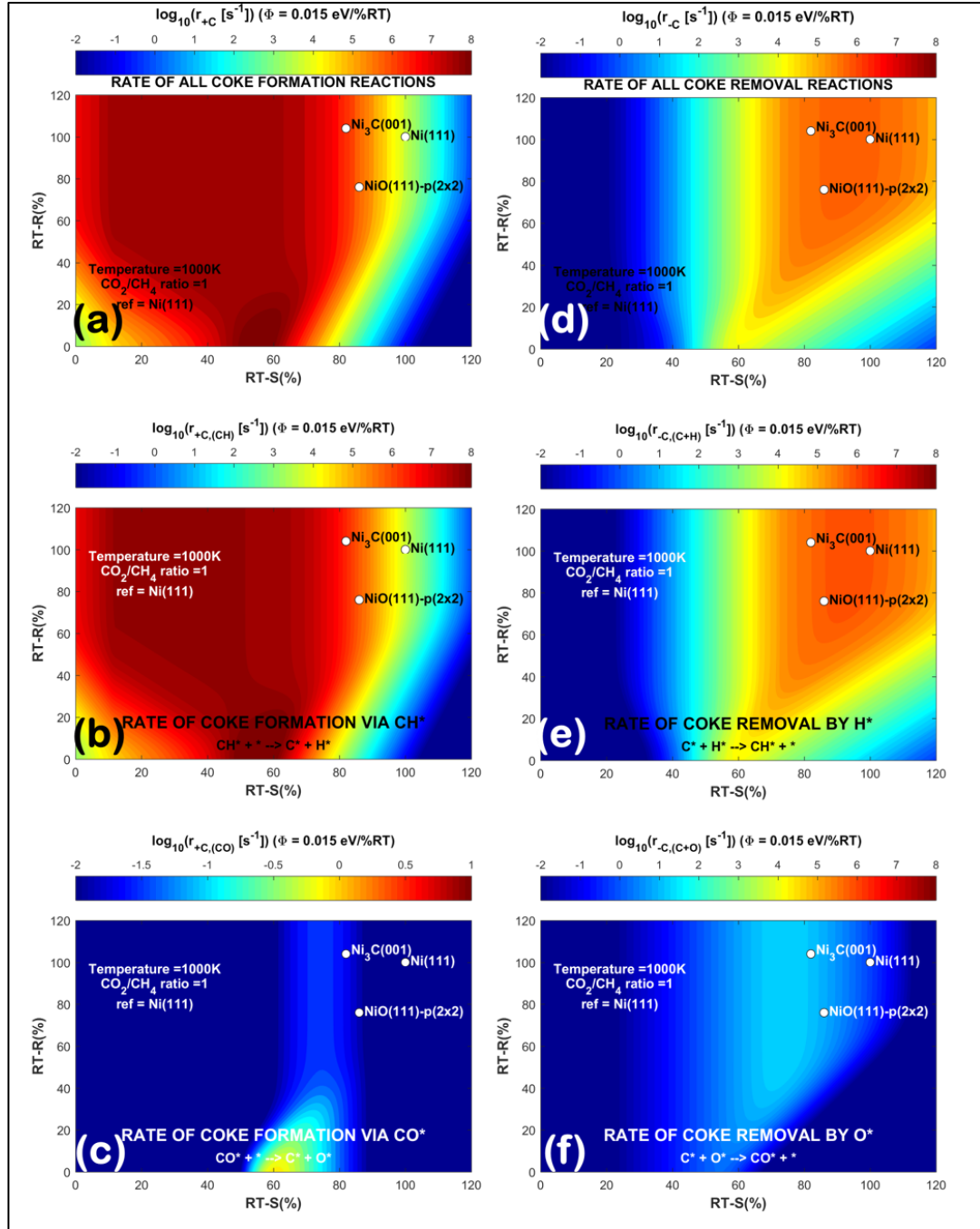
Figure 3 Log rate plot of (a) combined C formation from CH* and CO* species (1st and 2nd terms of Equation 25) , (b) C formation from CH* species (1st term of equation 7), (c) C formation from CO* species (2nd term of equation 7), (d) combined C removal via H* and O* species (1st and 2nd terms of Equation 26), (e) C removal via H* species (1st term of Equation 26) and (f) C removal via O* species (2nd term of Equation 26) all as a function of reactivity rating (RT-R) and stability rating (RT-S) at T = 1000 K, $P_{CH4} = P_{CO2} = 1$ bar, $P_{H2} = P_{CO} = 0.1$ bar

As a result, this area would lead to reactive but low coke-resistance catalysts. In addition, the second location for the reactive catalysts is found at the top right corner where both RT-S and RT-R are very high. In this area, the rate of reaction is as high as the first maximum rate but the coke-resistance is enhanced as the coke removal rate is highest in this area depicted in Figure 2(c). Thus, this zone could be an ideal zone for reactive and coke-resistant DRR catalysts. Further analyses of coke formation as combined and individual rate from CH* and CO* species are illustrated in Figure 3(a), (b) and (c), while the combined and individual rate of coke removal via H* and O* are included in Figure 3(d), (e) and (f), that can be summarized as follows. For coke formation, CH* is the main coke producer as it contributes to most of the coke formation rate suggesting that the control over the coke formation from CH* species could help lowering coke deposition. Besides, the major coke removal process is the hydrogenation via H* species, while the oxidation via O* is much less pronounced. This informs that the coke removal via the hydrogenation process could be an effective way to enhance the coke-resistant property for DRR catalyst.

The effects of temperature on reactivity and stability are incorporated via the Eyring equation (Equation 18) and can be summarized as follows. The increase in temperature not only intensifies the DRR rate but it also promotes the rate of coke formation together with the rate of coke removal. The phenomena are normal since high temperature would magnify the rate constant leading to the increase in the rate. In addition, the coke formation and coke removal zone are much less affected by the changes in temperature. This suggests that if the location of a given catalyst is in the coke formation zone, the increase in temperature would worsen the catalytic performance as a result of high coke formation. On the other hand, if the catalyst is located in the coke removal zone, its stability would be enhanced at high

temperature since the rate of coke removal has been promoted. In summary, the location of the catalyst plays a key role in determining whether their performance would be depressed or improved at increased temperature. A complete analysis of the temperature effects will be presented in future work.

To gain a better understanding on the use of the rating concept, in the next section, the concept is applied to describe reaction and coking schemes in the Ni–Ni$_3$C–NiO catalyst system during the DRR.

3.2. Application of the ratings concept

In this section, the rating concept is employed to describe the reaction and coking schemes on the Ni catalyst system consisting of 3 phases: metallic, carbide and oxide of Ni represented by slab models of Ni(111), Ni$_3$C(001) and NiO(111)-p(2x2) in Figure 4. This setting illustrates the DRR catalyst, in which these phases contribute differently to reactivity and stability of the system. It is known that Ni$_3$C that forms during the DRR by the reaction with carbon generated either from CH$_4$ or CO$_2$[58], promotes not only the main reaction but also the coke formation[59-62], while NiO formed by the reaction with CO$_2$ is shown to exhibit coke resistance properties, extending the life of catalysts[63].
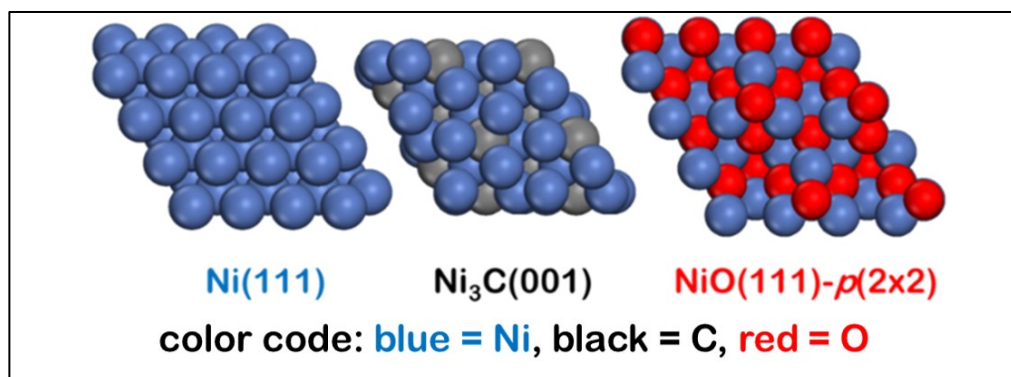
Figure 4 Slab models in top-view from left to right representing NiO(111)-p(2x2), Ni₃C(001) and Ni(111) of Ni DRR catalyst

Table 4 Activation energy and ratings of Ni-Ni3C-NiO catalyst system

set	reaction	Ni(111)		Ni₃C(001)		NiO(111)-p(2x2)	
		E_a (eV)	RT (%RT)	E_a (eV)	RT (%RT)	E_a (eV)	RT (%RT)
Y	$CH_{4(g)} + 2* \rightleftarrows CH_3* + H*$	0.89	100	0.71	113	0.91	100
Y	$H* + H* \rightleftarrows H_{2(g)} + 2*$	0.92	100	1.00	94	1.65	51
X1	$CH* + * \rightleftarrows C* + H*$	1.38	100	1.14	87	1.47	110
X1	$CO* + * \rightleftarrows C* + O*$	3.43	100	2.92	99	*N/D	*N/D
X2	$C* + H* \rightleftarrows CH* + *$	0.76	100	1.02	86	1.40	61
X2	$C* + O* \rightleftarrows CO* + *$	1.23	100	2.25	56	*N/D	*N/D
	RT-S$_{avg}$ (set X1 & X2)	100		82		86	
	RT-R$_{avg}$ (set Y)	100		104		76	
*N/D : not determined							

Prior to the evaluation of the reactivity and stability of these phases, the average reactivity rating (RT-R$_{avg}$) and average stability rating (RT-S$_{avg}$) are determined from the procedure in the previous section as shown in Table 4 and plotted onto Figure 2(a), (b) and (c). The reactivity interpreted through the RS index in Figure 2(a) illustrates that when the

carbide phase forms, the system shifts into a more reactive zone which agrees with the experiments that the carbide phase in the system would catalyze the main reaction with even higher magnitude[61, 62]. On the other hand, NiO showed a small increase in the rate of reaction compared to the pure Ni. On the stability assessment, both coke formation and coke removal ability of the system were analyzed via the index of SS in Figure 2(b) and (c). It is clarified that the reason why the carbide phase contributed to coking is that it is located in a coke formation zone, where coke formation is stronger than coke removal. In contrast, as the NiO formed the stability does not decrease since the system is still in the coke removal zone with a considerably high coke removal rate.

Further examination of individual coke production and coke removal processes are shown in Figure 3(a) to (f). It is found that the high rate of coke formation on Ni_3C came from both CO* and CH*. Also, Ni_3C showed the lowest combined rate of coke removal among three Ni phases. Note that although the coke removal rate via oxidation by O* (Figure 3(f)) for Ni_3C is the highest, it could not gain any stability since the magnitude of this oxidation step is too low compared to its coke formation. For NiO, it exhibits coke-resistant property similar to the Ni phase as it is located at the maximum coke removal rate in the coke removal zone in Figure 2(c). From these results, the reaction and coking schemes are proposed as follows: When the reaction proceeds on the fresh catalyst of metallic Ni, the carbide phase of Ni_3C starts to form decreasing the stability by shifting the system into the coke formation zone promoting the rate of coke formation. Meanwhile, the oxide phase of NiO formed would increase the system's reactivity and preserves the stability as it is in the coke removal zone with high coke removal rate.

It is clearly shown from the analysis that the control of Ni_3C formation is crucial since this would lower the coke formation, thus improving stability. In addition, adding NiO phase to the system would be beneficial although it does not show significant improvement in stability compared to the pure metallic Ni phase. However, this oxide phase does not transform directly into a low coke-resistant carbide phase but it may convert into metallic Ni via the reaction between a surface O atom and coke formed by CO_2 [63]. In this way, as NiO transforms first to Ni, both reactivity and coke-resistance could be regenerated again extending the life of the Ni-based catalyst. In summary, the proposed guideline for reactive and stable Ni-based DRR catalyst is based on the idea that the system should have the oxide phase of Ni in order to gain coke-resistant property, while the control over the formation of carbide phase is one of the keys for higher coke-resistance.

3.3. Conclusions

The rating concept was demonstrated to be a useful tool to screen for reactive and stable DRR catalysts via the analysis of reactivity rating (RT-R) and stability rating (RT-S) of the catalyst of interest through indexes on the reactivity and stability surfaces (RS and SS) representing by the total rate of DRR and rate of coke formation-removal, respectively. Moreover, the application of the rating concept on the Ni-NiO-Ni_3C catalyst system to describe the reaction-deactivation scheme shows good agreement with experimental data[59-63], where carbide phase formed via the reaction between the fresh catalyst and coke is accounted for lower stability as it promotes coke formation although the system becomes more reactive, while the oxide phase could preserve the stability of the system by its high coke removal rate; hence, suppressing coke formation. Ultimately, the guidelines for reactive

and stable Ni-based DRR catalyst suggest that there should be enough amount of NiO phase in the catalyst to preserve coke-resistant property, while the Ni_3C phase should be restricted in order to lower coke formation, enhance stability.

4. EXTENSION OF THE RATINGS CONCEPT FOR EXPERIMENTAL DATA

INTERPRETATION[*]

4.1. Derivation of the extended ratings concept

An extension of the ratings concept is proposed in order to use directly the experimental data of the DRR catalysts and predict the stability in terms of coke formation rate. The apparent activation energies ($E_{a,app}$) are of interest since most of experimental works measure and report them to represent the reactivity of the DRR catalysts. However, to utilize this experimental data, the correlation between $E_{a,app}$ and the rate of reaction must be derived. To start with, as in experimental reports, the rate description from the power rate law of DRR is generally described by Equation 34, where a and b are the reaction order of CH_4 and CO_2, accordingly[64].

$$\text{rate} = k_{app} \, (P_{CH4})^a \, (P_{CO2})^b \qquad \text{Equation 34}$$

In addition, the dependence on the CO_2 pressure can be neglected [4] and the DRR rate is assumed to depend solely on the CH_4 pressure as shown in Equation 35.

$$\text{rate} = k_{app} \, (P_{CH4})^a \qquad \text{Equation 35}$$

From this power rate law, the apparent rate constant (k_{app}) is described using the transition state theory via the Eyring equation in Equation 18. So, the rate of reaction becomes Equation 36.

$$\text{rate} = \left(\frac{k_B T}{h} e^{\frac{\Delta S^{\ddagger}}{k_B}} \right) e^{\frac{-E_{a,app}}{k_B T}} \, (P_{CH4})^a \qquad \text{Equation 36}$$

The assumption of zero entropy change was made in order to simplify Equation 36 to arrive at the log rate of CH_4 consumption (log r_{CH4}) as a function only of the apparent activation energy of CH_4 consumption reaction ($E_{a,app,CH4}$) in Equation 37. This assumption is made based on the fact that the entropy of the adsorbed initial reactants and transition state structures may be considered approximately the same.

$$\log_{10}(r_{CH_4}) = \frac{-E_{a,app,CH4}}{[k_B T \log_e(10)]} + \left[\log_e\left(\frac{k_B T}{h}(P_{CH4})^a\right)\right] \qquad \text{Equation 37}$$

The determination of the coke formation rate can be achieved via using one of the calculated ratings (either RT-S or RT-R) and the rate obtained from Equation 37 to locate the position of the catalysts of interest on the reactivity surface map. This map is a contour plot of the DRR rate in Equation 24 as a function of both RT-S and RT-R. After knowing the RT-S and RT-R indexes of that location, the rate of coke formation can be determined by reading the indexes on the stability surface map. This map is similar to that of the reactivity surface but the rate of the contour plot is the combined rate of coke formation in Equation 25 instead.

The application of this concept extension will be shown in the next section which demonstrated the prediction of coke formation rate on four Pt supported catalysts: Pt/SiO_2, Pt/TiO_2, Pt/Cr_2O_3 and Pt/ZrO_2 and also in the case of Rh supported catalysts: Rh/TiO_2, Rh/Al_2O_3, Rh/MgO and Rh/SiO_2.

4.2. Application of the extended ratings concept

In this section, we extended the ratings concept to predict the rate of coke formation from experimental data on Pt supported catalysts: Pt/SiO_2, Pt/Cr_2O_3, Pt/TiO_2 and Pt/ZrO_2,

and Rh supported catalysts: Rh/TiO_2, Rh/Al_2O_3, Rh/MgO and Rh/SiO_2, in which the trend of predicted rates of coke formation and the trend of measured carbon deposition from temperature-programmed hydrogenation and oxidation (TPH and TPO) [64-66] are compared. The experimental setup at 723 K (for Pt supported catalysts) and 773 K (for Rh supported catalysts) with CO_2/CH_4 feed ratio of 1 and methane pressure of 1 bar reported for these catalysts are used to construct the reactivity and stability surfaces (RS and SS) as shown in Figure 5 to Figure 9. It should be noted that since for the microkinetic calculation, the surface reaction as rate limiting step is assumed, our model represents the reaction scheme where the mass transfer limitation is neglected. Thus, the predicted values for rate of coke formation and removal would be more precise on the experimental system with high space velocity, where the measured activation energy (E_a) could be considered totally derived from the rate of a surface reaction without any interference of mass diffusion, pore diffusion limitations.

As in the ratings concept, the stability surface (SS) captures the information of coke formation and coke removal at any indexes of stability (RT-S) and reactivity (RT-R) ratings, where the indexes are unique for each catalyst. This means that (1) the rate of coke formation on the stability surface, (2) the stability rating (RT-S) and (3) the reactivity rating (RT-R) are dependent on each other. So, knowing two of these parameters, the third one can be determined. However, the direct utilization of the experimental parameters to predict the reactivity and stability of the DRR catalysts is not fully developed. Thus, we propose the extension of our ratings concept to directly evaluate the experimental data and predict the rate of coke formation, in which the prediction via RT-R and rate of reaction when the reference catalyst is Ni(111) is implemented.

The approach utilizes the apparent activation energy of CH4 consumption ($E_{app,CH4}$) as the only experimental input to our extended ratings concept. The procedure to predict the rate of coke formation is as follows. Note that the term E_a is an apparent activation energy of the catalyst of interest, $E_{a,0}$ is an activation energy of the reference catalyst, RT is calculated reactivity rating (RT-R) or stability rating (RT-S) of the selected catalyst, and RT_0 is the reactivity rating (RT-R) or stability rating (RT-S) of the reference catalyst which is always assigned to be 100 %RT, Φ is rating scale ratio which is a real positive value describing how much the value of E_a in eV would change when rating (RT) changes by 1 %RT which in this work Φ is 0.015 eV / %RT.

$$\text{reverse rating scale (for set X1 and Y): } \frac{E_a\text{-}E_{a,0}}{RT\text{ -}RT_0}=-|\Phi| \qquad \text{Equation 38}$$

1. Choose a reference catalyst where in this case is the Ni(111) slab model depicted in Figure 1 on page 14.

2. Calculate the reactivity rating (RT-R) from the known apparent activation energy of CH4 consumption ($E_{app,CH4}$)[64, 65] via the reverse rating scale in Equation 38 (which is the same as Equation 31 on page 21.

3. Calculate the log rate of CH4 consumption ($\log_{10}(r_{CH4})$) from $E_{app,CH4}$ via the relation developed in Equation 37 on page 35.

4. Determine the location of the catalyst of interest by reading the reactivity surface (RS) using the calculated RT-R and $\log_{10}(r_{CH4})$ in step 2 and 3, respectively.

5. Read the stability rating (RT-S) from the determined location in step 4.

6. Obtain the rate of total coke formation also with the individual coke formation rate from CH*, CO* and the Boudouard reaction for the catalyst from the stability surface (SS) via the obtained indexes of RT-S and RT-R determined in the previous step.

Therefore, the extended ratings concept is setup, wherein the next subsection the predicted rates of coke formation for all catalysts are determined and the reliability test of these predicted values will be demonstrated on two case studies which are Pt and Rh supported catalysts, accordingly.

4.2.1. Case study 1: Pt supported catalysts

In this first case study, the rates of carbon deposition for (1)Pt/SiO_2, (2)Pt/Cr_2O_3, (3)Pt/TiO_2 and (4)Pt/ZrO_2 calculated from the measured carbon deposition by TPH reported by Bradford and Vennice[64, 65] are compared to the predicted trend of coke formation rate all shown in Table 5. Note that the rate of carbon deposition is calculated by the total carbon deposition divided by the total measurement time via the temperature programmed hydrogenation (TPH).
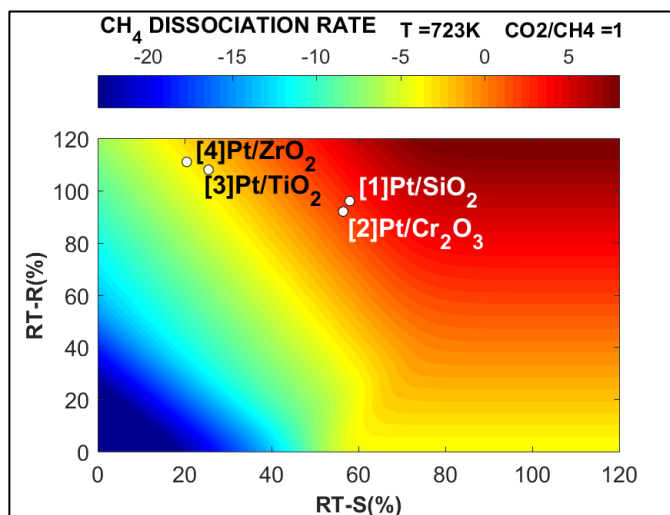
Figure 5 Rate of methane dissociation of Pt supported catalysts ((1)Pt/SiO_2, (2)Pt/TiO_2, (3)Pt/Cr_2O_3 and (4)Pt/ZrO_2) at operating condition of T = 723 K, CO_2/CH_4 = 1 same as the setup of experimental data and the reference catalyst is Ni(111)
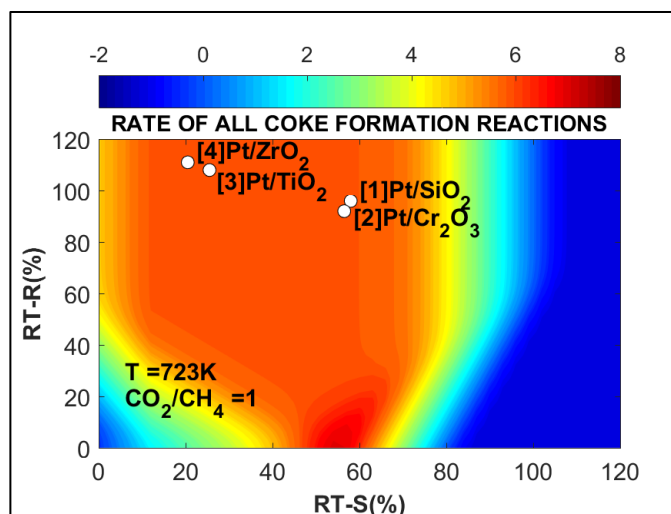
Figure 6 Rate of combined coke formation reaction of CH*, CO* and Boudouard reaction of Pt supported catalysts ((1)Pt/SiO2, (2)Pt/TiO2, (3)Pt/Cr2O3 and (4)Pt/ZrO2) at operating condition of T = 723 K, CO_2/CH_4 = 1 same as the setup of experimental data and the reference catalyst is Ni(111)
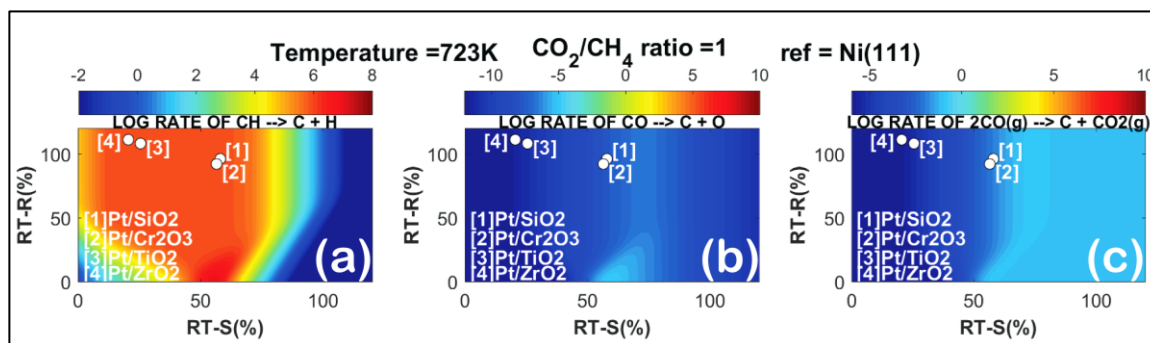
Figure 7 Rate of coke formation reaction from (a) CH*, (b) CO* and (c) Boudouard reaction of Pt supported catalysts ((1)Pt/SiO2, (2)Pt/Cr2O3, (3)Pt/TiO2 and (4)Pt/ZrO2) at operating condition of T = 723 K, CO_2/CH_4 = 1 same as the setup of experimental data and the reference catalyst is Ni(111)

Table 5 Comparison of the experimental data and predicted rate of coke formation via approach 1 and the reference catalyst is Ni(111) for Pt supported catalysts

Parameters	Catalysts			
	(1)Pt/SiO$_2$	(2)Pt/Cr$_2$O$_3$	(3)Pt/TiO$_2$	(4)Pt/ZrO$_2$
Experimental data				
$E_{a,app,CH4}$ (kcal/mol)	15	16	23	24
Total carbon deposition	41	28	15	9
Time on TPH (h)	3	3	5	73
Coke deposition (h^{-1})	13.7	9.3	3.0	0.12
Ratings concept				
Calculated				
RT-R (%RT)	96	92	108	111
$\log(r_{CH4})$	2.7	2.0	-2.8	-3.5
Predicted				
RT-S (%RT)	58	57	26	21
$\log(r_{Cgen,total})$	5.9	5.9	5.9	5.9
$\log(r_{Cgen,CH})$	5.9	5.9	5.9	5.9
$\log(r_{Cgen,CO})$	-7.6	-7.7	-11.0	-11.5
$\log(r_{Cgen,BD})$	-2.0	-2.1	-5.3	-5.8

From the experimental data, the trend for rate of coke deposition is (1)Pt/SiO$_2$, > (2)Pt/Cr$_2$O$_3$, > (3)Pt/TiO$_2$ > (4)Pt/ZrO$_2$ which is in good agreement with our predicted coke formation rate. These trends indicate that the least coke-resistant catalysts are (1)Pt/SiO$_2$ and (2)Pt/Cr$_2$O$_3$ as they generate the highest amount of coke verified by TPH for the same period of time, when compared to the two most coke-resistant catalysts that are (3)Pt/TiO$_2$ and (4)Pt/ZrO$_2$. This can be explained by the predicted rate of coke formation from our ratings concept. All of the Pt catalysts exhibit the same magnitude of coke formation via CH*, in which this does not clarify the trend from the experimental data. The

key factors that make (1)Pt/SiO$_2$ and (2)Pt/Cr$_2$O$_3$ the most coke deposited catalysts is that they have the highest log rate of coke formation via CO* and Boudouard reaction predicted from the ratings concept shown in Table 5. Trends for the rate of coke formation from both coke formation steps are in good agreement with the measured amount of coke deposition from the experimental data as (1)Pt/SiO$_2$ > (2)Pt/Cr$_2$O$_3$ > (3)Pt/TiO$_2$ > (4)Pt/ZrO$_2$.

4.2.2. Case study 2: Rh supported catalysts

In this case study, the Rh supported catalysts are studied. The same procedure as in the Pt case was followed starting by utilizing the apparent activation energy of the methane dissociation step from experiments [66]. After this step, the reactivity rating (RT-R) and the log rate of CH$_4$ consumption were calculated. From these two parameters, the stability rating (RT-S) was obtained by reading the reactivity surface (RS) at Rh catalysts operating condition shown in Figure 8. Now that the (RT-S, RT-R) index for each catalyst is known, we determine all of the coke formation and removal rates by reading the stability surfaces (SS) for each coke formation reactions in Figure 9(a), (b) and (c) and coke removal reactions in Figure 9(d), (e) and (f), accordingly, where all the predicted rates of coke formation and removal were summarized in Table 6.
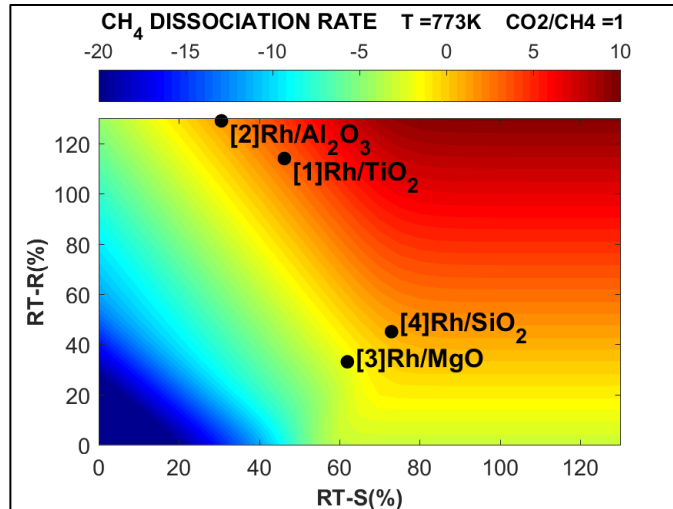
Figure 8 Rate of combined coke formation reaction of CH*, CO* and Boudouard reaction of Rh supported catalysts ((1)Rh/TiO$_2$, (2)Rh/Al$_2$O$_3$, (3)Rh/MgO and (4)Rh/SiO$_2$) at operating condition of T = 773 K, CO$_2$/CH$_4$ = 1 same as the setup of experimental data[66] and the reference catalyst is Ni(111)
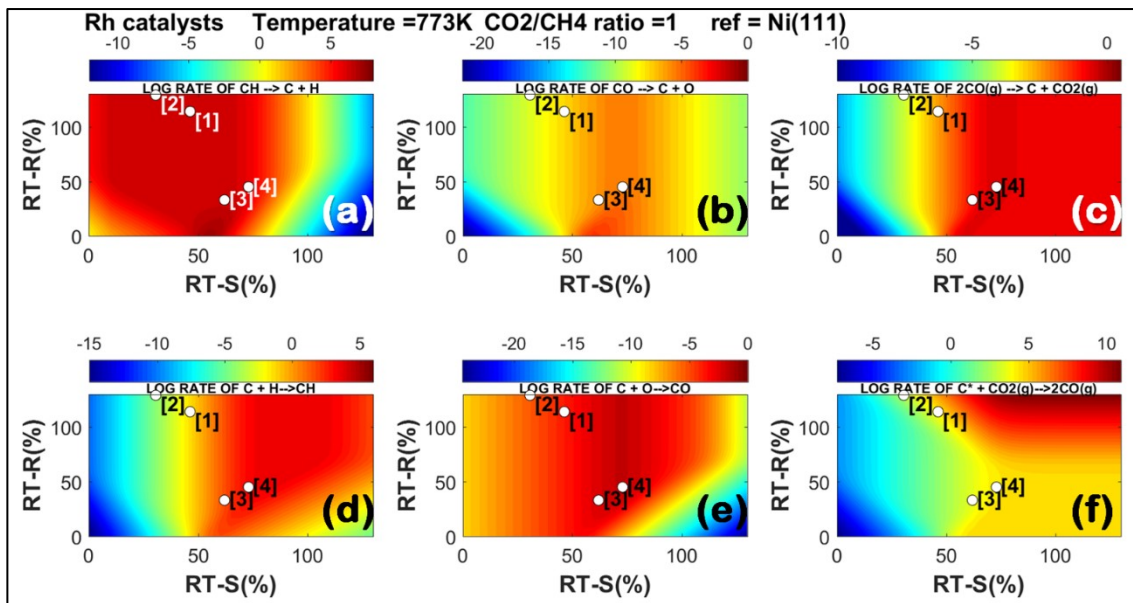
Figure 9 Rate of coke formation reaction from (a) CH*, (b) CO* and (c) Boudouard reaction and coke removal via (d) H*, (e) O* and (f) reverse-Boudouard reaction of Rh supported catalysts ((1)Rh/TiO$_2$, (2)Rh/Al$_2$O$_3$, (3)Rh/MgO and (4)Rh/SiO$_2$) at operating condition of T = 773 K, CO$_2$/CH$_4$ = 1 same as the setup of experimental data[66] and the reference catalyst is Ni(111)

42

Table 6 Comparison of the experimental data and predicted rate of coke formation via approach 1 and the reference catalyst is Ni(111) for Rh supported catalysts

Parameters	Catalysts			
	(1)Rh/TiO$_2$	(2)Rh/Al$_2$O$_3$	(3)Rh/MgO	(4)Rh/SiO$_2$
Experimental data				
$E_{a,app,CH4}$ (kcal/mol)	15.8	18.2	23.2	19.1
Total carbon deposition	0.003	0.06	0.04	0.04
Time on TPH (h)	1	1	1	1
Coke deposition (h^{-1})	0.003	0.06	0.04	0.04
Ratings concept				
Calculated				
RT-R (%RT)	114	129	33	45
log(r_{CH4})	2.92	1.36	-1.90	0.77
Predicted				
RT-S (%RT)	46	31	62	73
log($r_{Cgen,total}$)	6.5	9.4	3.4	1.2
log($r_{Cgen,CH}$)	6.5	9.4	3.4	1.2
log($r_{Cgen,CO}$)	-7.3	-5.9	-8.9	-10.0
log($r_{Cgen,BD}$)	-1.3	-1.4	-1.3	-1.3
log($r_{Crem,total}$)	9.6	11.0	1.6	2.8
log($r_{Crem,H}$)	-4.6	-4.6	-4.6	-4.6
log($r_{Crem,O}$)	-9.1	-7.7	-10.7	-11.7
log($r_{Cgen,RBD}$)	9.6	11.0	1.6	2.8
Net coke removal	9.6	11.0	-3.3	2.8

Based on the data in Table 6, the trend in coke formation, coke removal and net coke formation rate were plotted in Figure 10 and compared to the trend in coke deposition obtained via temperature-programmed oxidation (TPO) by Erdohelyi et al. which measures the coke formed during the first hour of the DRR tested on Rh supported catalysts:

(1)Rh/TiO₂, (2)Rh/Al₂O₃, (3)Rh/MgO and (4)Rh/SiO₂ [66]. It was found from the experiment that the amount of coke deposited was in the order of (2)Rh/Al₂O₃ > (3)Rh/MgO ≈ (4)Rh/SiO₂ > (1)Rh/TiO₂.
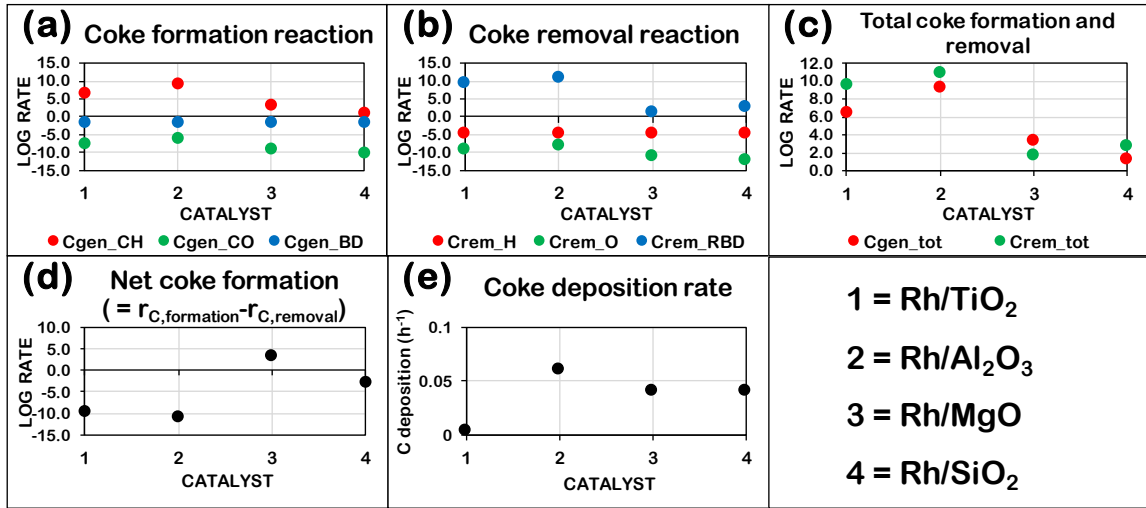
Figure 10 Predicted log rate of (a) coke formation reactions from CH* (Cgen_CH), CO* (Cgen_CO) and Boudouard reaction (Cgen_BD), (b) coke removal reactions from H* (Crem_H), O* (Crem_O) and reverse-Boudouard reaction (Cgen_RBD), (c) total coke formation rate and coke removal rate, (d) the net coke formation which represents how large the total coke formation is compared to the coke removal which equals the total rate of coke formation deducted by the total rate of coke removal, where the positive value means coke formation is higher than removal, while the negative value means that the system has higher coke removal than formation and (e) coke deposition measured from experiment[66] on Rh supported catalysts (number on x axis is designated as (1)Rh/TiO₂, (2)Rh/Al₂O₃, (3)Rh/MgO and (4)Rh/SiO₂) at operating condition of T = 773 K, CO₂/CH₄ = 1 same as the setup of experimental data[66] and the reference catalyst is Ni(111)

Next, we analyze the results of predicted rate of coke formation and removal in Figure 10(a), (b), (c) and (d) in order to compare them to the measured coke deposition which is plotted in Figure 10(e). The following observations were found. For the individual coke producer in Figure 10(a), coke formation from CH* is the main source followed by the

Boudouard reaction and coke generated from CO*, respectively. For the removal process of coke illustrated in Figure 10(b), the reverse-Boudouard reaction is the main process to remove coke as it accounted for the highest coke removal rate among coke removal via hydrogenation from H* and oxidation from O*. In order to describe coking on the catalysts, we first considered the total rate of coke formation and removal for each catalyst which is plotted in Figure 10(c) as red and green markers, accordingly. Thereafter, we analyze these data and obtain the net rate of coke formation plotted in Figure 10(d), which is the total rate of coke formation minus the total rate of coke removal for each catalyst.

We found that for (1)Rh/TiO$_2$ which exhibits the lowest coke deposition via experiment, its net coke formation rate is highly negative suggesting a very high coke removal at reaction condition of T = 773 K and CO$_2$/CH$_4$ ratio of 1, On the other hand, the (3)Rh/MgO and (4)Rh/SiO$_2$ which showed very high coke deposition were predicted to have very low net rate of coke formation within the value of log rate of -5 to 5 meaning that the systems merely have the ability to remove coke on the catalysts resulting in a very high coke deposition found from experiment. Lastly, in the case of (2)Rh/Al$_2$O$_3$, it possessed the highest coke formation determined via experiment which agreed with the total coke formation rate prediction by the extended ratings concept. Note that, although our model predicted its total coke formation rate to be in good agreement with coke deposition, the model also predicted its total coke removal rate to be highest among other catalysts, which resulted in the negative net rate of coke formation. This suggested the catalyst to be coke-resistant in contrast to the experimental finding. Explanations to this behavior are that, (1) the coke deposition measured by TPO by Erdöhelyi et al.[66] represents all forms of coke namely, atomic coke or alpha coke (C$_\alpha$), where the evolution of C$_\alpha$ will result in the

formation of larger coke such as amorphous carbon (C_β) and graphitic carbon (C_C) [20], but our model described the rate in which the atomic coke (C_α) can form via coke formation rate and the rate where it can be removed by coke removal rate, (2) another possible cause for the result is that the amount coke deposition was measured only in the first hour of reaction, where the amount contained may be too small to construct any coking trend. Also, this is different from the Pt case that at least 3 hours of reaction is carried out before the first measurement was made[64, 65].

4.3. Conclusions

In summary, the present study illustrates the practical use of the extended ratings concept to predict the stability of the DRR catalysts. The concept is successfully demonstrated in the case of Pt supported catalysts when the reactivity of the catalyst is characterized by the apparent activation energy. This energy is the only input used to calculate the reactivity rating (RT-R) and the rate of CH4 decomposition which are used to determine the location of the catalyst of the reactivity and stability surfaces (RS and SS). However, in the case of Rh supported catalysts, the coke deposition is not well predicted suggesting that the one-parameter procedure needs improvement. First of all, it is recommended that the measurement of activation energy from experiment could be made more accurate if the reaction is setup at high space velocity to avoid the effects of mass transfer, pore diffusion since if too low, the assumption of surface reaction as the rate limiting step would not be true. Secondly, another approach for the prediction of the rate of coke formation is to use the reactivity ratings (RT-R) and stability ratings (RT-S) to locate the location of the catalysts on RS and SS, where the calculation of RT-R and RT-S would

now need additional values of apparent activation energy from experiment. It is also important to remark that the prediction from the ratings concept is the description of rates at steady state (as pseudo steady state hypothesis is assumed), thus, the time needed for the validation of the predicted data is the time after the steady state is reached, where the experimentalist should carry out the experiment and determine first the steady state time. Further optimization of the calculation procedure may be also required, so the number of required experiments could be minimized. According to this, the predicted coke formation trend should be at its highest reliability. In such a way, it would be possible to perform a fast screening of reactive yet stable DRR catalysts with more reliability via our ratings concept prior to thorough experimental tests on stability like TPH[64] or TPO[14] thus saving time and efforts.

5. EFFECTS OF REACTION CONDITIONS ON THE PERFORMANCE OF DRR CATALYSTS[*]

5.1. Overview

Another important factor that affects the reactivity and stability of DRR catalysts is the reaction condition. In this section, we evaluate the rates of DRR, coke formation and coke removal via the analysis of reactivity surface and stability surface indexes at various DRR operating conditions in order to examine the effects of operating temperature (T) and reactants feed ratio (CO_2/CH_4 ratio) prior to the determination of the optimal operating conditions for the DRR catalysts. The studied temperatures are 500 K, 600 K, 700 K, 800 K, 900 K and 1000 K, while CO_2/CH_4 feed ratios are investigated at 0.2, 0.5, 1.0, 2.0 and 5.0 when the total pressure is constant at 2.2 bar with the pressure of $CO_{(g)}$ and $H_{2(g)}$ each fixed at 0.1 bar and the combined pressure of $CH_{4(g)}$ and $CO_{2(g)}$ is 2.0 bar.

Table 7 Ratings and classification Ni-based catalysts

Catalysts	RT-S_{avg} (%RT)	RT-R_{avg} (%RT)	Type
Ni(111)	100	100	1
Ni(100)†	59	114	3
Ni(211)†	68	107	3
Ni3C(001)	82	104	3
NiO(111)-*p*(2x2)	86	76	1
†the activation energies for Ni(100) and Ni(211) are from Fan et al.[5]			
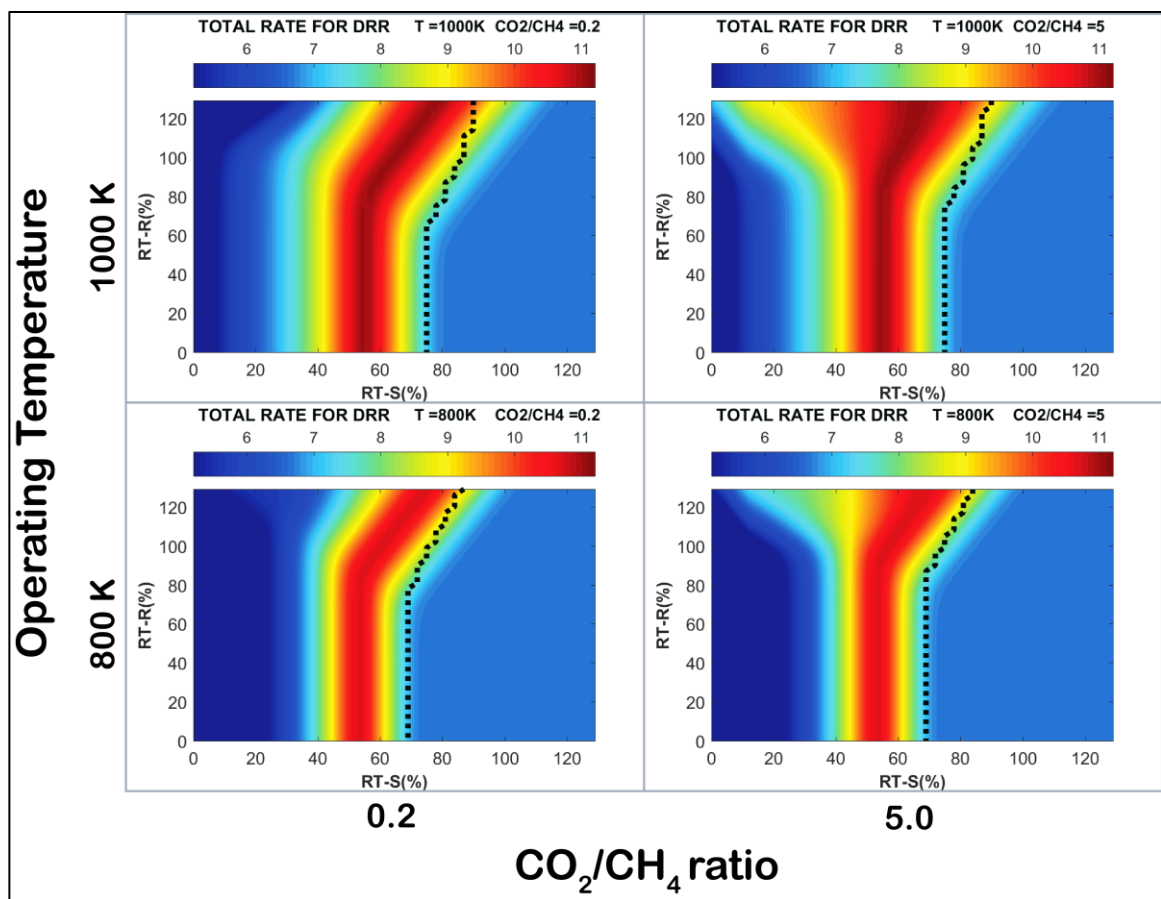
Figure 11 Reactivity surface (RS) representing the DRR rate for all location at various operating temperatures and CO_2/CH_4 feed ratios, where the dotted black line separating each of the 4 figures is the coking boundary, the left side of boundary is the coke formation zone, while the right side is the coke removal zone which has higher coke removal rate than coke formation, and the complete variations of temperature and feed ratio figures can be found in Appendix A
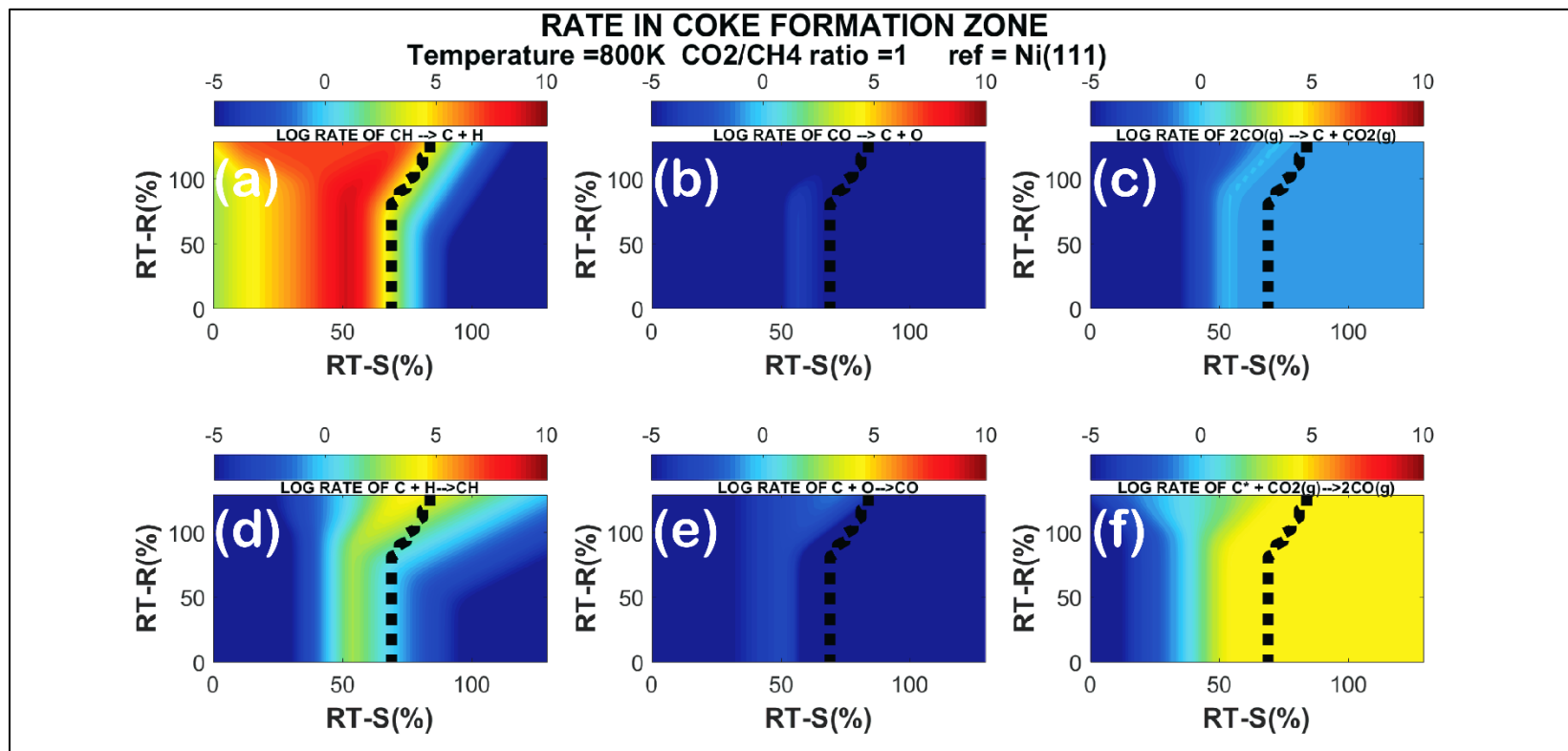
Figure 12 The stability surface (SS) showing individual coke formation reaction as (a) C from CH* dissociation, (b) C from CO* dissociation, (c) C from Boudouard reaction and individual coke removal reaction as (d) removal by H*, (e) removal by O* and (f) removal by reverse-Boudouard reaction all at temperature = 800 K and CO_2/CH_4 = 1, where the colors from blue to red indicate the magnitude of log rate of each specified reaction, the dotted black line separating each of the six figures is the coking boundary with the coke formation zone at the left, and the coke removal zone at the right of this boundary, and the complete variations of temperature and feed ratio figures can be found in Appendix A
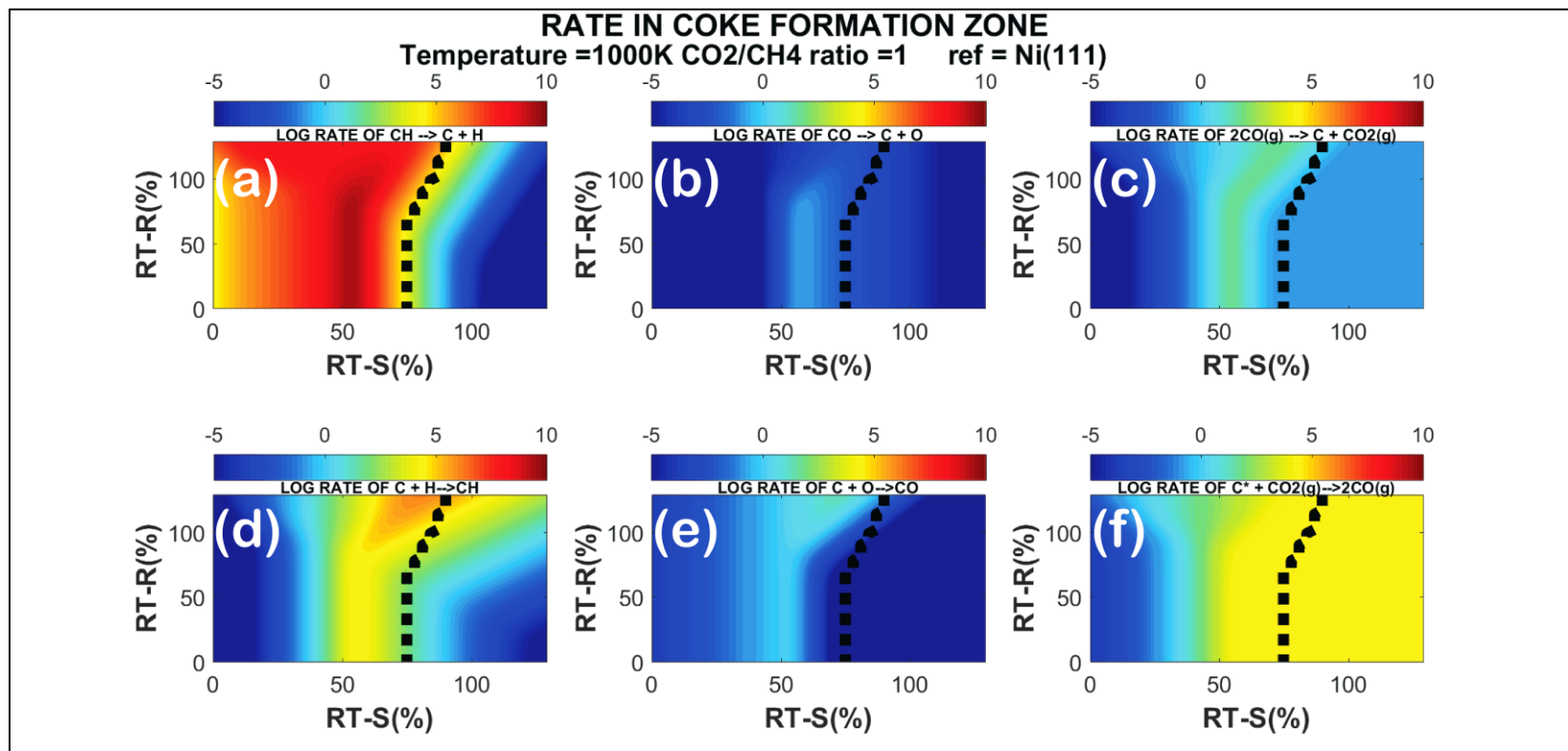
Figure 13 The stability surface (SS) showing individual coke formation reaction as (a) C from CH* dissociation, (b) C from CO* dissociation, (c) C from Boudouard reaction and individual coke removal reaction as (d) removal by H*, (e) removal by O* and (f) removal by reverse-Boudouard reaction all at temperature = 1000 K and $CO_2/CH_4 = 1$, where the colors from blue to red indicate the magnitude of log rate of each specified reaction, the dotted black line separating each of the six figures is the coking boundary with the coke formation zone at the left, and the coke removal zone at the right of this boundary, and the complete variations of temperature and feed ratio figures can be found in Appendix A

Figure 14 The stability surface (SS) showing individual coke formation reaction as (a) C from CH* dissociation, (b) C from CO* dissociation, (c) C from Boudouard reaction and individual coke removal reaction as (d) removal by H*, (e) removal by O* and (f) removal by reverse-Boudouard reaction all at temperature = 1000 K and $CO_2/CH_4 = 5$, where the colors from blue to red indicate the magnitude of log rate of each specified reaction, the dotted black line separating each of the six figures is the coking boundary with the coke formation zone at the left, and the coke removal zone at the right of this boundary, and the complete variations of temperature and feed ratio figures can be found in Appendix A

5.2. Effects of operating temperature on catalyst's performance

For better visualization, Figure 11 is divided into two zones. The dividing line is the coking boundary separating the coke formation and coke removal zones, Accordingly. The left side of the boundary is the "coke formation zone", whereas the right side of the boundary illustrates the "coke removal" zone. If any catalyst is located at a high rate coordinate but it is on the left side of the boundary, such catalyst would be reactive but not stable since it has a higher rate of coke formation than removal. The results shown in Figure 11 illustrate that as expected, at every constant feed ratio, a temperature increase enhances the rate of reaction and raises both coke formation and coke removal rates illustrated in Figure A 1, Figure A 2 and Figure A 3 in Appendix A. Further interpretation of RS and SS leads to the following observations.

1. The total rate of DRR increases for all locations whether the catalysts are in coke formation or coke removal zone shown in Figure 11.

2. When considering the operation at 800 K and 1000 K shown in Figure 12 and Figure 13, accordingly, the rates of each coke formation and coke removal reaction in both coke formation zone and coke removal zones rise as T escalates, while the location of the coke formation-removal boundary also changes with increased temperature such that the coke formation zone (left side of the boundary) expands.

These observations suggest that the increase in temperature would not only intensifies the coke formation and removal rates in both zones and also changing the character of any catalyst especially, the one near the boundary which can shift into another zone when the coking boundary moves due to temperature change. Thus, the catalyst near the coke formation-removal boundary may have a chance to shift from the coke removal

zone to the coke formation zone and vice versa. Note that the shifting across the coking zone as a result of changing boundary is also observed when CO_2/CH_4 ratio changes as will be discussed in the next section.

It may be concluded that high temperature could be either harmful or beneficial to the stability of the catalysts depending on their nature represented by the reactivity and stability rating indexes. At high temperature, catalysts with high stability rating (RT-S > coke formation-removal boundary) could gain coke-resistant properties due to higher coke removal rate. In contrast, the ones with low stability rating (RT-R < coke formation-removal boundary) would suffer from high coke formation rate as temperature increases. As a result, operation at high temperature would clearly promote reactivity, but to achieve high stability, only the catalysts that are located in the coke removal zone would benefit from the increase in temperature. In other words, the catalysts with high stability rating (RT-S) values will exhibit difficult coke formation and easy coke removal.

5.3. Effects of reactants feed ratio on reactivity and stability

Another parameter that affects the reactivity and stability of the system is the reactants feed ratio (CO_2/CH_4). We investigate the scheme of high CO_2/CH_4 compared to low CO_2/CH_4 feed ratio at a constant pressure of 2.2 bar. By interpreting the reactivity map in Figure 11 and the stability surface in Figure 13 (at a low CO_2/CH_4 feed ratio of 1 and T = 1000 K) compared to Figure 14 (at a high CO_2/CH_4 feed ratio of 5 and T = 1000 K), trends in reactivity and stability could be established. Note that complete study on reactant feed ratio from 0.2 to 5 is shown in Appendix A in Figure A 5 to Figure A 9.

For the effects on reactivity, Figure 11 shows that the changes in the intensity of reaction rate in both zones depend on the reactivity ratings (RT-R), too. In the upper part of the coke formation zone (high RT-R), as CO_2/CH_4 increases from 0.2 to 5.0, the reaction rate is promoted more than in the lower part (low RT-R) of this zone. This can be explained via Figure 13 and Figure 14 as follows.

1. The reverse-Boudouard reaction (Figure 13(f) and Figure 14(f)) which removes carbon via $CO_{2(g)}$ producing $CO_{(g)}$ is promoted, hence inducing increases of the DRR rate as more $CO_{(g)}$ is generated.

2. This reverse-Boudouard reaction dominates and becomes the main coke removal process suppressing other coke removal processes via H* (Figure 13(d) and Figure 14(d)) and O*(Figure 13(e) and Figure 14(e)).

3. the decrease in coke removal by H* enhances its reverse reaction, the CH* dissociation reaction (Figure 13(a) and Figure 14(a)) that forms C* and H*.

4. the increase in H* content from higher CH* dissociation induces more $H_{2(g)}$ formation raising the DRR rate (Figure 11).

For these reasons, the total DRR rate is enhanced at high CO_2/CH_4 as a result of higher reverse-Boudouard and CH* dissociation reactions which increase $CO_{(g)}$ and $H_{2(g)}$ formation, respectively. In addition, in both zones, if the catalysts have high reactivity rating (RT-R), a higher rate of reaction would be achieved for the same increase in the CO_2/CH_4 ratio. This is because high RT-R would promote more the reverse-Boudouard and CH* dissociation reactions since CO_2 and CH_4 could now be activated with less difficulty at this high RT-R rating.

On stability, as shown in Figure 11 at T = 1000 K, the coke formation-removal boundary shifts to the left at high CO_2/CH_4 ratio resulting in the expansion of the coke removal zone and the shrinkage of the coke formation zone. This indicates that there are more areas where the coke removal overcomes coke formation at a high CO_2/CH_4 ratio. Moreover, the intensity of the net coke formation and removal rate of both zones increases with the CO_2/CH_4 ratio. The reasons behind this situation could be explained via Figure 13 and Figure 14 as follows.

In the coke formation zone (left side of the coking boundary in (a) to (f) of both Figure 13 and Figure 14), these observations were found.

1. more adsorbed CO* is produced as more CO_2 is introduced into the system leading to the promotion of the Boudouard reaction (Figure 13(c) and Figure 14(c)) and CO* dissociation (Figure 13(b) and Figure 14(b)), where both reactions form C as a product increasing the coke formation rate.

2. The intensification of the reverse-Boudouard reaction (Figure 13(f) and Figure 14(f)) due to higher CO_2/CH_4 ratio suppresses other coke removal processes from H* (Figure 13(d) and Figure 14(d)) and O* (Figure 13(e) and Figure 14(e)), thus lowering their rate.

3. The decrease in coke removal rate via H* and O* promotes their reverse reactions, which are CH* dissociation (Figure 13(a) and Figure 14(a)) and CO* dissociation (Figure 13(b) and Figure 14(b)) contributing to higher coke formation rate with CH* as the main coke producer.

From the above-mentioned causes of high coke formation rate in the coke formation zone at high CO_2/CH_4, it can be suggested that if the catalysts are in this zone, the CO_2 content should be kept low in order to restrict coke from CH* that is the main coke formation source.

Next, in the coke removal zone (right side of the coking boundary in (a) to (f) of both Figure 13 and Figure 14), the following observations were revealed.

1. higher CO_2 content boosts the reverse-Boudouard reaction (Figure 13(f) and Figure 14(f)) which again dominates over other coke removal processes

2. coke removal steps via H* (Figure 13(d) and Figure 14(d)) and O* (Figure 13(e) and Figure 14(e)) decline as a result of the previous step

3. In this zone, this magnitude of the reverse-Boudouard reaction is so high that the coke formation via the Boudouard reaction (Figure 13(c) and Figure 14(c)) diminishes resulting in low combined coke formation rate

To sum up, for the coke removal zone, the increase in a reverse-Boudouard reaction is the main factor that enhances the stability. Therefore, the operation at high CO_2/CH_4 ratio would be advantageous for enhanced reactivity. For the coke-resistance, high CO_2 content would be beneficial or not depending on the location of the catalysts in the stability surfaces (SS). For instance, Ni(111), Ni(100) and Ni(211) are located in the coke removal zone, as shown by the RT-S and RT-R indexes in Table 7. As all these Ni facets may be parts of a Ni catalyst in the DRR, it can be concluded that the increase in CO_2/CH_4 ratio would lead to higher coke removal; thus, higher coke-resistant for the DRR Ni catalyst. Furthermore, this is also supported by experimental reports stating that the Ni catalyst operated at a high CO_2/CH_4 ratio around 3 would lead to no carbon formation[67].

5.4. Strategies towards optimal DRR operating conditions

Prior to proposing strategies for reactive and coke-resistant DRR catalysts, the catalysts must be classified based on the reactivity and stability ratings since different strategies may be needed. As a result, four types of catalysts are categorized based on their RT-S and RT-R as shown in Figure 15.
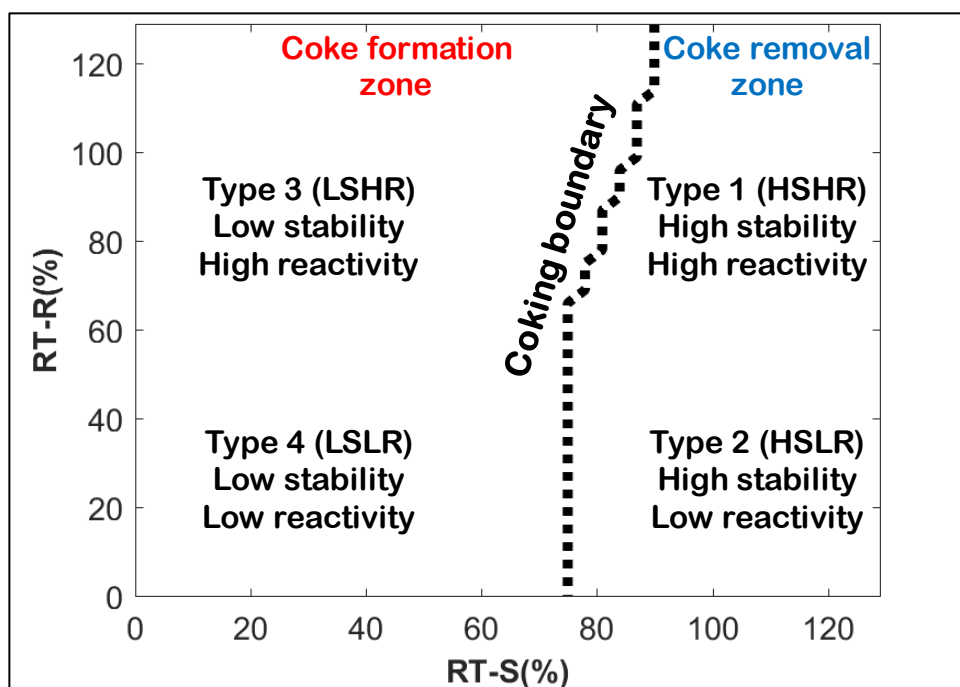
Figure 15 Coke formation and coke removal zone together with the 4 classifications of DRR catalysts at 1000 K, CO_2/CH_4 feed ratio = 1 and reference catalyst of Ni(111)

In order to customize the strategies for each of them, we have to recall the knowledge from the effects of operating conditions, where (1) temperature would only affect the intensity of the rate, e.g., high T would increase the rate of reaction, coke formation and coke removal without changing the coke formation-removal boundary and (2) by changing the

CO_2/CH_4 feed ratio the coking boundary could be shifted, e.g., the expansion of the coke removal zone at high CO_2/CH_4 ratio.

According to this analysis, the following strategies are proposed.

1. Type 1 (HSHR): as these combinations of high selectivity and high reactivity are in the coke removal zone, high temperature combined with high CO_2/CH_4 ratio would enhance both reactivity and stability of the catalysts since the DRR rate and the total coke removal rate are promoted.

2. Type 2 (HSLR): the only thing that is different from Type 1 is that increases in the temperature and CO_2/CH_4 ratio would increase the rate of reaction and coke removal although to values lower than Type 1. However, the same strategy described for Type 1 could be applied for Type 2.

3. Type 3 (LSHR): since the catalyst materials fall now in the coke formation zone there are two options. First, if increasing the CO_2/CH_4 ratio shrinks the coke formation zone up to the point where the catalyst may be located into the coke removal zone, the Type 1 strategy may be used after high CO_2/CH_4 ratio operation. This shifting would be possible if the catalysts are near the coke formation-removal boundary. On the other hand, if the catalyst is still in the coke formation zone after the operation at high CO_2/CH_4 ratio, both the temperature and CO_2/CH_4 ratio have to be lowered down in order to suppress coke formation while keeping in mind that the adjustment of both operating T and feed ratio down should still yield high enough DRR rate so that the catalysts would not become inactive.

4. Type 4 (LSLR): this catalyst possesses lower stability and reactivity ratings (RT-S and RT-R). As a consequence, the only possible strategy that could be applied is to

operate at both low temperature and low CO_2/CH_4 which will result in the suppression of coke formation reaction but it will cause a decrease in the DRR rate. As a result, the best choice for Type 4 catalyst is to make it coke-resistance with low DRR rate where although it becomes less reactive, its life could be extended.

5.5. Conclusions

In conclusion, in order to improve the reactivity and coke-resistant property of DRR catalysts without any modifications other than the adjustment of the operating conditions, four strategies could be applied based on four types of the catalyst. For Type 1 and 2, the optimal operating conditions could lead to reactive and stable DRR catalysts, while for Type 3, if the catalyst is located near the coke formation-removal boundary, it could be shifted to Type 1 yielding reactive and stable catalysts. Otherwise, the optimal operating condition would bring them to a stable but low reactivity point instead. For the Type 4 catalysts when an optimal condition is applied they would become stable but less reactive, where no more modification could be made to shift them into the coke removal zone.

6. SURFACE TRANSFORMATION OF NICKEL-BASED DRR CATALYSTS

6.1. Overview

In addition to the evaluation of catalysts performance, the understanding of how these catalysts behave during the DRR is another vital information.
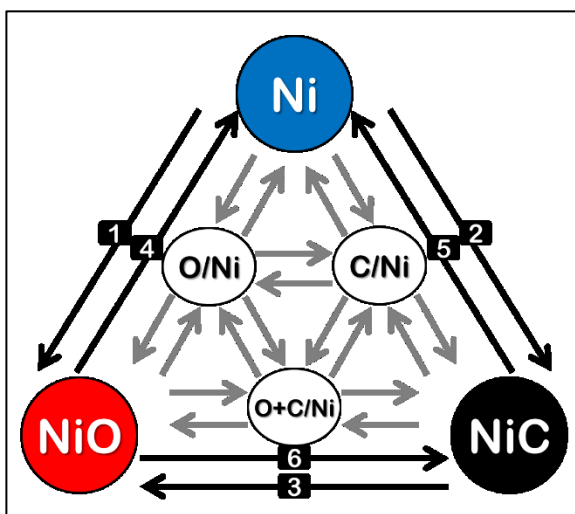
Figure 16 Surface transformation network for Ni DRR catalysts

Many have reported that for the Ni-based catalyst, the main phases involved in the DRR are the metallic, oxide and carbide [6, 22, 60, 63, 68]. Each of these phases can transform between each other during the dry reforming reaction of methane as depicted in Figure 16. From the illustration, the proposed structure for the catalyst at the beginning of the reaction is the clean metallic surface labeled as "Ni". When the reaction begins, it has two choices of surface transformation: oxidation or a carburization designated as routes 1 and 2, respectively. If oxidation proceeds, the partial oxidized Ni labeled as "O/Ni" is formed which finally arrives at the complete oxide named "NiO." In general, this process could be

61

described via the Cabrera-Mott mechanism proposed for the metal oxide formation scheme[69, 70]. On the other hand, if "Ni" undergoes carburization, it would first form partially carburized Ni labeled as "C/Ni" before proceeding to the complete formation of the carbide labeled as "NiC". In addition, such carbide and oxide phases were reported to be able to transform back to metallic Ni via the deoxygenation and decarburization processes labeled as route 4 and 5, respectively[21, 63]. Moreover, the transformations between the oxide and carbide directly without passing through the metallic phase, labeled as routes 3 and 6, are also reported[71]. Therefore, we proposed these 6 transformations routes to be the key pathways governing the reactivity and stability of a catalyst during the DRR as the changes in surface characteristics would directly affect the catalyst performance. For this reason, this work intended to understand the changes in catalyst's performance during the DRR as a result of surface evolution since if we know how to control such surface transformation, the catalyst performance could be designed.

6.2. Characteristics of Ni catalysts during surface transformation

In this section, we investigated the characteristics of each surface type in the surface transformation network of the Ni catalyst during the DRR. First, the coke-resistant property was analyzed in terms of the surface binding strength to coke. To model coke, an adsorbed carbon atom or the alpha coke (C_α) is chosen[20]. For the binding strength, the adsorption energy of the carbon atom ($E_{ads}(C)$) to the surface is used for the description, where a more negative value means stronger coke binding which can be calculated from the following equation.

$$E_{ads}(C) = E_{C/sys} - E_{sys} - E_C \qquad \text{Equation 39}$$

Note that the term $E_{ads}(C)$ is an adsorption energy of C atom on the system's surface (eV), $E_{C/sys}$ is the energy of the carbon adsorbed system's surface (eV), E_{sys} is the energy of the system's surface (eV), and E_C is energy of the carbon atom (eV).
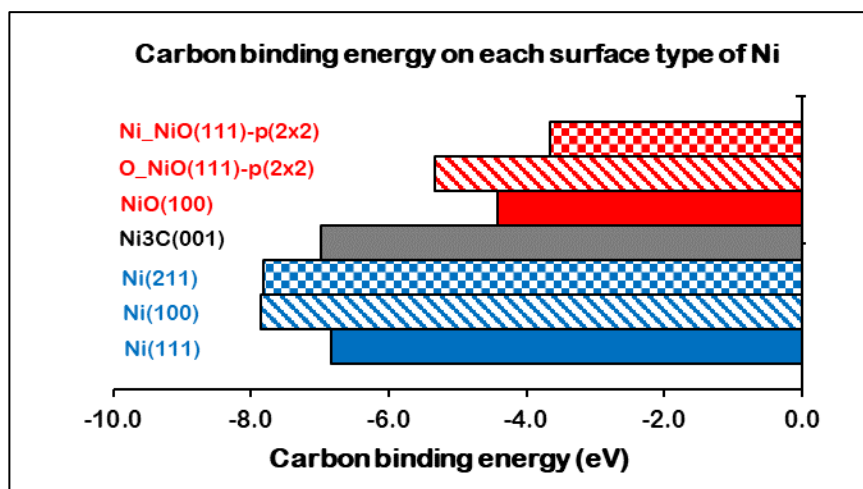
Figure 17 Adsorption energy of carbon atom on each surface, where Ni_NiO(111)-p(2x2) and O_NiO(111)-p(2x2) mean the NiO(111) octopolar reconstructed surface with Ni and O as terminating atoms, respectively

We examined the C binding strength on seven surface types of Ni namely, (1) Nickel-terminated octopolar reconstructed NiO(111), (2) Oxygen-terminated octopolar reconstructed NiO(111), (3) NiO(100), (4) Ni$_3$C(001), (5) Ni(211), (6) Ni(100) and (7) Ni(111). It can be observed from Figure 17 that all the Ni oxide surfaces (surface (1), (2) and (3)) exhibit lower C binding strength than the metallic and carbide surfaces. This may explain why high coke deposition was found on the catalyst surface at the beginning of the reaction since the majority of the fresh Ni catalyst surface is the metallic surface which exhibits strong binding to a carbon atom, an alpha coke formed either by CH_4 or CO_2

dissociations[3-6]. Furthermore, this type of coke is an initial point towards the formation of carbide phase[21, 22], in which if it forms, it would display the comparable binding strength to the metallic. Thus, the accumulated carbon would lead to the higher coke formation illustrated from the following equation, where the term $C*$ is an adsorbed carbon atom on the surface representing α-coke (C_α), the $(C-C)*$ designated the condensed 2-atom carbon species formed via Equation 40, and $*$ referred to the vacant active site.

$$C* + C* \rightleftarrows (C\text{-}C)* + * \hspace{3cm} \text{Equation 40}$$

On the other hand, it was reported from the experiment that the Ni oxide phase could enhance the coke-resistant property of the catalyst[63]. It was shown that the low C binding strength observed on the oxide surface may be the reason behind this improved stability since the active site. This is because it may have less chance to be blocked since the coke is weakly bonded to the oxide surface, and the possibility for higher carbon formation may decrease due to the low concentration of the atomic coke on the surface. However, adding this oxide component to the system may help to reduce the coke accumulation on the active site since this oxide surface is considered one of the active sites. This would add more active sites with low coke binding strength, while the overall coke deposition may not be significantly lowered since coke still accumulates strongly in other regions such as the support which comprises most of the surface in the catalyst[72].

Table 8 The activation energies of elementary reactions involve during the dry reforming reaction of methane for each phase of Ni

Reaction	Metallic*			Oxide**		Carbide
	Ni(111)	Ni(100)	Ni(211)	NiO(111)-p(2x2)	NiO(100)	Ni₃C(001)
$CH_4(g) + 2* = CH_3* + H*$	0.91	0.80	0.62	0.91	1.9	0.71
$CO_2(g) + 2* = CO* + O*$	0.67	0.36	0.74	N/D	N/D	N/D
$H* + H* = H_2(g)$	0.92	0.81	0.77	1.7	N/D	1.0
$CH* + * = C* + H*$	1.3	0.52	0.68	1.5	2.7	1.1
$CO* + * = C* + O*$	2.9	1.8	2.0	N/D	N/D	2.9
$C* + H* = CH* + *$	0.81	0.74	0.92	1.4	1.1	1.0
$C* + O* = CO* + *$	1.6	2.2	1.7	N/D	N/D	2.3
$C* + C* = C\text{-}C* + *$	0.00	4.0	N/D	N/D	1.3	0.10
$C\text{-}C* + * = C* + C*$	1.7	2.4	N/D	N/D	1.6	0.38
1. * for Activation of Ni(100) and Ni(211), please refer to Fan et al. [5]. 2. ** NiO(111)-p(2x2) is Oxygen-terminated NiO(111) octopolar reconstructed surface 3. N/D = not determined						

Another parameter that illustrates the tendency of coke formation is the activation energy (E_a) of the C condensation reaction shown in Equation 40. This reaction captures the event of higher coke formation process proceeding via the bonding of adsorbed carbons or alpha coke ($C_α$). The evolution of $C_α$ will result in the formation of a larger coke such as amorphous carbon ($C_β$) and graphitic carbon (C_C)[20]. The activation energy for the C condensation reaction on the metallic, oxide and carbide surfaces of Ni shown in Table 3 are obtained via the climbing nudged elastic band method (cNEB)[44, 45]. The oxide surface, in this case, NiO(100) exhibits high activation barrier of 1.3 eV for this reaction confirming that the coke-resistant property of the oxide surface, in general, may be due to the difficult formation of a higher coke. The carbide, modeled as Ni₃C(001) exhibited a low activation barrier of 0.10 eV which is significantly lower than that of the oxide surface. This low

coke-resistance of carbide is also demonstrated via experiments stating that higher coke formation is preferred on this surface[60]. For the Ni metallic surface, the Ni(111) was found to have less resistant to coke formation due to its zero activation barrier, whereas the Ni(100) was found to be a very coke-resistant surface with the activation barrier of 4.01 eV which is even higher than that of the oxide surface.

Although the Ni(100) surface may seem to be coke-resistant due to its high E_a for higher coke formation ($C^* + C^* \rightleftarrows C\text{-}C^* + *$), it exhibited high E_a values for other coke formation processes from CH^* and CO^* shown in Table 8, which are 0.52 and 1.8 eV, accordingly. This suggested a different conclusion since these E_a are lower than those both on the Ni(111) metallic (1.3 eV and 2.9 eV) and $Ni_3C(001)$ carbide (1.1 eV and 2.9 eV). Hence, the most coke-resistant system determined by our study is the NiO(100) oxide surface with high activation barrier for atomic coke formation from CH^* and CO^*, while exhibiting high activation barrier for higher coke formation.

We have characterized all surfaces that contribute to the performance of the Ni catalyst during DRR, we would now investigate their behavior to coke during the surface evolution caused by the transformation processes illustrated in Figure 16, including oxidation (route 1), deoxygenation (route 4), carburization (route 2) and decarburization (route 5).
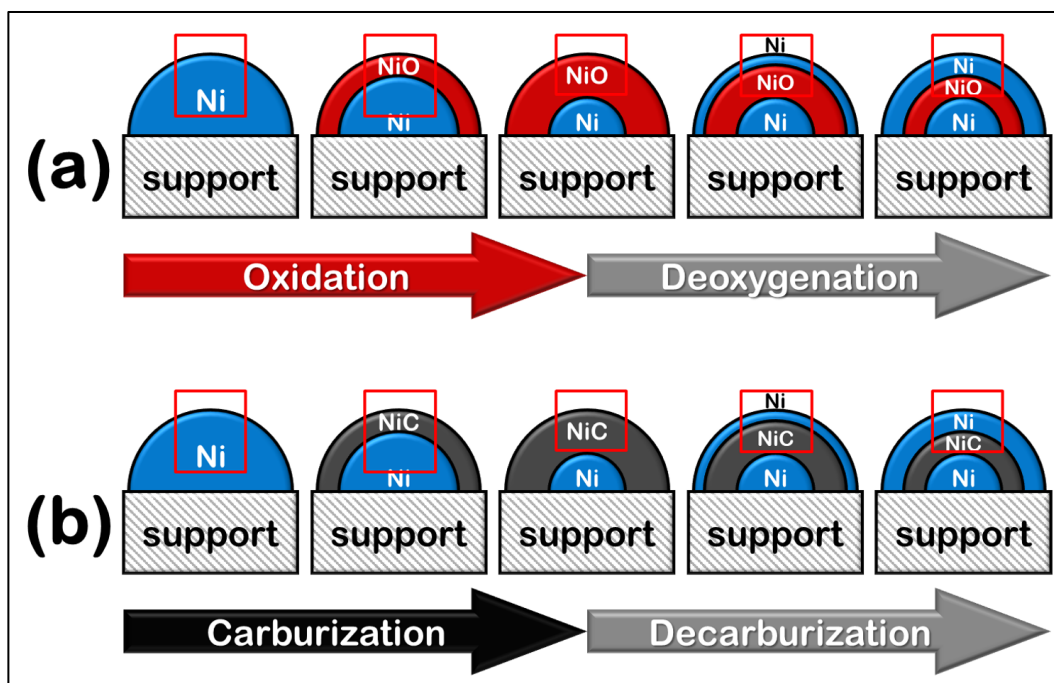
Figure 18 Illustration of the catalyst in (a) the oxidation-deoxygenation and (b) the carburization-decarburization processes during the DRR

To start with, let us construct models that illustrate each route. For any process, the models are classified into three stages: initial, intermediate and final. The initial and final stages are represented by the pure surface of either Ni metallic, oxide or carbide, which are labeled as "Ni", "NiO" and "NiC" in Figure 16 depending on the selected route. On the other hand, the intermediate stages are modeled as the evolving surface between each initial and final stages of each route labeled as "O/Ni" for oxidation and deoxygenation and "C/Ni" for carburization and decarburization routes, respectively. Additionally, the model description for each route is shown in Table 9, while constructions of each model are described in Appendix E.

Table 9 Details of the models for each surface transformation route

Route*	Name	Initial stage	Intermediate stage		Final stage
			Upper layer	Lower layer	
1	oxidation	Ni(100)	NiO	Ni	NiO(100)
2	carburization	Ni(111)	Ni₃C	Ni	Ni₃C(001)
4	deoxygenation	NiO(100)	Ni	NiO	Ni(100)
5	decarburization	Ni₃C(001)	Ni	Ni₃C	Ni(111)
*These routes refer to the route in the surface transformation network in Figure 16					
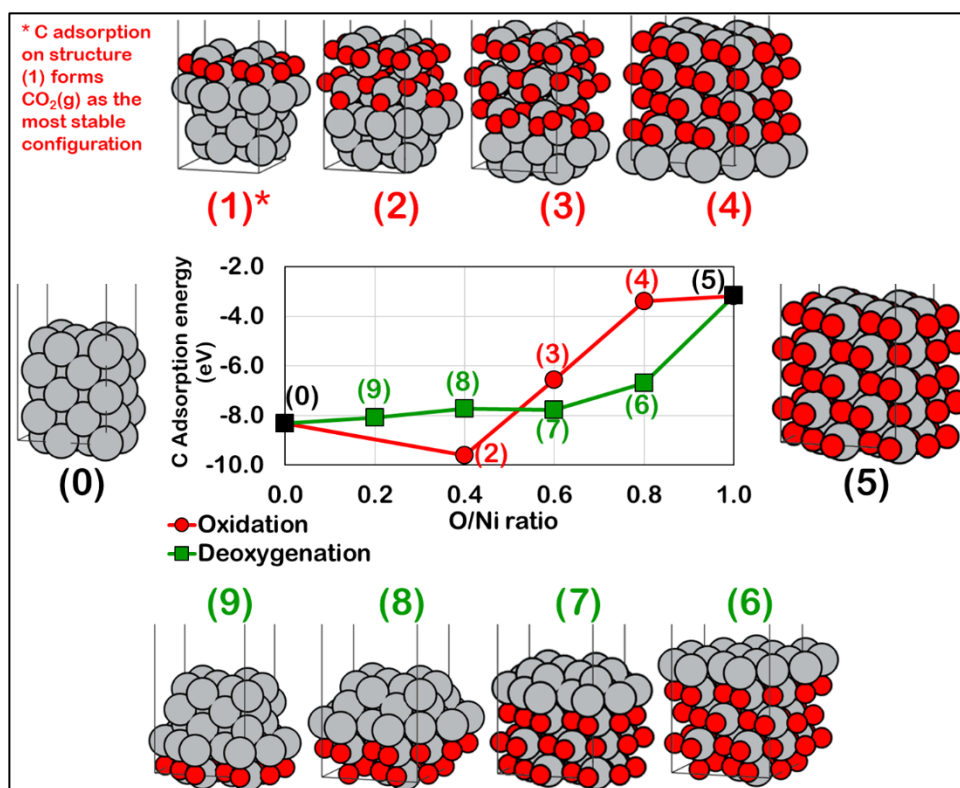
Figure 19 Evolution of the carbon adsorption energy (E_{ads}(C)) during the oxidation and deoxygenation processes, where 0 = Ni(100), 1 to 4 = intermediate stages of the oxidation route, 5 = NiO(100), and 6 to 9 = intermediate stages for the deoxygenation route, where the labels are red = Oxygen atom and grey = Nickel atom

First, the oxidation process (route 1) depicted in Figure 18(a) is assumed to follow the Cabrera-Mott model describing the formation of the metal oxide[69]. The initial surface is composed of pure Ni and as the oxidation proceeds, the surface is oxidized from the top layer down to the lower ones resulting in the final system having oxide over metallic Ni. As a result, for this route, the starting structure is modeled by the Ni(100) slab model, while intermediate models are the partially oxidized Ni(100) constructed as the NiO(100) on top of Ni(100) slab models at various thickness of NiO(100), and the final structure is represented by the NiO(100) slab model. The (100) facet was selected since Ni(100) and NiO(100) are the analogous (100) surface type, where if all O atoms are removed from NiO(100), the resulting structure would be Ni(100). The optimized structures of this process are shown in Figure 19, which are initial (model 0), intermediate (model 1, 2, 3, 4), and final (model 5) stages.

Next, the starting configuration on a deoxygenation process (route 4) was described as the deoxygenation of the oxide layer of Ni, in which the removal of the oxygen atoms initiates at the top oxide layer before proceeding to the lower oxide layer. As seen from Figure 18 (a), the initial structure of this route is the Ni covered by its oxide as the outer layer which is the final stage of the oxidation route. According to this, during the deoxygenation process (route 4), only the oxide portion is considered for the process, where inner core of Ni is not included in the model. As a result, the first structure for this deoxygenation route is represented by NiO(100), where the bottom layer of the slab model is fixed to the lattice parameter of the bulk NiO. The intermediate models consist of pure Ni top layers of different thickness on top of the NiO. Note that during the optimization, only the bottom Ni and O layers are fixed while the rest of atoms are relaxed and the cell shape

and size are allowed to change. The optimized models for this process are illustrated in Figure 19, which are initial (model 5), intermediate (model 6, 7, 8, 9), and final (model 0) stages.
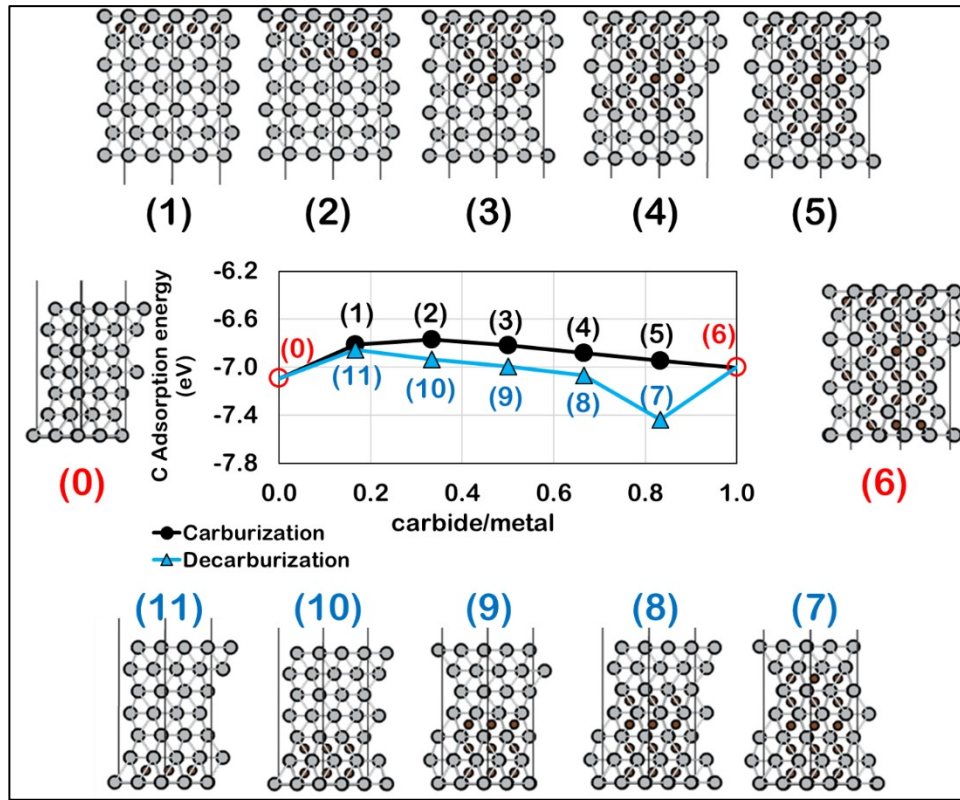
Figure 20 Evolution of the carbon adsorption energy ($E_{ads}(C)$) during the carburization and decarburization processes, where 0 = Ni(111), 1 to 5 = intermediate stages of the carburization route, 6 = $Ni_3C(001)$, and 7 to 10 = intermediate stages for the decarburization route, where labels are brown = Carbon atom and grey = Nickel atom

For the carburization (route 2), it is assumed that the carbide formation initiates from the top layer of metallic Ni and form the complete carbide prior to the formation of the carbide in the deeper layer depicted in Figure 18(b). Like in the case of oxidation, the starting system is the pure Ni metal but this time is modeled on the (111) facet as Ni(111), while the

intermediate models are the partially carburized Ni(111) which have the carbide of Ni$_3$C(001) as the outer layer on the inner layer of Ni(111). The final configuration is the pure carbide of Ni$_3$C(001). For the choice of the facet, Ni(111) and Ni$_3$C(001) were chosen since they are the analogous (111) surface type, where if all C atoms are removed from Ni$_3$C(001) the resulting structure would be Ni(111). The optimized models of each stage are shown in Figure 20, which are initial (model 0), intermediate (model 1, 2, 3, 4, 5) and final (model 6) stages.

On the decarburization route (route 5), the carbon removal on the Ni carbide is initiated at the top carbide layer and propagate down into the lower layers shown in Figure 18(b). The initial structure for this decarburization route (route 5) is the Ni covered by its carbide outer layer which is the same as the final stage of the carburization process (route 2). With respect to this, it is assumed that during the decarburization process (route 5), only the carbide portion is modeled for the process excluding the inner core of Ni as shown in Figure 18(b). As a result, the first structure for this deoxygenation route is represented by Ni$_3$C(001), where the bottom layer of the slab model is fixed to the lattice parameter of the bulk Ni$_3$C, while for the intermediate models, the top and bottom layers are Ni(111) and Ni$_3$C(001), respectively. During the optimization, the bottom Ni and O layers are fixed while the rest of atoms are relaxed and the cell shape and size are also allowed to change. The optimized structures are shown in Figure 20, which are initial (model 6), intermediate (model 7, 8, 9, 10, 11), and final (model 0) stages.

Now that models for each process were constructed and optimized, we will investigate the effects of these processes on coking. We observe how the coke behaves on the catalyst's surface via the strength of carbon binding to the surface which can be

71

calculated by the adsorption energy of carbon in Equation 39, where this value would represent the tendency of coke deposition. To emphasize, if the carbon atom attaches to the surface strongly, it could reach high surface coverage and may increase the tendency of higher coke formation thought C-C condensation reaction or promote the formation of carbide.

For the oxidation and deoxygenation routes shown in Figure 19, first thing to observe is that the binding strength of coke for the NiO(100) oxide, is weaker than that for the Ni(100) metallic, which may suggest the coke-resistant property of the oxide surface since if carbon attaches weakly to the surface, the maximum surface coverage of carbon may be reduced, leading to lower carbon deposition caused by the reaction of adsorbed carbon via C-C condensation reaction. Furthermore, when the oxidation occurs on the metallic surface in configuration 0 and transforms it into configuration 1 prior to the formation of thicker oxide layers until it reaches the pure oxide-like configuration 5, the C binding strength also becomes weaker. This occurs as the oxidation proceeds and slowly converges to the value of the oxide, but not until an O/Ni ratio of 0.6 that this value becomes close to that of the pure oxide. Note that, the value for configuration 1 is not plotted since the most stable configuration for this case forms CO_2 as the product of the atomic C and two nearby oxygen atoms. This behavior suggested that for the partially oxidized Ni to exhibit similar coke-resistant property to that of a pure oxide surface, more than half of the metallic portion has to be oxidized as seen from the value of E_{ads} that gets weaker converging to that of the NiO(100) surface when the O/Ni ratio is 0.6 or higher.

On the contrary, the oxygen removal in the deoxygenation route starting from configuration 5, shows a significant increase in the C binding strength when only the first

layer of oxide was deoxygenated, and the value rapidly reaches the value of Ni(100) only after the removal of the first two NiO(100) layers. This suggests that if we would like to introduce an oxide surface to the system in order to enhance the coke-resistance, such layer should be thick enough to be able to get the advantage of the low coke binding of the oxide. This is because the surface's coke-resistance would become oxide-like at values of O/Ni higher than 0.6. On the other hand, if just one layer of oxide from this thick oxide layer was deoxygenated to metallic, the coke-resistance would change quickly back to the metallic-like. Hence, the oxide surface is very sensitive to the reducer, while needing a high degree of oxidation to recover back the coke-resistant property from a metallic-like to an oxide-like. In summary, the oxidation route would be more difficult to reach completion during the DRR since just only a small reduction would instantaneously initiate the deoxygenation route. Therefore, there would be more chances for the surface to behave as metallic-like more than oxide-like on this (100) facet with respect to coke formation.

Regarding the carburization and decarburization routes, it was shown that the adsorption energy of the Ni in configuration 0 is slightly stronger than the carbide in configuration 6 (Figure 20). Thereafter, it can be observed that for both routes, when the first carburization and decarburization occur on Ni(111) and $Ni_3C(001)$, respectively, the adsorption energy quickly reaches the value of the final stage for each route. On one hand, the first carburization (black data points) over-weakens the binding energy of coke, where the value slowly converges back to the pure carbide along the carburization process. On the other hand, for the first decarburization (blue data points), the adsorption energy rapidly strengthens exceeding the value of the pure metallic and gradually weakens back to the pure metallic when more of the top surface has been decarburized. Thus, we can see that during

carburization (black data points) the surface would weakly bind to coke, while for the decarburization (blue data points), the too low degree in carbon removal (carbide/metal = 0.8) would intensify the strength of coke binding and may lead to unwanted coke deposition. So, for the transformation between the metallic and carbide via carburization and decarburization, the behavior of the surface to become metallic-like and carbide-like would be almost the same as observed on the (111) facet.

In summary, comparing the formation of oxide and carbide surfaces from the metallic surface of a fresh catalyst, for the binding energy of coke to reach that of the pure oxide, a high degree of oxidation is needed when compared to the formation of carbide. In contrast, on the carbide surface, the binding energy would rapidly reach the value of pure Ni_3C after the first carburization. Furthermore, on the deoxygenation and decarburization, after only just the first oxide and carbide layers were removed via forming the metal top surface on NiO and Ni_3C, respectively, the coke binding energy quickly converges to that of the metallic surface. Therefore, during the DRR, if one would like to enhance the coke-resistant property by introducing oxide surfaces to the system, it would need a high degree of oxidation in order to weaken the C binding on the surface and prevent high coke deposition. In other words, a thicker oxide layer is required for the surface to behave like an oxide, while this weak binding to carbon would be easily eliminated upon the first removal of the oxide layer as seen from Figure 19. This is because the E_{ads} of C quickly reaches the value of the pure Ni surface after the first deoxygenation.

6.3. Catalytic performance of surfaces during surface transformation

In this section, the reactivity and the coke-resistant properties for each surface in the surface transformation network were evaluated in terms of the DRR, coke formation and removal rates. These parameters are shown in Table 4 and were obtained via the ratings concept which interpreted the indexes of RT-R and RT-S ratings on each surface as input parameters [73] (detailed setup of the concept is in Chapter 0). In addition, the RT-R and RT-S for each surface are shown in Table 10.

Table 10 Rate of reaction (TOF_DRR), total coke formation (TOF_C_{gen}), total coke removal (TOF_C_{rem}), and coking zone (coke formation or coke removal zone) determined via the ratings concept for metallic, oxide and carbide surface of the Ni catalyst at temperature = 1000 K and CO_2/CH_4 feed ratio = 1.0

Surface type	Ratings (%RT)		Log rate = f(RT-S, RT-R)			
	RT-S	RT-R	TOF_DRR	TOF_C_{gen}	TOF_C_{rem}	Coking zone
Ni(100)	59	112	7.9	6.0	2.3	Formation
Ni(111)	100	100	4.8	-0.1	1.4	Removal
Ni(211)	68	108	7.2	4.6	2.0	Formation
NiO(100)	136	37	2.1	-0.7	-0.6	Removal
NiO(111)-p(2x2)	85	76	5.9	2.0	-0.21	Formation
Ni$_3$C(001)	82	104	6.2	2.5	1.7	Formation

RT-S = average stability rating of the surface (%RT)
RT-R = average reactivity rating of the surface (%RT) (Definition of the RT-S and RT-R can be referred to [73])
TOF_DRR refer to log rates of the dry reforming reaction of methane (DRR)
TOF_C_{gen} refer to log rate of coke formation from CH* and CO* species only
TOF_C_{rem} refer to log rates of coke removal via H* and O* species only

From Table 10, the reactivity for the metallic and the carbide surfaces are observed to be high among all Ni surface types, while for the oxide surface, only the NiO(111)-p(2x2)

is reactive enough, in contrast to an inactive NiO(100) surface. Besides, NiO(100) is reported elsewhere to be inactive for the activation of the C-H bond in methane, thus it may be less active for DRR[74].

On the stability, both formation and removal of coke were considered. The coke formation reactions included the production of atomic carbon from both CH*, CO* species and the Boudouard reaction, while for the coke removal reactions, the coke removed via H*, O* and CO_2 (reverse-Boudouard reaction) were considered. As for the stability criteria of a surface, it should possess a higher rate of coke removal than formation. Therefore, if the catalyst has a higher total rate of coke removal than formation, it would be considered to be in the coke removal zone. This zone is the net rate of coking is coke removal at all time at this pseudo steady-state, whereas in the coke formation zone, the rate of coke formation is higher than removal at all times. It was found that the surfaces that satisfy these criteria are the Ni(111) for metallic and NiO(100) for oxide surfaces, respectively, while all the carbide surfaces fail. Accounting for reactivity and stability criteria, it can be observed that for the metallic surfaces, although all of them promotes high DRR rate, only the Ni(111) is coke-resistant. So, for the design of a reactive-stable dry reforming catalyst, Ni(111) is considered as a good candidate for the metallic surface, whereas for the carbide surface, despite exhibiting a high rate of reaction, it is not coke-resistant at all. This can answer why the carbide although being such a reactive surface would slow down the reaction during the DRR. It is because although the carbide active site has a high rate per site, it promotes high coke formation. Thus, the coke would accumulate on the active sites, reducing the number of active sites and total rate of reaction but not the turnover rate per site. In the case of the oxide surface, it was indicated that the NiO(111)-p(2x2) is the reactive facet but as its rate

of coke formation exceeds the removal, it is not coke-resistant, in contrast to the

coke-resistant but less active NiO(100).

Table 11 Changes in the rate of reaction (TOF_DRR), total coke formation (TOF_C$_{gen}$) and total coke removal (TOF_C$_{rem}$) when surface transforms at temperature = 1000 K and CO$_2$/CH$_4$ feed ratio = 1.0

Route*	Log Rate change (%)**		
	TOF_DRR	TOF_C$_{gen}$	TOF_C$_{rem}$
(1) Ni(100)→NiO(100)	-	-	-
(1) Ni(111)→NiO(111)-p(2x2)	+	+	-
(2) Ni(111)→Ni3C(001)	+	+	+
(3) Ni₃C(001)→NiO(111)-p(2x2)	-	-	-
(4) NiO(100)→Ni(100)	+	+	+
(4) NiO(111)-p(2x2)→Ni(111)	-	-	+
(5) Ni₃C(001)→Ni(111)	-	-	-
(6) NiO(111)-p(2x2)→Ni₃C(001)	+	+	+

* Route number in the parenthesis (#) refers directly to the Surface transformation network in Figure 16 (surface1 → surface2 refers to the surface transformation route that starts with surface1 and ends as surface2 when the surface transformation process is complete)
** The calculation of Log Rate change uses the rate from Table 4 using the simple percentage changes as: Log Rate change$_{surf1→surf2}$ (%) = (Log Rate$_{surface,2}$- Log Rate$_{surface,1}$)/ Rate$_{surface,1}$, where positive (+) and negative (-) signs mean rate increase and decrease, respectively.

According to this study, one can realize that not only the type of Ni phase matters

but the way it arranges, e.g., (111), (100), etc. would alter the performance of the catalyst.

To emphasize, it is not always that the pure metallic surface on the Ni catalyst would help

to promote the main reaction. This is because although all of the metallic Ni has a high rate

of reaction, the one that has low coke-resistance such as Ni(100) would promote coking

which would block the active sites, thus lowering the total DRR rate and deactivating the catalyst. With respect to this part, the next section discusses how the evolution of the surface via transformation such as oxidation and carburization on Ni would affect the performance of the catalyst.

Thereafter, we analyzed how the reactivity and stability in terms of DRR, coke formation and coke removal rates changed as a result of surface transformations as illustrated in Figure 16. For the fresh Ni catalyst, the surface was modeled as the metallic surface of Ni[46]. At the initial stage of the reaction, the surface would experience a transformation via either oxidation or carburization depending on the adsorbates. After the oxide and carbide form as a result of these two processes, it could transform back to the metallic Ni via deoxygenation and decarburization, respectively. According to this, the effects of oxidation, deoxygenation, carburization, and decarburization routes on catalyst performance are discussed as follows.

1. For the transformation route 1&4 (oxidation-deoxygenation), the oxidation route of the metallic Ni surface to form Ni oxide labeled as route 1 in Figure 16 occurs during the reaction between the metallic surface and oxygen atoms that are generated from the dissociation of CO_2 reactant [71]. This route is modeled on two different facets, which are the (100) facet describing the transformation of Ni(100) to NiO(100) and the (111) facet illustrating the Ni(111) facet transforming to NiO(111) that finally undergoes octopolar surface reconstruction and forms the NiO(111)-p(2x2) [52, 53]. Referring to Table 11, it is found that for the oxidation on the (100) facet (Ni(100)→NiO(100)), the oxide shows lower reactivity than the metallic surface, while on coke-resistance, although the log rate of coke removal is low on the oxide,

it is higher than the coke formation resulting in the coke-resistant surface. Thus, the oxidation on the (100) facet would lower the reactivity but enhance coke-resistance. On the (111) facet, the Ni(111)→NiO(111)-p(2x2) route, although the reactivity would slightly increase, the system is not coke-resistant due to an increase in coke formation and a decrease in coke removal. It can be clearly seen that for the oxidation route 1 of the Ni catalyst, if it takes place on the (100) facet, the resulting oxide surface would be less reactive but still coke-resistant. In the case of the (111) facet, the catalyst surface would be more reactive but more prone to coke deposition. In summary, for the oxidation route 1, it should be highlighted that the degree of reduction on the catalyst from an oxide to a metallic surface obtained in the reduction step of catalyst preparation may affect directly the performance of the catalyst. To emphasize, the poor reduction on the (100) facet would lead to a surface with a high amount of NiO(100) compared to Ni(100) making the characteristics of the catalyst become more oxide-like which has high coke-resistance but less reactive. In contrast, if a poor reduction occurs on the (111) facet, the catalyst would be more active but not coke-resistant. Hence, coke-resistant Ni catalysts should have a high degree of oxidation on the (100) facet, but low on the (111) facet.

2. In the case of transformation route 2&5 (carburization-decarburization), when the DRR begins, the metallic Ni phase can transform to carbide via the carburization denoted as route 2 in the surface transformation network of Figure 16, by the reaction between the surface and adsorbed carbon atoms formed via CH_4 and CO_2 dissociations[21]. The changes in catalyst performance due to this route are presented in Table 11. They are observed on the (111) facet, where the models of metallic and

carbide surfaces are chosen to be Ni(111) and Ni₃C(001) as they are analogous surfaces. This is due to that if all the carbon atoms are removed from the Ni₃C(001), the resulting structure will be Ni(111) [6]. The carbide surface is observed experimentally to have high reactivity but low stability [60, 61]. This characteristic is obvious from Table 11. When the Ni(111) transforms to Ni₃C(001), the rate of reaction rises, while there is a decrease in coke-resistance due to a great increase in coke formation from log rate of -0.20 to 2.5. Although the coke removal did increase, its value of 1.7 is lower than coke formation resulting in more coke formation than removal, thus, not coke-resistant. In conclusion, the formation of the carbide would enhance the catalyst's reactivity but lower the coke-resistance by promoting high coke formation.

3. Lastly, the transformation route 3&6 (oxide-to-carbide & carbide-to-oxide), the transformation route 3 represents the situation where the carbide transforms to the oxide surface. Evidence supporting such route has been observed by Yuan et al.[63] They showed that the $CO_2(g)$ reactant could react and eliminate the Ni carbide portion on the sample. This was confirmed by the absence of a Ni_xC peak at 283.6 eV measured by a Near Ambient Pressure X-ray Photoelectron Spectroscopy (NAP-XPS). Furthermore, the excess oxygen atoms produced from CO_2 can initiate the oxidation of the surface resulting in the formation of the oxide surface. Note that this event could be considered if the metallic surface is formed via the elimination of carbide but instantly oxidized as soon as the metallic phase forms. To model this event, let us consider the (111) facet, where the Ni₃C(001) and NiO(111)-p(2x2) are chosen as the starting and final structures of this route, respectively since both (111)

surfaces are structurally analogous to the Ni(111). It is found that the transformation from carbide to oxide would lower the reactivity but enhance the stability as coke formation was suppressed while coke removal was promoted. In contrast, the route 6 represents the transformation of oxide to carbide which was demonstrated by Cocke et al.[71]. The authors showed that the decomposition of the Ni oxide under the presence of adsorbed carbon atoms on the surface can lead to the formation of Ni carbide. As a result, (refer to Table 5), if the surface transforms from oxide to carbide, it would be more reactive but less coke-resistant since the coke formation rises while the coke removal falls. This again confirms the high reactivity but low coke-resistance of the carbide and the high stability but low reactivity of the oxide.

According to routes 1 to 6, the formations of both oxide and carbide phases from the fresh catalyst surface of metallic Ni are possible. Thus, it is demonstrated that the control over the degree of oxidation and carburization of Ni catalysts may allow us to adjust the reactivity and coke-resistance of the catalyst. In order to get a better understanding of how much the degree of oxidation and carburization would have to be in order to achieve reactive and stable system of catalyst, reactivity and coke resistance as a function of surface composition as the ratio of metallic to oxide and carbide of Ni, were studied in the following section through the interpretation of the ternary contour plot (TCP).

6.4. Effects of phase composition on catalysts performance

Up to now, each surface type of Ni contributing to the DRR has been characterized by its coke formation/removal behavior, reactivity, and stability.
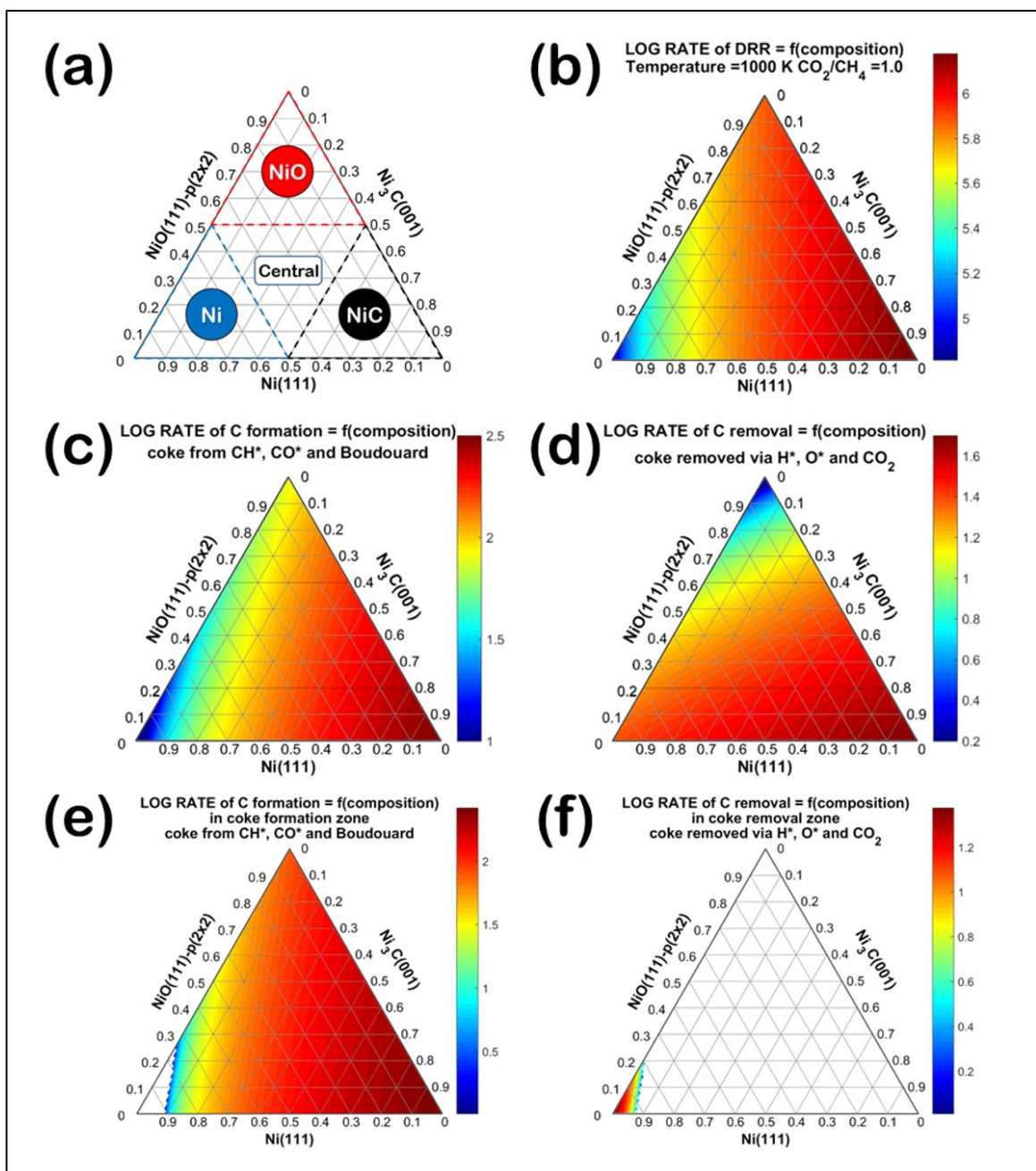
Figure 21 Ternary contour plot as a function of surface composition of (a) dominant surface region, where the labels in each zone indicate the surface which comprise more than 50 % of all surface types, (b) log rate of DRR , (c) log rate of all coke formation reactions, (d) log rate of all coke removal reactions, (e) log net rate of coke formation in the coke formation zone and (f) log net rate of coke removal in the coke removal zone, where all TCPs are constructed at an operating condition of 1000 K, a unity CO_2/CH_4 ratio

In addition, this section determined surface compositions of Ni catalysts represented by the ratio of metallic/oxide/carbide of Ni, which exhibit high reactivity while being coke-resistant via the interpretation of the ternary contour plot (TCP) shown in Figure 21 illustrating the reaction rate of interest as a function of metallic/oxide/carbide ratio.

First, the (111) facet is chosen to represent the reaction and coking schemes, in which the metallic, oxide, and carbide surfaces are modeled by Ni(111), NiO(111)-p(2x2) and $Ni_3C(001)$ slab models, respectively. Additionally, the reaction condition is 1000 K and a unity CO_2/CH_4 feed ratio. To interpret the TCP, first, we classify the region into four main regions shown in Figure 21(a). There are three regions of the dominant surface which are red for oxide-dominant, blue for metallic-dominant, and black for carbide-dominant. The surface composition in the three dominant regions represents a catalyst's surface with more than 50 % of that dominant surface. The last region labeled as "central" region is where the surface would have a comparable fraction of each surface type.

In order to calculate the rate in each TCP, we first obtain the rate of all elementary step on each surface using the rating concept[73] prior to the calculation of the weighted average rate via the following equation. Here, the calculation of weighted rate was used by Fan et al.[5] was used to predict the DRR rate on a Ni catalyst of truncated octahedron shape as a function of Ni(111), Ni(100) and Ni(211) surface fraction (the term r_i is the weighted average the ith reaction rate, f_k is the fraction of surface type k, where the k equals metallic, oxide and carbide of Ni, and the $r_{i,k}$ is the ith reaction rate on surface type k).

$$r_i = \sum_{k=1}^{3} f_k r_{i,k} = f_{Ni} r_{i,Ni} + f_{NiO} r_{i,NiO} + f_{NiC} r_{i,NiC} \qquad \text{Equation 41}$$

Thereafter, by applying this equation, we obtain the DRR rate, coke formation, coke removal, net coke formation in a coke formation zone, and net coke removal in a coke removal zone plotted in Figure 21(b) to (f), respectively. According to the results, on this (111) facet of the Ni catalyst, high reactivity in terms of DRR rate in Figure 21(b). High reactivity is observed when the surface has high fractions of carbide and oxide, while the most reactive region is in the carbide-dominant region. On coke-resistance, when we analyze the coke formation, we found that the carbide-dominant surface has the highest rate of coke formation despite being the most reactive, whereas the metallic Ni(111) exhibits the lowest coke formation among the others. Analysis on the coke removal revealed that both metallic and carbide display high coke removal rate compared to the oxide.

The following question arises: why is that in the experiment[60, 61] carbide would not be coke-resistant although it possesses a high rate of coke removal? This can be answered by analyzing the coke formation and removal zone in Figure 21(e) and (f), respectively. The coke formation zone is calculated via the difference in the rate of total coke formation in Figure 21(c) and the total rate of coke removal in Figure 21(d). After the subtraction, any region with a positive difference means that the coke formation is higher than removal, thus, defined as coke formation zone and plotted in Figure 21(e). We can see that there is an uncolored region in the plot. This region represents the situation when the rate of coke removal is higher than formation. Hence, this uncolored region in Figure 21(e) is the coke-removal zone, in which it is plotted into another TCP in Figure 21(f). In addition, any catalyst that locates in the colored region of Figure 21(e) is considered non coke-resistant, whereas the coke-resistant catalysts would fall in the colored region of Figure 21(f).

After analyzing the coke formation and removal zones, it can be clearly seen that the

carbide-dominant surface is in the coke formation zone. This can be described that although it has a high coke removal rate, its coke formation rate is much higher. In addition, it was found that the surface with up to 75 % metallic phase would shift the system out of the coke formation zone. However, it needs up to 80 % to enter the coke removal zone, thus becoming coke-resistant, while all the oxide-dominant surface is not coke-resistant. This finding on the analogous (111) surface suggests that the oxide, NiO(111)-p(2x2) although reactive, it is not coke-resistant since it is located in the coke formation zone. Another aspect that we can determine from these zones is the maximum allowable amount of carbide that the system can hold before losing the coke-resistant property. This can be described in Figure 21(f), depicting the coke removal zone. By reading this colored region, it is found that the maximum amount of carbide surface that is still in the coke removal zone is around 10 % when the rest of the surface is metallic. This suggests that the amount of the active site on a fresh Ni catalyst should not have more than 10 % of the carbide phase on the surface relative to all other surface types in order to be coke-resistant.

However, during the DRR, as the surface transformation occurs, the metallic surface can also transform to carbide via carburization, hence shifting the catalyst composition into the coke formation zone, reducing the coke-resistant property. Therefore, this TCP can be used as a preliminary guideline for the design of a Ni-based catalyst by suggesting appropriate compositions of Ni yielding high reactivity and stability. If these surface compositions could be sustained during the reaction, the catalyst would be reactive and long-lived.

6.5. Conclusions

In this chapter, we investigated how the evolution of the DRR catalyst surface would affect the coke formation/removal behavior, reactivity, and stability of the Ni catalyst together with the appropriate surface composition that the catalyst should have in order to become reactive and stable. On the characteristics of each surface, the metallic and carbide were found to be more prone to coke formation than the oxide since both of them would bind to the alpha coke (C_α) or the C atom strongly. In addition, the C-C condensation reaction which is the initial stage of higher coke formation such as amorphous (C_β) and graphitic coke (C_C) was also investigated. It was demonstrated that the reaction would rapidly proceed on the carbide $Ni_3C(001)$ surface and in the metallic $Ni(111)$ surface but would be suppressed on the oxide surface of $NiO(100)$ and on the metallic $Ni(100)$ due to the presence of high activation barriers.

Furthermore, the behavior of the surface to coke formation/removal during surface transformation was also studied. It was shown that a high degree of oxidation is needed for the binding energy of coke on the partially oxidized metallic Ni surface to converge to the value of pure oxide. On the other hand, during the carburization, only after the first carburization the surface's binding energy would reach the value of pure Ni_3C. Moreover, in the deoxygenation and decarburization routes, the coke binding energy also converges rapidly to the metallic surface only after the first deoxygenation and decarburization of the top surface layer on NiO and Ni_3C, respectively.

On reactivity, all of the metallic, oxide, and carbide surfaces are active, except $NiO(100)$. This low reactivity of $NiO(100)$ is common and has been reported elsewhere [74]. On coke-resistance, the only Ni metallic surface that satisfies the stability criterion is

Ni(111), while the carbide of $Ni_3C(001)$ does not. For the Ni oxide surface, only the NiO(100) surface is considered coke-resistant. The changes in catalyst performance due to surface transformations can be summarized as follows. For the coke-resistant oxide surface, the degree of oxidation on the (100) facet should be high, while on the (111) facet, it should be low, thus, completely reduced to metallic. In the case of carbide surface, a high degree of carburization would increase the catalyst reactivity but raise the coke formation rate; hence, lowering the stability.

In the study of the surface composition that would yield highly reactive and stable DRR catalyst, it was found that for the surface to become coke-resistant, the maximum allowable amount of carbide surface should not exceed 10 % of total surface types. Also, up to 75 % of metallic is needed for the system to escape the coke formation zone, whereas the surface should comprise more than 80 % of metallic phase to be in the coke removal zone. In conclusion, the control over the degree of catalyst surface transformation the catalyst is the key property towards the design the reactive and coke-resistant DRR catalysts.

7. DESIGN PROCEDURE FOR NICKEL-BASED CATALYSTS FOR THE DRY REFORMING REACTION OF METHANE

7.1. The design procedure for DRR catalysts

At the moment, we have demonstrated various tools for the evaluation of catalyst reactivity and coke-resistance through the catalyst analysis in chapter 3 to 6. Thus, this chapter proceeds to the catalyst design, in which the procedure towards DRR catalyst screening and the criteria for good DRR catalysts will be addressed.
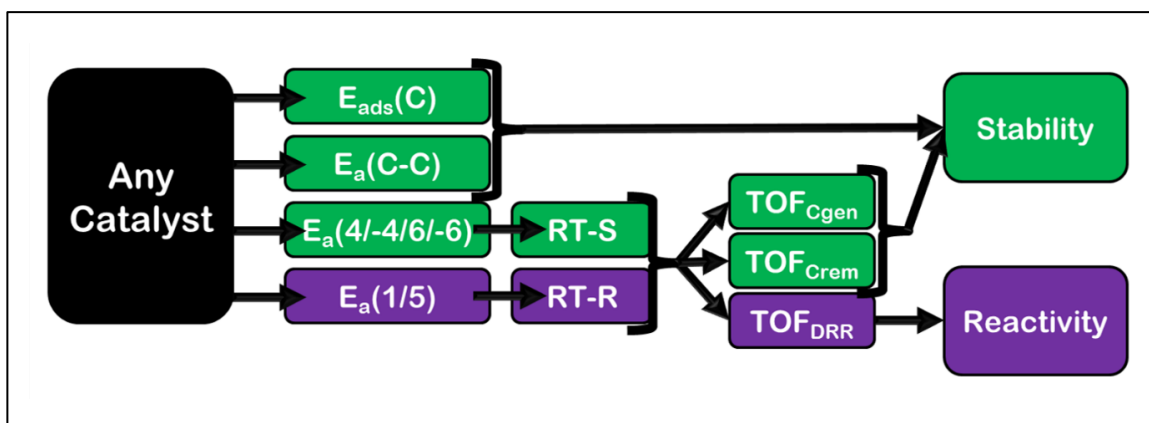
Figure 22 The evaluation of stability and reactivity of DRR catalysts

First of all, to screen whether or not a catalyst of interest is reactive and/or stable, the interpretation on the following parameters entailing adsorption energy (E_{ads}) and sets of activation energies (E_a) shown in Figure 22 are performed.

1. E_{ads} of carbon atom (E_{ads} (C))
2. E_a of C-C condensation reaction (E_a (C-C))

3. E_a of C formation from CH* species (step 4 forward in DRR mechanism, E_a(4))

4. E_a of C removal via H* species (step 4 reverse in DRR mechanism, E_a(-4))

5. E_a of C formation from CO* species (step 6 reverse in DRR mechanism, E_a(-6))

6. E_a of C removal via O* species (step 6 forward in DRR mechanism, E_a(6))

7. E_a of CH_4 1st dissociation step (step 6 forward in DRR mechanism, E_a(1))

8. E_a of CO_2 1st dissociation step (step 6 forward in DRR mechanism, E_a(5))

The first two parameters represent the stability or the coke-resistant properties of the catalyst. To clarify, catalysts with low coke-resistance would possess strong E_{ads}(C) and low activation energy of C-C condensation reaction (E_a(C-C)). This is because strong coke adsorption (in this case it is limited to alpha coke or the atomic carbon adsorption [20]) suggests that whenever coke forms it would attach tightly to the surface blocking the active site, thus, leading to high coke accumulation. In contrast, low E_a(C-C) would facilitate the formation of larger coke initiated by carbon atoms on the catalyst's surface. Thereafter, the rest of the parameters constitute the set of activation energies used to constructed the stability and reactivity ratings (RT-S and RT-R), where both were used to determine the DRR, coke formation and removal rates via the application of the ratings concept constructed in chapter 3. Accordingly, we can now evaluate the stability of the catalyst via its adsorption strength to coke, activation barrier to higher coke formation, coke formation rate and coke removal rate, while describing the reactivity by DRR rate. In addition, one must determine the coking zone via the known coke formation and removal rates, where catalysts that satisfy the coke-resistance criteria must locate in the coke removal zone.
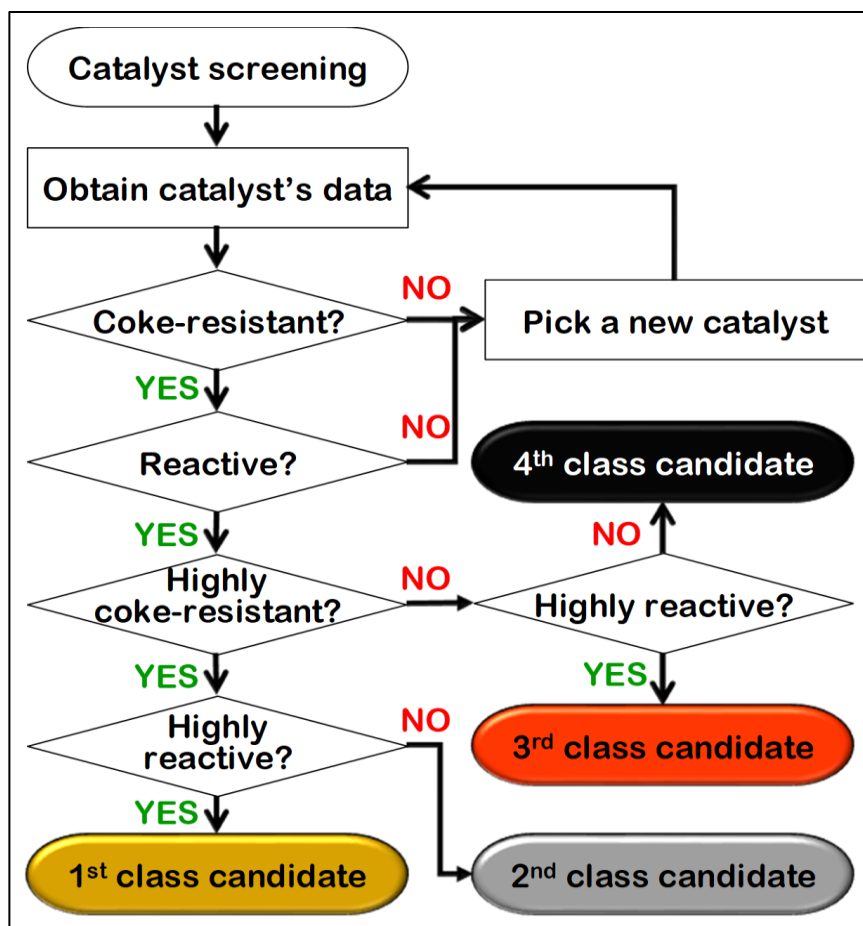
Figure 23 Flow diagram of DRR catalyst design procedure

Since the reactivity and stability of the DRR catalysts are now determined, we will proceed to the catalyst screening procedure illustrated in Figure 23. At first glance, we can see that the screening of stability is always performed before the reactivity because we would like to improve the life of DRR catalysts for lower regeneration and/or replacement costs, so, the catalysts with low coke-resistance are not considered candidates and are screened out in the first step. Additionally, to satisfy the coke-resistance criteria the catalysts must locate in the coke-removal zone, where the rate of coke removal exceeds coke formation. Thereafter, for the reactivity evaluation, inactive catalysts exhibiting lower DRR rate than a

reference catalyst (Ni(111)) are eliminated. Up to this step, the pre-screened catalysts will be classified into four groups: 1st, 2nd, 3rd and 4th class candidates, in which these designations refer to the same raking of DRR catalysts in the ratings concept described in Table 3 of chapter 3.

This classification is carried out in order to prioritize the experimental screening of these candidates. In this screening, they will be further evaluated for both the reactivity in terms of conversion, and stability. The evaluation is done via (1) coke deposition rate calculated from the total amount of measured coke over the reaction time (measured via either temperature-programmed hydrogenation (TPH) or oxidation (TPO)) and (2) conversion over time reflecting how long the catalyst can perform until the conversion significantly decreases, thus, being deactivated.

7.2. Criteria for reactive-stable DRR catalysts

In this section, we analyze the reactivity and stability surfaces (RS and SS) in Figure 24 constructed via the ratings concept for the locations of high reactivity and high coke-resistant at operating temperature of 1000 K and CO_2/CH_4 feed ratio of unity, in which the reactivity ratings (RT-R) and stability ratings (RT-S) at each specified location were retrieved. It was revealed that the reactive regions can be classified into R_1 and R_2 as highly and moderately reactive, respectively as shown in Figure 25, while the coke-resistant regions were categorized into two S_1 and S_2 for highly and moderately coke-resistant, respectively.
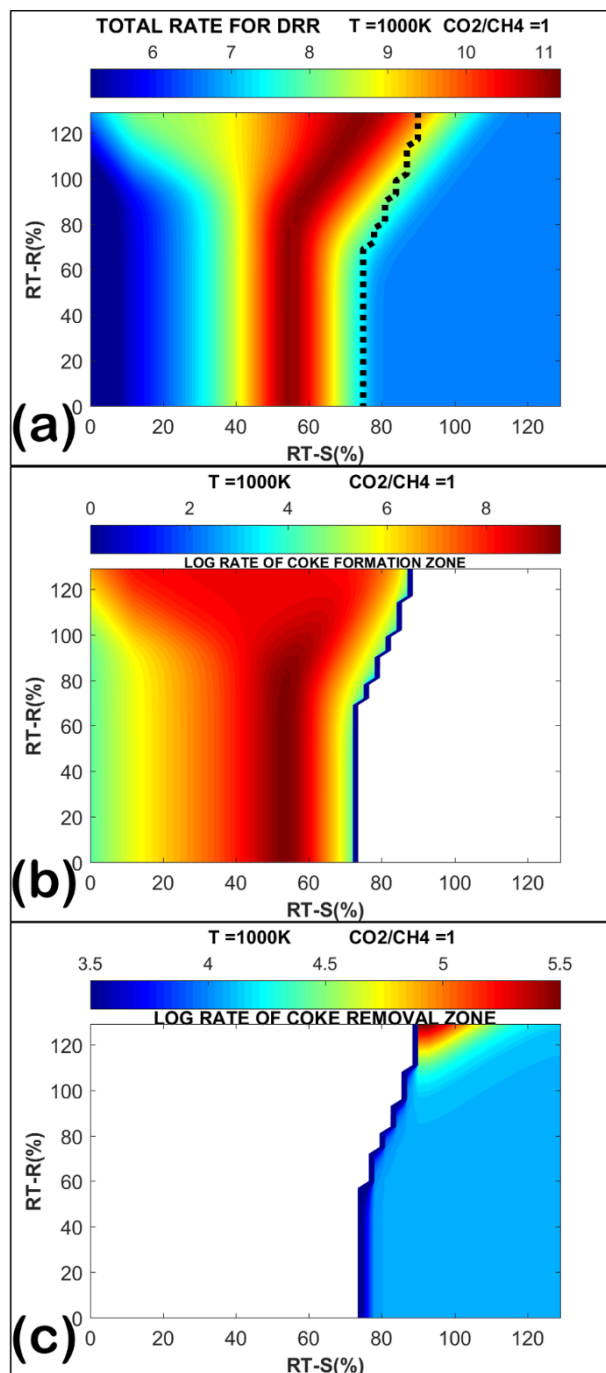
Figure 24 Reactivity surface (RS) as (a) log rate of DRR, and stability surfaces (SS) as (b) log net rate of coke formation in the coke-formation zone, and (c) log net rate of coke removal in the coke-removal zone, all at 1000 K, unity feed ratio, and a reference catalyst of Ni(111)
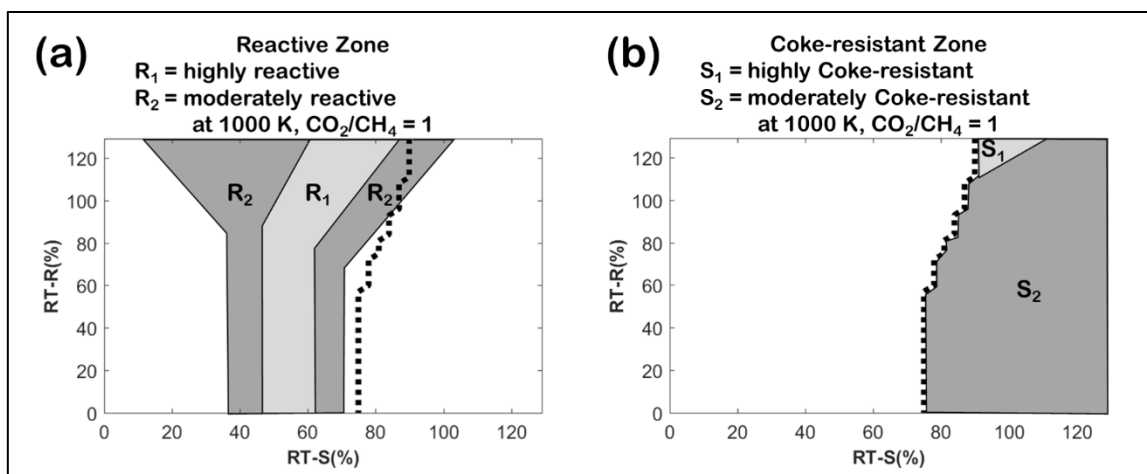
Figure 25 The proposed zones as a function of RT-S and RT-R for (a) reactive zones, which is the locations of high DRR rate classified into R1, highly reactive and R2, moderately reactive zones, and (b) coke-resistant zones that is the locations the coke-removal zone with high net coke removal rates designated as S1, highly coke-resistant and S2, moderately coke-resistant zones, in which the dotted line is the coking boundary

In the reactive regions, a highly reactive region (R_1) is completely located on the left side of the coking boundary, the coke-formation zone. This suggested that catalysts of highest reactivity could not satisfy the coke-resistant criteria, so, the goal to achieve highly reactive and highly coke-resistant DRR catalysts may not be possible since the 1st class candidate is not observed at this operating condition. However, it was found that the moderately reactive region (R_2) expands across the coking boundary into the coke-removal zone, in which this region intersects with the highly coke-resistant region (S_1). As a result, from Figure 25, the 2nd class candidate can be observed in the region of such intersection regarded as reactive-stable zone and can be described as $R_2 \cap S_1$ enclosing the area of RT-S$\in$[90 105] and RT-R$\in$[110 130] depicted in Figure 26.
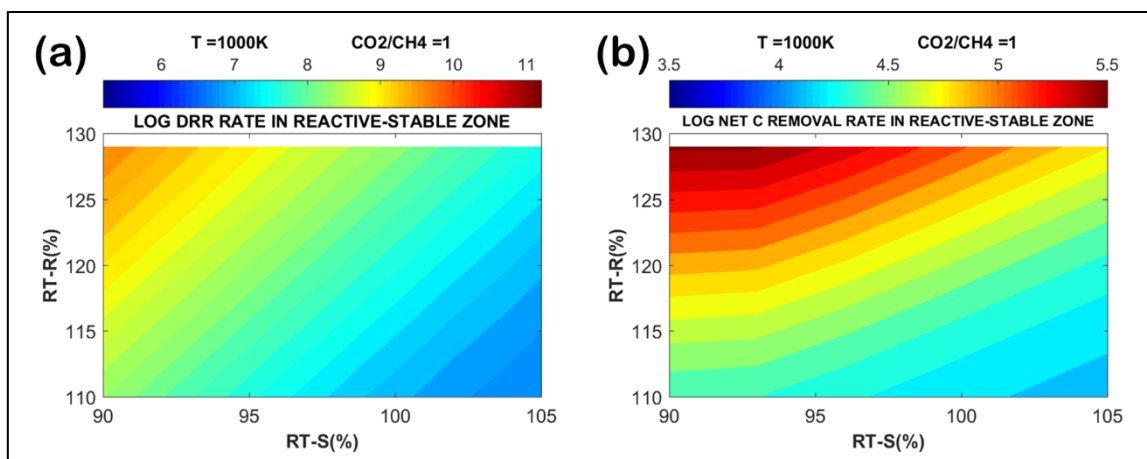
Figure 26 Log rates in the reactive-stable zone (zone $R_2 \cap S_1$) of (a) log rate of the dry reforming reaction of methane and (b) log net rate of coke removal rate

In this reactive-stable region illustrated in Figure 26, the most reactive-stable location is at the highest RT-R (y-axis) but lowest RT-S (x-axis) demonstrating the highest rates of both DRR and net coke removal. This region also represents the suggested values of RT-S and RT-R for the 2nd class candidates. Regarding this, we can translate these values of RT-S and RT-R into the E_a of elementary steps used to construct them. According to the ratings concept, the RT-S represents the E_a of the catalyst in the elementary reaction involving the formation of coke from CH* and CO* and Boudouard reaction, and the removal of coke via H*, O* and reverse-Boudouard reaction, while the RT-R describes the E_a of the catalyst in the activation of CH_4 and CO_2. Therefore, the suggested values of E_a for the 2nd class candidate are calculated and shown in Table 12 below.

Table 12 The activation energies for each elementary step of DRR catalysts in the reactive-stable region

Parameters	Ratings (%RT)		The activation energy of step i (eV)					
	RT-S	RT-R	$E_{a,1}$	$E_{a,5}$	$E_{a,4}$	$E_{a,-6}$	$E_{a,-4}$	$E_{a,6}$
reference catalyst Ni(111)	100	100	0.89	0.67	1.38	3.43	0.81	1.59
Reactive-Stable zone								
Lower limit	90	110	0.4	0.2	1.2	3.3	0.7	1.5
Upper limit	105	130	0.7	0.5	1.5	3.5	1.0	1.7
average	98	120	0.6	0.4	1.3	3.4	0.9	1.6
compared to reference catalyst	lower	higher	lower	lower	lower	lower	higher	higher

In order for the catalysts to be reactive and stable, it was shown that when compared to the reference catalyst, Ni(111), the E_a for the activation of CH_4 ($E_{a,1}$) and CO_2 ($E_{a,5}$), should be less difficult, while the coke formation and coke removal should be around the same tendency. This implied that catalysts which facilitate the activation of the reactants, CH_4 and CO_2, whereas possessing the similar ability to form and removal coke to Ni(111) would be preferred as candidates for good DRR catalysts.

In addition, the 4th class candidates having moderate coke-resistance and reactivity were also observed at this operating condition, in which they located in the region $R_2 \cap S_2$ resulting from the interception between the moderately reactive (R_2, dark gray area that extended into the coke-removal zone on the right side of the coking boundary) and the moderately coke-resistant regions (S_2).
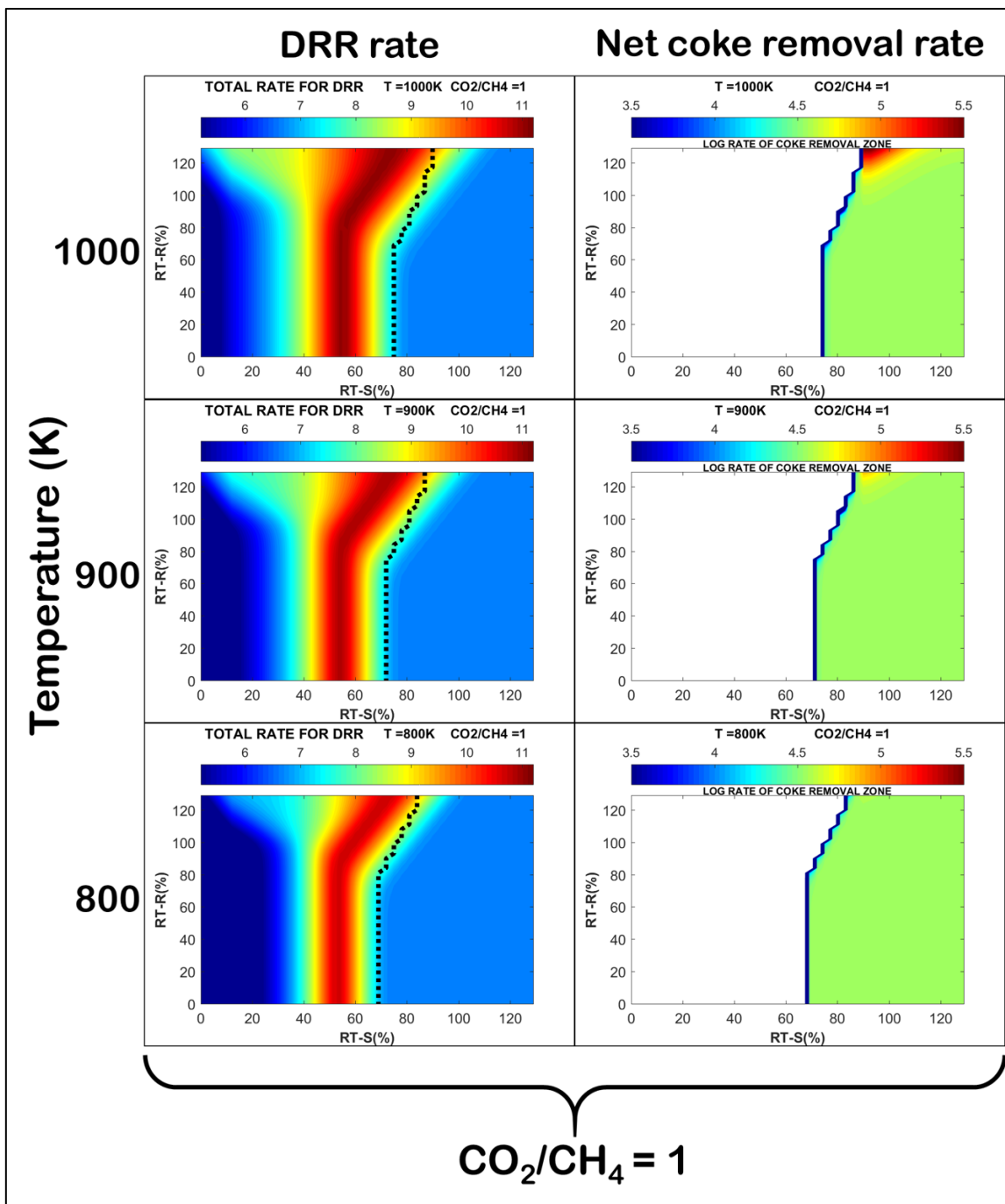
Figure 27 Effects of temperature on the reactive-stable region at a CO_2/CH_4 feed ratio of unity from a temperature of 800 - 1000 K
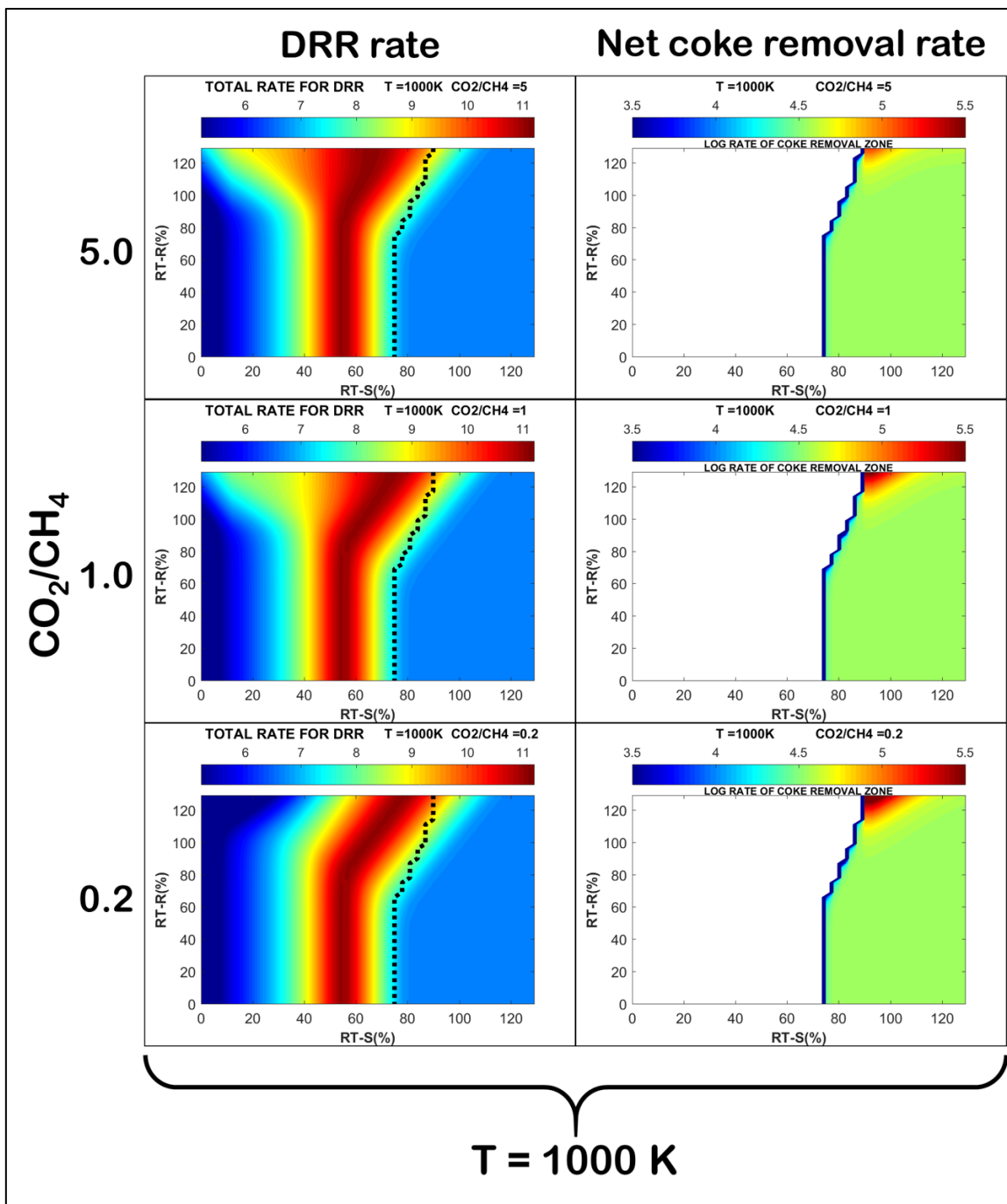
Figure 28 Effects of CO_2/CH_4 feed ratio on the reactive-stable region at temperature = 1000K from CO_2/CH_4 feed ratio of 0.2 - 5.0

Another important factor affecting the DRR catalysts during the reaction is the operating condition described by temperature and CO_2/CH_4 feed ratio. As a result, the effects of these operating parameters on the reactive-stable zone are studied by observing the changes of areas involving with the reactive regions (R_1 and R_2) and the coke-resistant regions (S_1 and S_2). On the effects of temperature, it was found from Figure 27 that low temperature would make all reactive regions ($R_1 \cup R_2$) shrink but this did not change the area of the moderately reactive regions (R_2) that is on the right side of the coking boundary (coke-removal zone), in other words the $R_1 \cup R_2$ decrease but not $R_2 \cap (S_1 \cup S_2)$, whereas for the coke-resistant regions (S_1 and S_2), the highly coke-resistant (S_1) diminished at low temperature and disappeared below 900 K. Therefore, the reactive-stable zone which is found to be in the area of $R_2 \cap S_1$ representing the 2nd class candidates, would disappear at temperature lower than 900 K due to the disappearance of the highly coke-resistant region (R_1), thus, only the 4th class candidate could be observed since the $R_2 \cap S_1$ area becomes $R_2 \cap S_2$. Interestingly, for the adjustment of the feed ratio shown in Figure 28, at a low CO_2/CH_4 ratio (high CH_4 content in the feed), the highly coke-resistant region (S_1) could be broadened. Meanwhile, again only the moderately reactive region (R_2) could be found in the coke removal zone and it is unaffected by the changes in feed ratio. Hence, the reactive-stable zone of 2nd class candidates generated by the interception between R_2 and S_1 designated as $R_2 \cap S_1$ expands and it could shift some of the 4th class candidates to the 2nd class.

As conclusions to the criteria for DRR candidates, the catalysts should be in the reactive-stable zone, where activations of both reactants, CH_4 and CO_2 are easier than Ni(111), while the activation barriers to form and removal coke are more or less the same to

our reference catalyst. From the observation at various operating conditions other than at 1000 K and unity feed ratio, it was found that low temperature would not affect the moderately reactive region that intersects the coke removal zone designated as $R_2 \cap (S_1 \cup S_2)$. However, it would reduce the area of the highly coke-resistant region (S_1). Below 900 K, this S_1 region vanishes resulting in the disappearance of the reactive-stable zone ($R_2 \cap S_1$) and the 2nd class candidate, thus, at low temperature, only the 4th class candidates exist. On the other hand, although low CO_2/CH_4 feed ratio would not affect the $R_2 \cap (S_1 \cup S_2)$ region akin to the effect of low temperature, the enlargement of S_1 region is witnessed at this low feed ratio. At these conditions, the expansion of S_1 could promote some 4th class candidates to the 2nd class, suggesting that some of the 4th class candidates could exhibit high coke-resistant property under low CO_2/CH_4 ratio. Thus, instead of rejecting all 4th class candidates for further experimental screening, one could try analyzing first if some of them could shift to the 2nd class through the control of operating conditions. If so, there should be some possibilities that some of these 4th class candidates could potentially pass the experimental screening in the next step.

One approach to represent the nanoparticle catalyst of different size is via the ratio between the facet metallic surfaces: (111), (100) and (211) if the shape of a truncated octahedron is assumed as illustrated by Blaylock et al. [75] and shown in Table 13. We can estimate the rate of the nanoparticle by the weighted rate as a function of each facet using the same calculation as in Equation 41. Also, one can refer back to our investigation on the rates on different surfaces of Ni-based catalyst that only the Ni(111) is coke-resistant among other metallic surfaces suggesting that the as-prepared or fresh catalyst with high amount of Ni(111) facet would be ideal. Thus, it is proposed that if the controlled synthesis of the

Ni-based DRR catalyst to be Ni(111)-dominant is possible, the reactive-stable property would be achieved.

Table 13 Particle size as a function of facet fraction for the truncated octahedron shape particle

size (nm)	Surface fraction		
	Ni(111)	Ni(100)	Ni(211)
1.25	0.46	0.05	0.49
2.5	0.61	0.12	0.27
3.5	0.69	0.11	0.20
5	0.72	0.13	0.15
7	0.74	0.15	0.11
15	0.79	0.16	0.05

However, the transformation of Ni(111) to $Ni_3C(001)$ is at ease, where the formation of such carbide would promote very high coke formation, hence, lower stability. As a result, the controlled synthesis of Ni(111) should be combined with the control of surface transformation from metallic to carbide in order to ensure high coke-resistant of the Ni-based DRR catalysts.

7.3. Conclusions

The main idea conveyed in the design procedure of reactive and stable DRR catalysts is that the screening for coke-resistant candidates is more important than the reactive ones. This is because catalysts of high resistance to coke formation but low in activity could save the regeneration and replacement cost, thus lowering the total fixed and operational costs of

the DRR process when compared to the ones that are highly reactive but promote coke formation. Further, following the screening procedure, the candidates ready for experimental screening in the next step could be classified into 4 groups as 1st, 2nd, 3rd and 4th class.

However, at typical DRR operating conditions [1] of around 1000 K and unity feed ratio, only the 2nd and 4th class candidates could be observed. As the 2nd class is the best option achievable at this condition, the characteristics for such class is chosen as guideline for reactive and stable DRR catalysts, in which facile activation of both reactants: CH_4 and CO_2 together with the similar ability of coke formation and removal compared to the reference catalyst, Ni(111) is preferred. Moreover, the interchangeability between these two classes has also been observed to be possible under some operating temperature and feed ratio. For instance, at a temperature lower than 900 K, the 2nd class candidate would not exist and only the 4th class ones are found, implying that the increase in temperature could transform the 4th class to 2nd class candidates, thus improving catalyst's stability. On the CO_2/CH_4 feed ratio, high CH_4 content (feed ratio<1.0) could expand the reactive-stable zone ($R_2 \cap S_1$) resulting in the shifting of some 4th to the 2nd class candidates. Therefore, for the screening at such operating condition, the 2nd class candidates are the first priority for further experimental screening, on the other hand, although the 4th class candidates could not perform better than the 2nd class, some of them could transform to the 2nd class under specific operating condition, thus exhibiting some potential as candidates for further experimental screening. Finally, the control synthesis of the catalysts to have a high amount of the Ni(111) facet incorporating the control of surface transformation to carbide is proposed as a key for the reactive and stable Ni-based DRR catalysts.

8. CONCLUSIONS AND RECOMMENDATIONS

8.1. Conclusions

The ratings concept was developed to screen for reactive and stable DRR catalysts via the analysis of reactivity rating (RT-R) and stability rating (RT-S) of the catalyst of interest. The ratings are constructed by rating the sets of activation energies to the reference catalyst on a rating scale. The members in these sets are E_a of C formation from CH*, CO* and Boudouard reaction, and C removal via H*, O* and reverse-Boudouard reaction for the construction of RT-S, and E_a of CH_4 and CO_2 activation reactions in the case of RT-R. By plotting and reading through the index of (RT-S, RT-R) for each catalyst on the reactivity and stability surfaces generated by the total rate of DRR and rate of coke formation-removal, respectively, the reactivity and coke-resistance of the catalysts can be determined. In addition, analysis of the coking zone is also carried out to translate the predicted rate of coke formation and removal into a clear representation of coke-resistant. Regarding this representation, if the (RT-S, RT-R) index of any catalyst falls into the coke formation zone, it would possess higher total rate of coke formation than the removal, thus not coke-resistant, while the coke-resistant catalyst is located in coke removal zone, having higher total rate of coke removal than formation. Therefore, the reactive-stable DRR catalysts should situate at the high DRR rate location on the RS, while being in the coke removal zone at the location of high coke removal rate.

The practical use of the ratings concept has been shown in its extended version. This version interprets reported experimental apparent activation energy of the methane decomposition reaction as an input parameter to determine the rate of coke formation and

removal and predict the trend of coke deposition of Pt and Rh supported catalysts. In these analyses, the experimental data on coke deposition measured by TPH[64] and TPO[14] is used to verify the predicted trend. The concept can predict well the trend of coke deposition rate in the case of Pt but not in the case of Rh supported catalysts. Hence, the improvement of the extended ratings concept is suggested to enhance this one-experimental-parameter model by integrating more information regarding apparent activation energies of the reaction used in the construction of the stability ratings that is the $CO(g)$ dissociation reaction, and the one used to construct the reactivity ratings which is the $CO_2(g)$ dissociation reaction. Therefore, with the proposed full-option procedure, it is expected that the predictive power of the extended ratings concept could be improved. In addition, we must emphasize that for the full-option calculation mentioned above, carrying out such experiments may take time as much as running the DRR reaction testing and time on stream. Thus, we must further optimize the calculation to use the least number of experimental parameters as possible to decrease the time needed to obtain the experimental values but still possessing high predictive power.

On the enhancement of reactivity and coke-resistant property of DRR catalysts, the manipulation of operating conditions has been studied. Four strategies have been proposed based on four types of the catalyst. For Types 1 and 2, the best operating conditions would lead to reactive and stable DRR catalysts, whereas for Type 3, only if the catalyst is located near the coke formation-removal boundary, it could be shifted to Type 1, in which the best operating condition for this type is now the same as type 1. For the Type 4 catalysts, when adjusting to their optimal condition they would become coke-resistant but low in reactivity, where no more modification could be made to shift them into the coke removal zone.

The investigation on the evolution of the catalyst surface during the dry reforming reaction of methane revealed that the behavior to coke, reactivity, and stability of the Ni catalyst changes by means of the changes on surface characteristics and compositions. Metallic and carbide surfaces were shown to be more likely to form than the oxide did since they bind strongly to atomic carbon (alpha coke, C_α). Another determiner of coke-resistant is the activation energy of the C-C condensation reaction. This is because if the value is too low it would facilitate the higher coke formation, e.g., amorphous (C_β) and graphitic coke (C_C) which leads to the accumulation of coke deactivating the active sites and ultimately, the encapsulation of the catalysts. It was found that such reaction easily proceeds on $Ni_3C(001)$ as same as Ni(111) but suppressed on NiO(100) and Ni(100).

The study on the degree of oxidation and carburization of a fresh catalyst surface, designated as Ni(111), is also carried out. When the surface was oxidized from metallic Ni surface to oxide, a high degree of oxidation is needed for the surface to behave like the pure oxide surface. Such degree of oxidation is determined by the value where the binding energy to coke starts to converge to the value of pure oxide when the O/Ni ratio of the system exceeds 0.6. For the carburization, the surface's binding energy reaches the value of pure carbide only after the carburization of the first top layer. In the reverse processes, namely deoxygenation and decarburization routes, the binding energy converges to the value of that the metallic surface only after the first deoxygenation and decarburization of the top surface on NiO and Ni_3C, respectively.

On catalytic performance and coke-resistance of the surface, all except NiO(100) is considered active confirmed by high DRR rate calculated via the ratings concept, whereas only Ni(111) and NiO(100) could satisfy the stability criteria due to their location determined

to be in the coke removal zone. Changes of catalyst performance due to surface transformations suggested that the coke-resistant oxide surface should have a high degree of oxidation on the (100) facet but low on the (111) facet, while a high degree of carburization of the carbide surface increases reactivity but also the coke formation, thus, lower stability.

Study on the reactive and stable surface composition of DRR catalysts via the interpretation of the ternary contour plot (TCP) showed that at the general operating condition of 1000 K and unity feed ratio, the amount of carbide surface should not exceed 10 % of total surface types. Also, it is needed to preserve at least 75 % of metallic surface to avoid the system from being in the coke formation zone, and to enter the coke removal zone more than 80 % of metallic should be acquired.

In the design of reactive and stable DRR catalysts, the screening for coke-resistant candidates is the first priority followed by the reactivity screening, where the candidates are classified as 1st, 2nd, 3rd and 4th class. At typical operating conditions in the dry reforming reaction of methane [1] of 1000 K and unity feed ratio, only the 2nd and 4th class candidates could be observed. Between these classes, it has been shown that under certain operating temperature and feed ratio the interchange from one to another is possible. At the temperatures higher than 900 K, some of the 4th class would transform into 2nd class candidate due to the existence of the highly coke-resistant region (S_1) at high temperature creating the reactive-stable zone ($R_2 \cap S_1$). As a result, the 4th class candidate that falls into such interchange should be prioritized with the same importance as the 2nd class when being arranged for experimental screening in the next step. Ultimately, it is emphasized that the criteria for reactive and stable Ni-based DRR catalysts would be on the controlled synthesis

to have Ni(111) as the dominant surface, while also being able to control over the surface transformation from the metallic to the carbide.

8.2. Recommendation for future works

8.2.1. Development of multi-parameter extended ratings concept

According to the one-experimental-parameter extended ratings concept used to predict the coke deposition trend via the interpretation of the apparent activation energy of methane consumption reaction ($E_{a,app,CH4}$), it has shown that the predictive power is still low. Furthermore, it needed improvement by incorporating other related apparent E_a of reactions such as CO_2 decomposition ($E_{a,app,CO2}$) and CO decomposition ($E_{a,app,CO}$). To explain this, previously, we used only $E_{a,app,CH4}$ to derive (1) the reactivity rating (RT-R) as the Y index on the plot, and (2) the rate of methane consumption, $\log_{10}(r_{CH_4})$ via Equation 37 on page 35. This recommended improved version would include $E_{a,app,CO2}$ in the calculation of the RT-R, and $E_{a,app,CO}$ for the calculation of the RT-S. We expected this multi-parameter model to be more predictive than the previous version.

8.2.2. Effects of particle size on the performance of DRR catalysts

As it is shown that the ternary contour plot (TCP) gave us a clearer picture for the determination of the surface composition needed to avoid coke formation, thus, improving coke-resistance, the plot can be applied further to study the effects of particle size on catalyst performance. The study should focus on how the size of the Ni metallic particle affect the DRR rate, coke formation and coke removal rates, including the coking boundary. To represent the particle size in the TCP we must refer back to the construction of the plot first.

Since in the case of surface composition study, the plotted rate on each TCP is a function of three parameters (fraction of metallic, oxide and carbide surface), where the rate at each corner of the TCP is the rate of each pure surface. Likewise, for the particle size, we should use the ratio between the Ni(111), Ni(211) and Ni(100) to represent the size of the catalyst of truncated octahedron shape due to that these fractions change as a function of the particle size[75] as shown in Table 13. With respect to this, the rate as a function of particle size can be determined, where this predicted value will be cross-checked with the experimental data.

8.2.3. Incorporation of an equilibrium coking scheme

As we applied the pseudo steady state hypothesis (PSSH) to our ratings concept, the net rate of reaction for each reactive intermediate is assumed to be zero and the coking was described at steady state. However, since reactions generating and removing coke may reach equilibrium anytime during the DRR, the prediction of coking at equilibrium should also be considered in addition to the PSSH. Now for the catalysts to be stable, the prediction from both approaches should agree and characterize the catalyst's surface as coke-resistant.

8.2.4. Applications for real-time process optimizations

Since the ratings concept enables us to determine the optimal temperature and CO_2/CH_4 feed ratio for a given catalyst at changing operating conditions, it would be very useful to integrate the concept into the process optimization by working in real-time with the dry reforming reactor unit. For instance, if the feed ratio and/or temperature of the feed changes anytime during the process, the concept will be used in real-time to determine the optimal operating temperature and feed ratio to sustain the same catalyst performance.

REFERENCES

[1] J.H. Edwards, A.M. Maitra, The Chemistry of Methane Reforming with Carbon-Dioxide and Its Current and Potential Applications, Fuel Processing Technology, 42 (1995) 269-289.

[2] M.E. Dry, The Fischer-Tropsch process: 1950-2000, Catalysis Today, 71 (2002) 227-241.

[3] Y.A. Zhu, D. Chen, X.G. Zhou, W.K. Yuan, DFT studies of dry reforming of methane on Ni catalyst, Catalysis Today, 148 (2009) 260-267.

[4] J. Wei, E. Iglesia, Isotopic and kinetic assessment of the mechanism of reactions of CH_4 with CO_2 or H_2O to form synthesis gas and carbon on nickel catalysts, Journal of Catalysis, 224 (2004) 370-383.

[5] C. Fan, Y.-A. Zhu, M.-L. Yang, Z.-J. Sui, X.-G. Zhou, D. Chen, Density Functional Theory-Assisted Microkinetic Analysis of Methane Dry Reforming on Ni Catalyst, Industrial & Engineering Chemistry Research, 54 (2015) 5901-5913.

[6] Z.Y. Wang, X.M. Cao, J.H. Zhu, P. Hu, Activity and coke formation of nickel and nickel carbide in dry reforming: A deactivation scheme from density functional theory, Journal of Catalysis, 311 (2014) 469-480.

[7] D. San-José-Alonso, J. Juan-Juan, M.J. Illán-Gómez, M.C. Román-Martínez, Ni, Co and bimetallic Ni–Co catalysts for the dry reforming of methane, Applied Catalysis A: General, 371 (2009) 54-59.

[8] M.C.J. Bradford, M.A. Vannice, Catalytic reforming of methane with carbon dioxide over nickel catalysts II. Reaction kinetics, Applied Catalysis A: General, 142 (1996) 97-122.

[9] B. Djebarri, V.M. Gonzalez-Delacruz, D. Halliche, K. Bachari, A. Saadi, A. Caballero, J.P. Holgado, O. Cherifi, Promoting effect of Ce and Mg cations in Ni/Al catalysts prepared from hydrotalcites for the dry reforming of methane, Reaction Kinetics, Mechanisms and Catalysis, 111 (2014) 259-275.

[10] J.L. Lu, B. Liu, J.P. Greeley, Z.X. Feng, J.A. Libera, Y. Lei, M.J. Bedzyk, P.C. Stair, J.W. Elam, Porous Alumina Protective Coatings on Palladium Nanoparticles by Self-Poisoned Atomic Layer Deposition, Chemistry of Materials, 24 (2012) 2047-2055.

[11] B. Qiao, A. Wang, X. Yang, L.F. Allard, Z. Jiang, Y. Cui, J. Liu, J. Li, T. Zhang, Single-atom catalysis of CO oxidation using Pt1/FeOx, Nature Chemistry, 3 (2011) 634-641.

[12] S. Praserthdam, B. Jongsomjit, Observation on Different Turnover Number in Two-phase Acid-catalyzed Esterification of Dilute Acetic Acid and 1-Heptanol, Catalysis Letters, 130 (2009) 583-587.

[13] S. Praserthdam, P. Wongmaneenil, B. Jongsomjit, Investigation of different modifiers for nanocrystal zirconia on W/ZrO2 catalysts via esterification, Journal of Industrial and Engineering Chemistry, 16 (2010) 935-940.

[14] S. Srihiranpullop, P. Praserthdam, A new approach of coke characterization on metal and support for Pt/Al_2O_3 by combination of Al_2O_3 and Pt/SiO_2, Catalysis Today, 93-95 (2004) 723-727.

[15] P.G. Menon, Coke on Catalysts - Harmful, Harmless, Invisible and Beneficial Types, Journal of Molecular Catalysis, 59 (1990) 207-220.

[16] C.H. Bartholomew, Mechanisms of catalyst deactivation, Applied Catalysis A: General, 212 (2001) 17-60.

[17] A.H. Motagamwala, J.A. Dumesic, Analysis of reaction schemes using maximum rates of constituent steps, Proceedings of the National Academy of Sciences of the United States of America, 113 (2016) E2879-E2888.

[18] C. Stegelmann, A. Andreasen, C.T. Campbell, Degree of Rate Control: How Much the Energies of Intermediates and Transition States Control Rates, Journal of the American Chemical Society, 131 (2009) 8077-8082.

[19] J. Greeley, Theoretical Heterogeneous Catalysis: Scaling Relationships and Computational Catalyst Design, Annual Review of Chemical and Biomolecular Engineering, Vol 7, 7 (2016) 605-635.

[20] C.H. Bartholomew, Carbon Deposition in Steam Reforming and Methanation, Catalysis Reviews-Science and Engineering, 24 (1982) 67-112.

[21] L.J.E. Hofer, E.M. Cohn, W.C. Peebles, The Isothermal Decomposition of Nickel Carbide, The Journal of Physical and Colloid Chemistry, 54 (1950) 1161-1169.

[22] I. Czekaj, F. Loviat, F. Raimondi, J. Wambach, S. Biollaz, A. Wokaun, Characterization of surface processes at the Ni-based catalyst during the methanation of biomass-derived synthesis gas: X-ray photoelectron spectroscopy (XPS), Applied Catalysis A: General, 329 (2007) 68-78.

[23] P. Weinberger, Revisiting Louis de Broglie's famous 1924 paper in the Philosophical Magazine, Philosophical Magazine Letters, 86 (2006) 405-410.

[24] E. Schrödinger, Quantisierung als Eigenwertproblem, Annalen der Physik, 384 (1926) 361-376.

[25] J.G. Lee, Computational Materials Science: An Introduction, Second Edition, CRC Press, 2016.

[26] D. Sholl, J.A. Steckel, Density Functional Theory: A Practical Introduction, Wiley, 2009.

[27] W. Kohn, L.J. Sham, Self-Consistent Equations Including Exchange and Correlation Effects, Physical Review, 140 (1965) A1133-A1138.

[28] W. Pauli, Über den Zusammenhang des Abschlusses der Elektronengruppen im Atom mit der Komplexstruktur der Spektren, Zeitschrift für Physik, 31 (1925) 765-783.

[29] P.E. Blöchl, Projector augmented-wave method, Physical Review B, 50 (1994) 17953-17979.

[30] G. Kresse, Ab-Initio Molecular-Dynamics for Liquid-Metals, Journal of Non-Crystalline Solids, 193 (1995) 222-229.

[31] G. Kresse, J. Furthmuller, Efficient iterative schemes for ab initio total-energy calculations using a plane-wave basis set, Physical Review B, 54 (1996) 11169-11186.

[32] G. Kresse, J. Furthmuller, Efficiency of ab-initio total energy calculations for metals and semiconductors using a plane-wave basis set, Computational Materials Science, 6 (1996) 15-50.

[33] G. Kresse, J. Hafner, Ab-Initio Molecular-Dynamics Simulation of the Liquid-Metal Amorphous-Semiconductor Transition in Germanium, Physical Review B, 49 (1994) 14251-14269.

[34] J.P. Perdew, K. Burke, M. Ernzerhof, Generalized gradient approximation made simple, Physical Review Letters, 77 (1996) 3865-3868.

[35] J.P. Perdew, K. Burke, M. Ernzerhof, Generalized gradient approximation made simple (vol 77, pg 3865, 1996), Physical Review Letters, 78 (1997) 1396-1396.

[36] H.J. Monkhorst, J.D. Pack, Special Points for Brillouin-Zone Integrations, Physical Review B, 13 (1976) 5188-5192.

[37] M. Methfessel, A.T. Paxton, High-Precision Sampling for Brillouin-Zone Integration in Metals, Physical Review B, 40 (1989) 3616-3621.

[38] V.I. Anisimov, J. Zaanen, O.K. Andersen, Band theory and Mott insulators: Hubbard U instead of Stoner I, Physical Review B, 44 (1991) 943-954.

[39] C. Ebensperger, B. Meyer, First-principles study of the reconstruction and hydroxylation of the polar NiO(111) surface, physica status solidi (b), 248 (2011) 2229-2241.

[40] A. Rohrbach, J. Hafner, G. Kresse, Molecular adsorption on the surface of strongly correlated transition-metal oxides: A case study for CO/NiO(100), Physical Review B, 69 (2004) 075413.

[41] O. Bengone, M. Alouani, P. Blöchl, J. Hugel, Implementation of the projector augmented-wave LDA+U method: Application to the electronic structure of NiO, Physical Review B, 62 (2000) 16392-16401.

[42] O. Bengone, M. Alouani, J. Hugel, P. Blöchl, LDA+U calculated electronic and structural properties of NiO(001) and NiO(111) p(2×2) surfaces, Computational Materials Science, 24 (2002) 192-198.

[43] W.-B. Zhang, B.-Y. Tang, Stability of the polar NiO(111) surface, The Journal of Chemical Physics, 128 (2008) 124703.

[44] G. Henkelman, B.P. Uberuaga, H. Jonsson, A climbing image nudged elastic band method for finding saddle points and minimum energy paths, Journal of Chemical Physics, 113 (2000) 9901-9904.

[45] G. Henkelman, H. Jonsson, Improved tangent estimate in the nudged elastic band method for finding minimum energy paths and saddle points, Journal of Chemical Physics, 113 (2000) 9978-9985.

[46] S. Nahreen, S. Praserthdam, S.P. Beltran, P.B. Balbuena, S. Adhikari, R.B. Gupta, Catalytic Upgrading of Methane to Higher Hydrocarbon in a Nonoxidative Chemical Conversion, Energy & Fuels, 30 (2016) 2584-2593.

[47] G. Ramos-Sanchez, S. Praserthdam, F. Godinez-Salomon, C. Barker, M. Moerbe, H.A. Calderon, L.A. Lartundo, M.A. Leyva, O. Solorza-Feria, P.B. Balbuena, Challenges of modelling real nanoparticles: Ni@Pt electrocatalysts for the oxygen reduction reaction, Physical Chemistry Chemical Physics, 17 (2015) 28286-28297.

[48] S. Praserthdam, P.B. Balbuena, Effects of oxygen coverage, catalyst size, and core composition on Pt-alloy core-shell nanoparticles for oxygen reduction reaction, Catalysis Science & Technology, 6 (2016) 5168-5177.

[49] M.G. Jiao, K. Li, W. Guan, Y. Wang, Z.J. Wu, A. Page, K. Morokuma, Crystalline Ni3C as both carbon source and catalyst for graphene nucleation: a QM/MD study, Scientific Reports, 5 (2015).

[50] S.G. Josh, U. Jamal, R.C. Thomas, K.B. Nelli, K.W. Angela, First-principle study of structure and stability of nickel carbides, Journal of Physics: Condensed Matter, 22 (2010) 445503.

[51] C.A.J. Fisher, Molecular dynamics simulations of reconstructed NiO surfaces, Scripta Materialia, 50 (2004) 1045-1049.

[52] D. Wolf, Reconstruction of NaCl surfaces from a dipolar solution to the Madelung problem, Physical Review Letters, 68 (1992) 3315-3318.

[53] H. Kuhlenbeck, S. Shaikhutdinov, H.-J. Freund, Well-Ordered Transition Metal Oxide Layers in Model Catalysis – A Series of Case Studies, Chemical Reviews, 113 (2013) 3986-4034.

[54] L. Foppa, M.-C. Silaghi, K. Larmier, A. Comas-Vives, Intrinsic reactivity of Ni, Pd and Pt surfaces in dry reforming and competitive reactions: Insights from first principles calculations and microkinetic modeling simulations, Journal of Catalysis, 343 (2016) 196-207.

[55] H. Eyring, The Activated Complex in Chemical Reactions, The Journal of Chemical Physics, 3 (1935) 107-115.

[56] X.-M. Cao, R. Burch, C. Hardacre, P. Hu, An understanding of chemoselective hydrogenation on crotonaldehyde over Pt(111) in the free energy landscape: The microkinetics study based on first-principles calculations, Catalysis Today, 165 (2011) 71-79.

[57] J. Cheng, P. Hu, Utilization of the Three-Dimensional Volcano Surface To Understand the Chemistry of Multiphase Systems in Heterogeneous Catalysis, Journal of the American Chemical Society, 130 (2008) 10868-10869.

[58] E.G.M. Kuijpers, A.J.H.M. Kock, M.W.C.M.A. Nieuwesteeg, J.W. Geus, Disproportionation of CO on $NiSiO_2$: Kinetics and nature of the deposited carbon, Journal of Catalysis, 95 (1985) 13-20.

[59] D.L. Trimm, Catalysts for the control of coking during steam reforming, Catalysis Today, 49 (1999) 3-10.

[60] J. Rostrup-Nielsen, D.L. Trimm, Mechanisms of carbon formation on nickel-containing catalysts, Journal of Catalysis, 48 (1977) 155-165.

[61] V.C.H. Kroll, H.M. Swaan, C. Mirodatos, Methane Reforming Reaction with Carbon Dioxide Over Ni/SiO_2 Catalyst, Journal of Catalysis, 161 (1996) 409-422.

[62] V.C.H. Kroll, H.M. Swaan, S. Lacombe, C. Mirodatos, Methane Reforming Reaction with Carbon Dioxide over Ni/SiO2Catalyst, Journal of Catalysis, 164 (1996) 387-398.

[63] K. Yuan, J.-Q. Zhong, X. Zhou, L. Xu, S.L. Bergman, K. Wu, G.Q. Xu, S.L. Bernasek, H.X. Li, W. Chen, Dynamic Oxygen on Surface: Catalytic Intermediate and Coking Barrier in the Modeled CO2 Reforming of CH4 on Ni (111), ACS Catalysis, 6 (2016) 4330-4339.

[64] M.C.J. Bradford, M.A. Vannice, CO_2 Reforming of CH_4 over Supported Pt Catalysts, Journal of Catalysis, 173 (1998) 157-171.

[65] M.C.J. Bradford, M.A. Vannice, CO_2 reforming of CH_4, Catalysis Reviews - Science and Engineering, 41 (1999) 1-42.

[66] A. Erdohelyi, J. Cserenyi, F. Solymosi, Activation of CH_4 and Its Reaction with CO_2 over Supported Rh Catalysts, Journal of Catalysis, 141 (1993) 287-299.

[67] J.M. Lavoie, Review on dry reforming of methane, a potentially more environmentally-friendly approach to the increasing natural gas exploitation, Frontiers in Chemistry, 2 (2014) 81.

[68] V.C.H. Kroll, H.M. Swaan, C. Mirodatos, Methane reforming reaction with carbon dioxide over Ni/SiO_2 catalyst .1. Deactivation studies, Journal of Catalysis, 161 (1996) 409-422.

[69] N. Cabrera, N.F. Mott, Theory of the oxidation of metals, Reports on Progress in Physics, 12 (1949) 163.

[70] N. Kitakatsu, V. Maurice, C. Hinnen, P. Marcus, Surface hydroxylation and local structure of NiO thin films formed on Ni(111), Surface Science, 407 (1998) 36-58.

[71] D.L. Cocke, M.S. Owens, Reactivity of Metal-Oxide Overlayers - Formation of Metal Carbides, Journal of Colloid and Interface Science, 131 (1989) 166-180.

[72] P. Marécot, H. Martinez, J. Barbier, Coking reaction by anthracene on acidic aluminas and silica-aluminas, Journal of Catalysis, 138 (1992) 474-481.

[73] S. Praserthdam, P.B. Balbuena, Performance evaluation of catalysts in the dry reforming reaction of methane via the ratings concept, Reaction Kinetics, Mechanisms and Catalysis, 122 (2017) 53-68.

[74] J.J. Varghese, S.H. Mushrif, Insights into the C–H Bond Activation on NiO Surfaces: The Role of Nickel and Oxygen Vacancies and of Low Valent Dopants on the Reactivity and Energetics, The Journal of Physical Chemistry C, 121 (2017) 17969-17981.

[75] D.W. Blaylock, Y.-A. Zhu, W.H. Green, Computational Investigation of the Thermochemistry and Kinetics of Steam Methane Reforming Over a Multi-Faceted Nickel Catalyst, Topics in Catalysis, 54 (2011) 828.

APPENDIX A

REACTIVITY AND STABILITY SURFACES AT ALL OPERATING TEMPERATURES AND FEED RATIO

A1)   Reactivity and stability surfaces at all operating temperatures and feed ratio with ZPE, U, and S correction
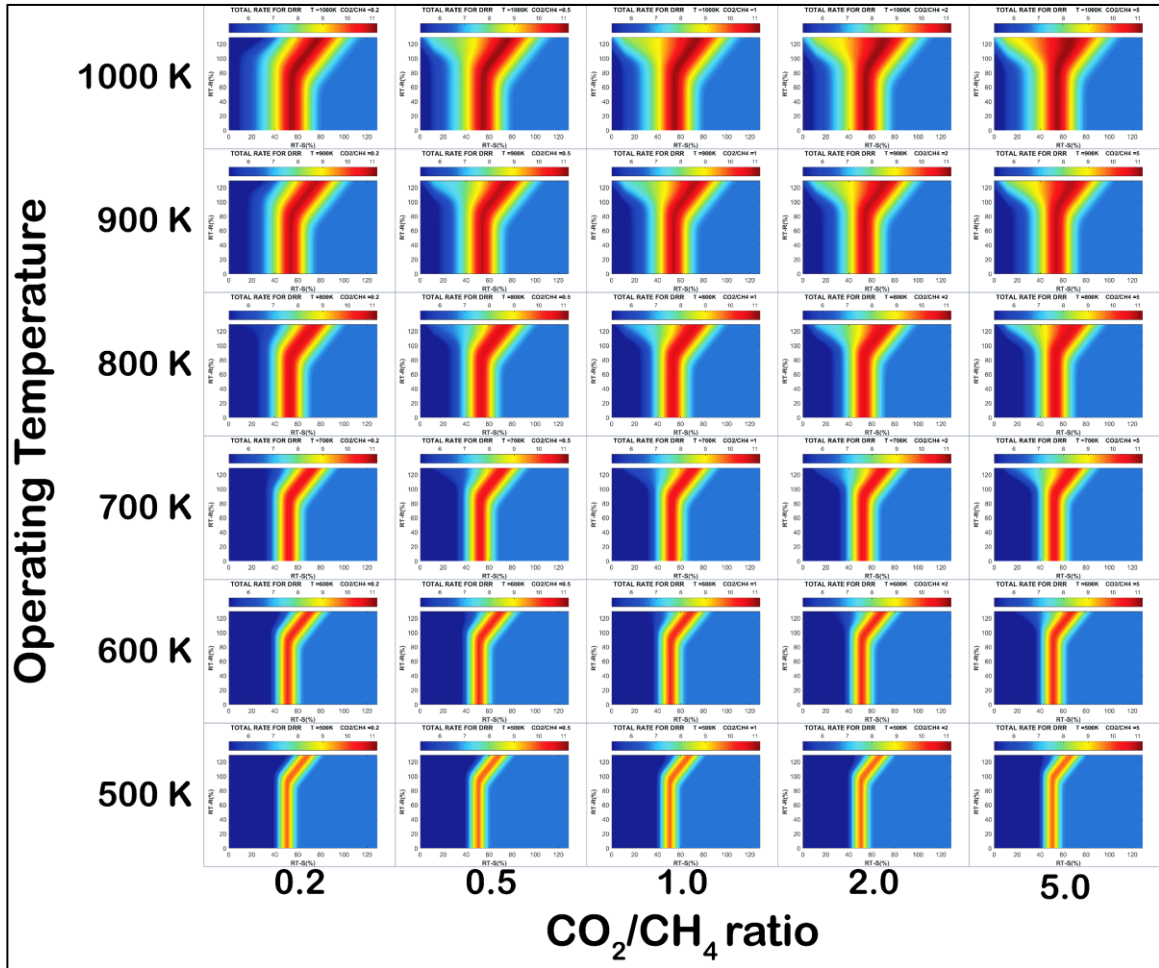

Figure A 1 Reactivity surface (RS) at all operating temperatures (500-1000 K) and CO2/CH4 feed ratios (0.2 – 5.0) with ZPE, U and S correction
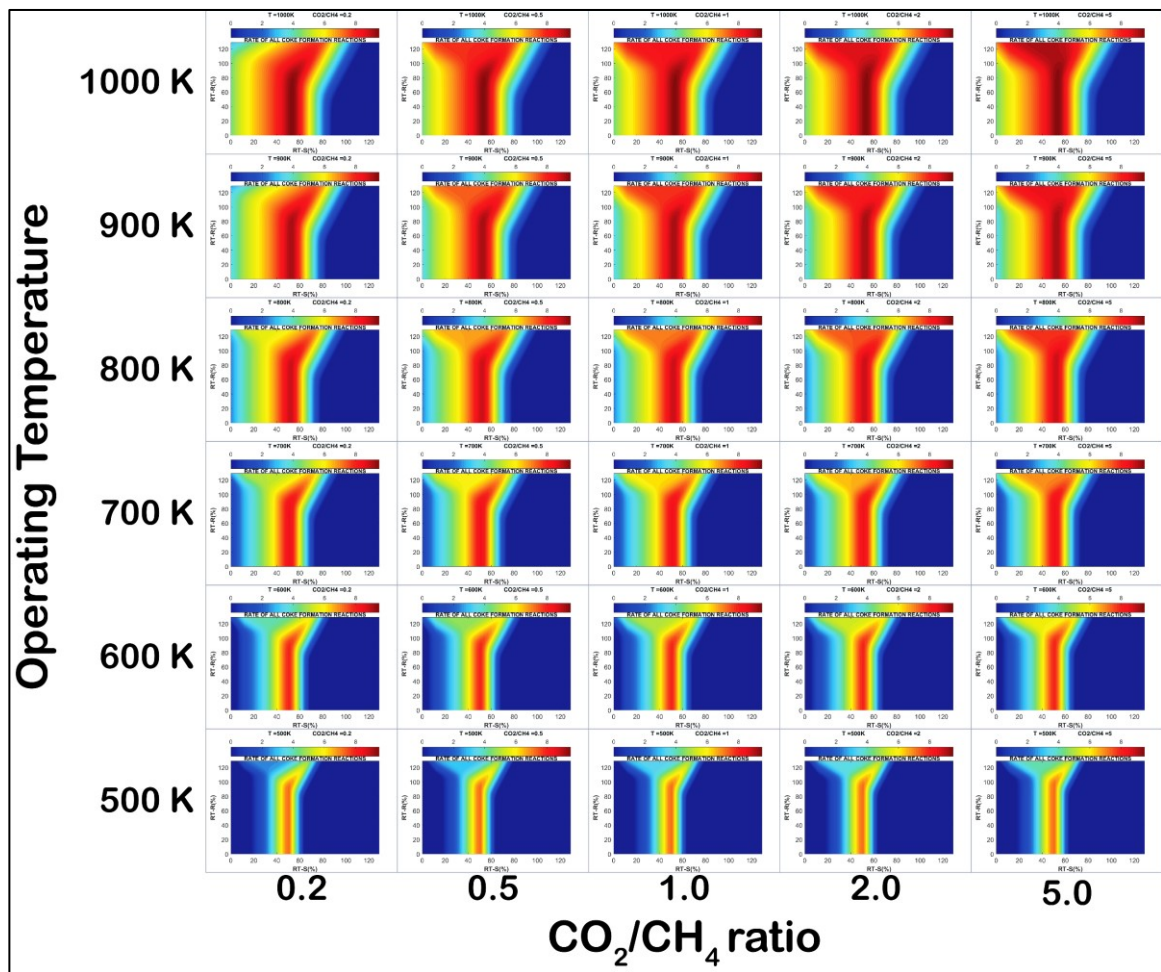
Figure A 2 Combined coke formation rate on the stability surface (SS) at all operating temperatures (500-1000 K) and CO_2/CH_4 feed ratios (0.2 – 5.0) with ZPE, U and S correction
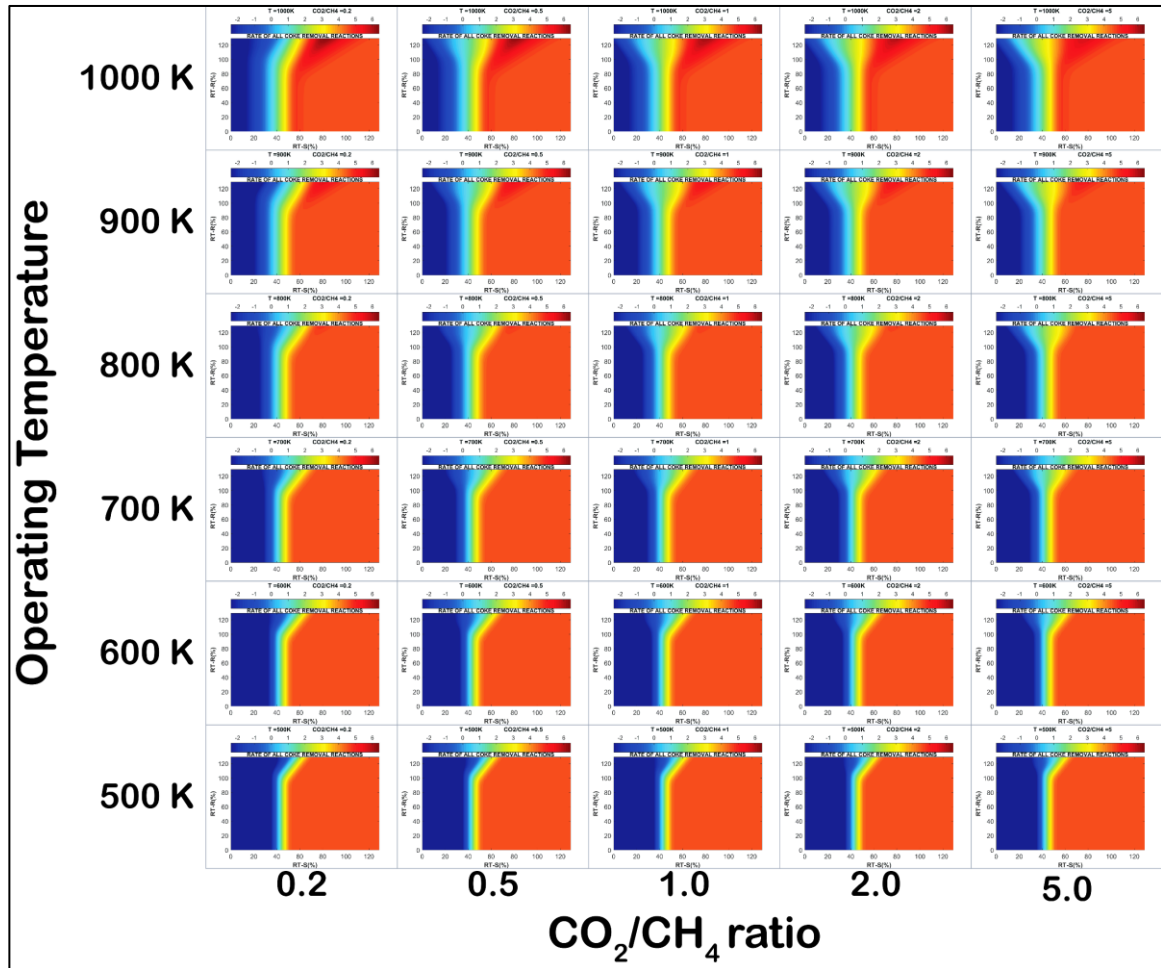
Figure A 3 Combined coke removal rate on the stability surface (SS) at all operating temperatures (500-1000 K) and CO_2/CH_4 feed ratios (0.2 – 5.0) with ZPE, U and S correction
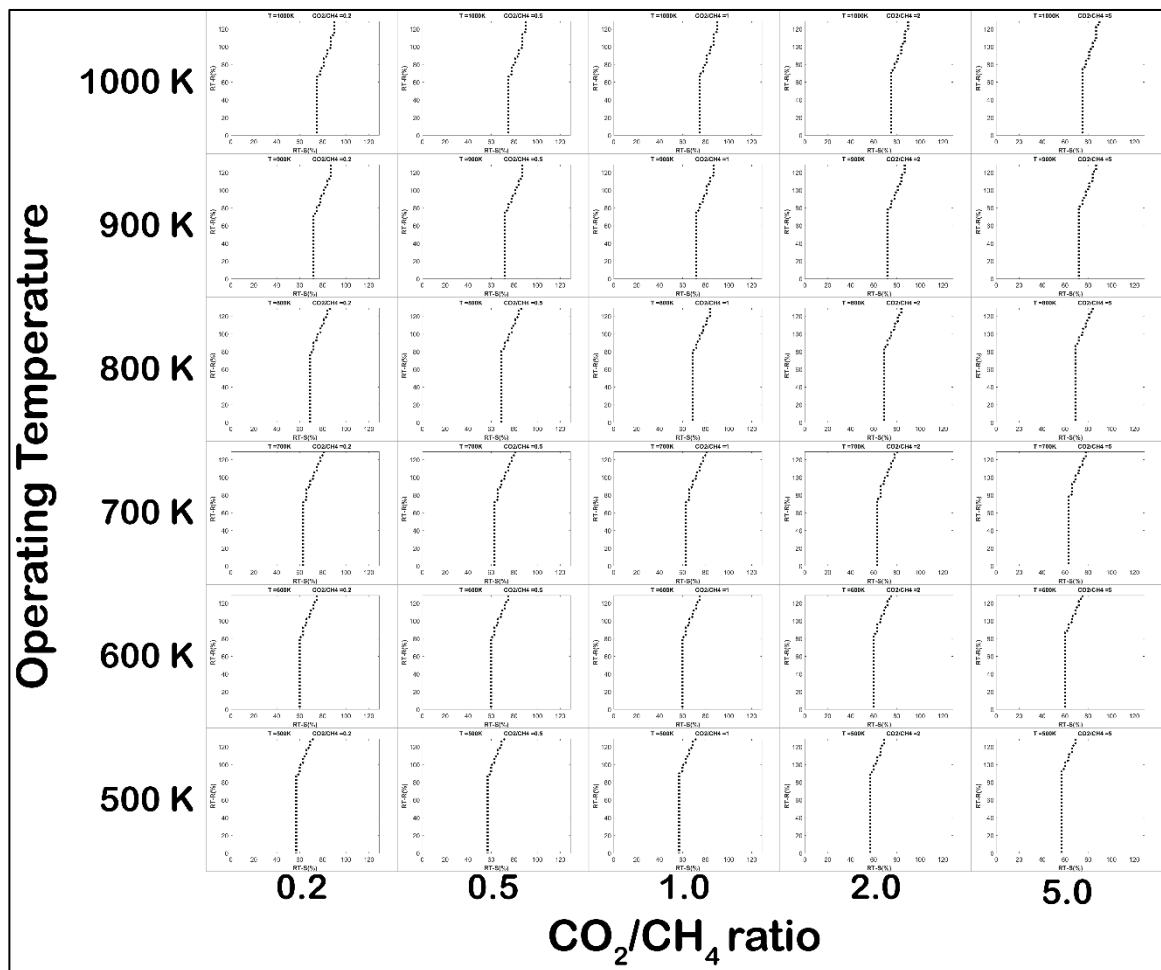
Figure A 4 Coking Boundary at all operating temperatures (500-1000 K) and CO_2/CH_4 feed ratios (0.2 – 5.0) with ZPE, U and S correction

Figure A 5 The stability surface (SS) showing individual coke formation reaction as (a) C from CH* dissociation, (b) C from CO* dissociation, (c) C from Boudouard reaction and individual coke removal reaction as (d) removal by H*, (e) removal by O* and (f) removal by reverse-Boudouard reaction with ZPE, U and S correction all at temperature = 1000 K and $CO_2/CH_4 = 0.2$

(The colors from blue to red indicate the magnitude of log rate of each specified reaction. The dotted black line separating each of the 6 figures is the coking boundary where the left side of this line is the coke formation zone, while on the right side of this line is the coke removal zone)
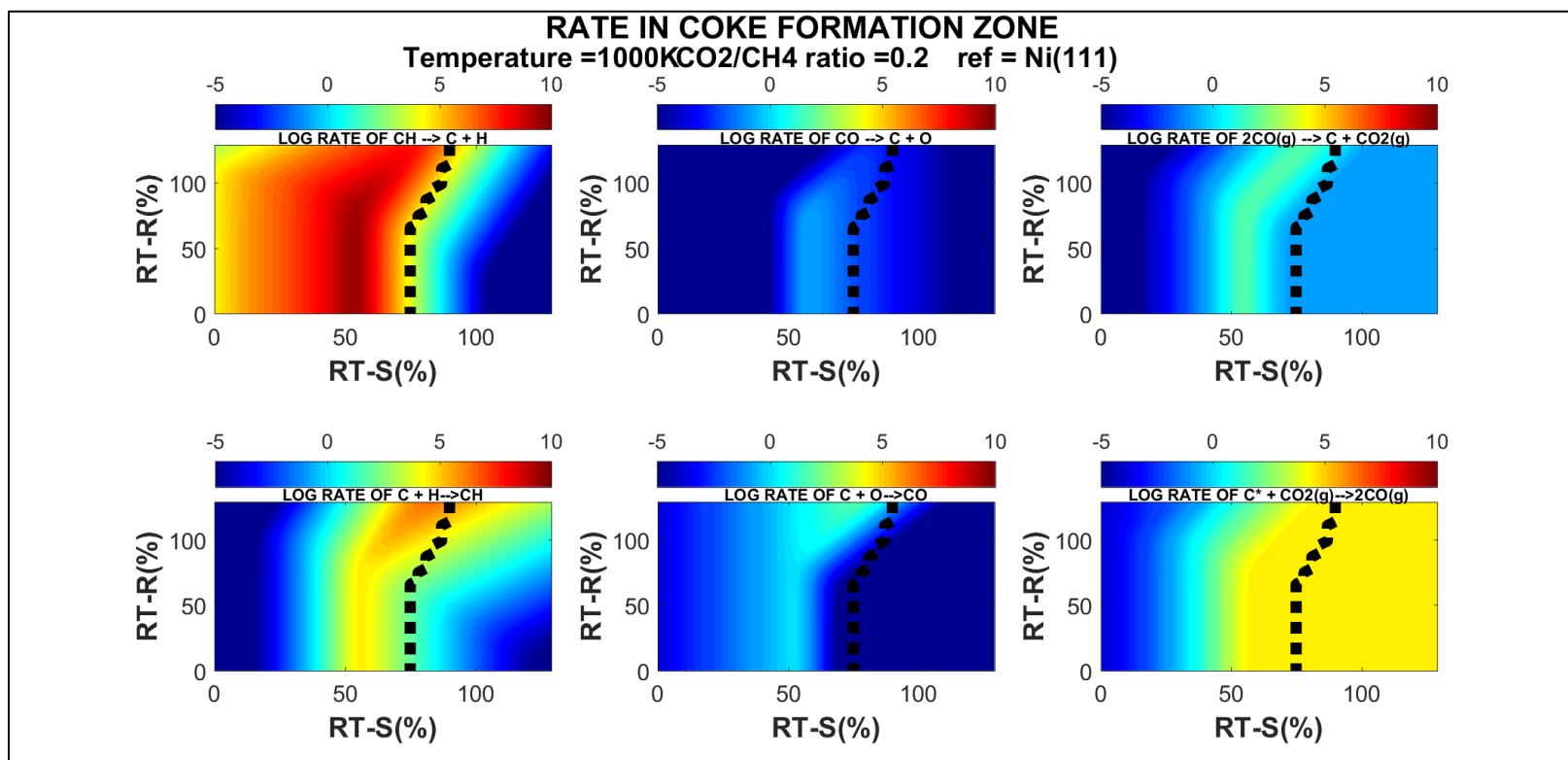
Figure A 6 The stability surface (SS) showing individual coke formation reaction as (a) C from CH* dissociation, (b) C from CO* dissociation, (c) C from Boudouard reaction and individual coke removal reaction as (d) removal by H*, (e) removal by O* and (f) removal by reverse-Boudouard reaction with ZPE, U and S correction all at temperature = 1000 K and $CO_2/CH_4 = 0.5$

(The colors from blue to red indicate the magnitude of log rate of each specified reaction. The dotted black line separating each of the 6 figures is the coking boundary where the left side of this line is the coke formation zone, while on the right side of this line is the coke removal zone)
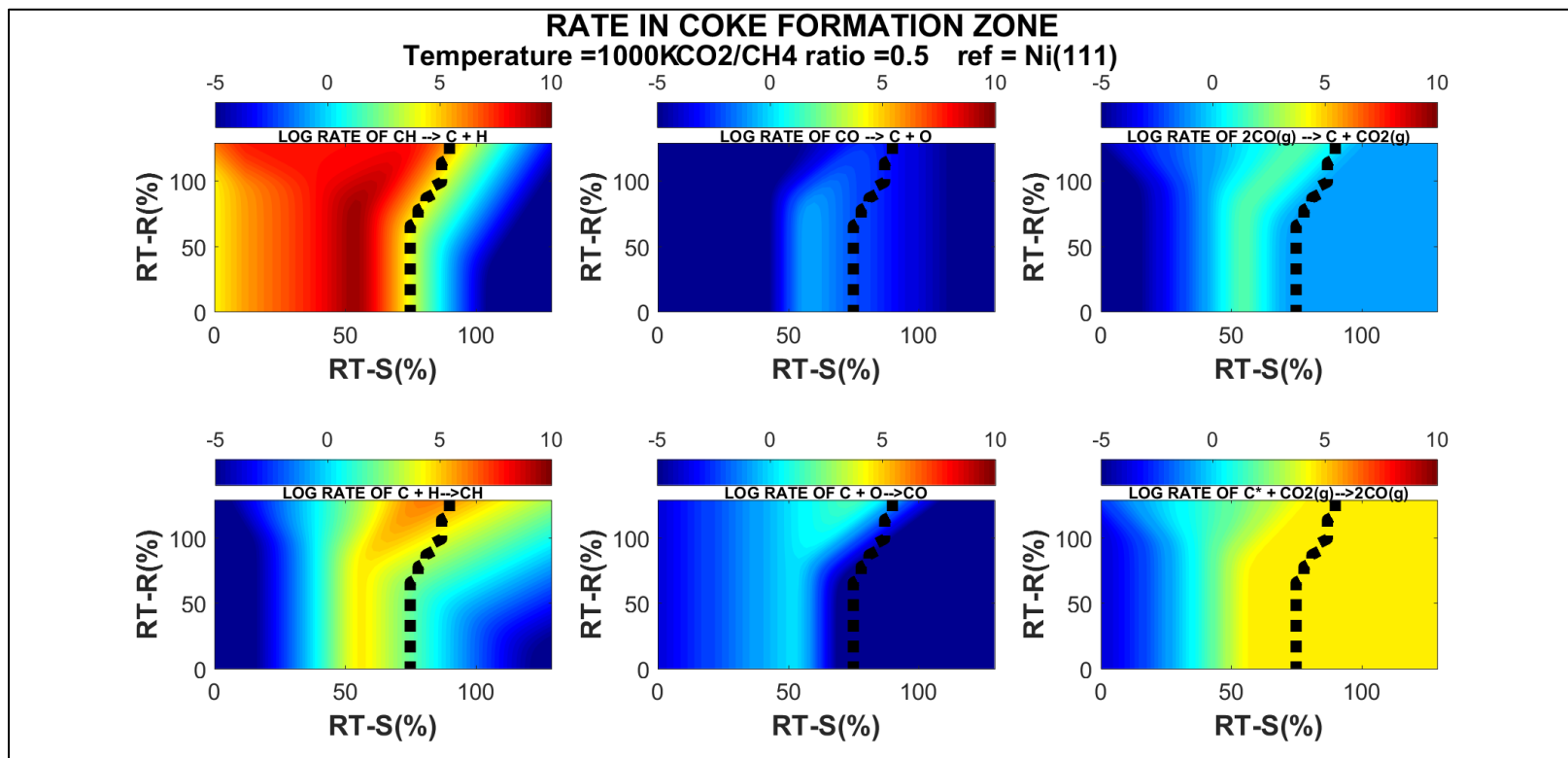
Figure A 7 The stability surface (SS) showing individual coke formation reaction as (a) C from CH* dissociation, (b) C from CO* dissociation, (c) C from Boudouard reaction and individual coke removal reaction as (d) removal by H*, (e) removal by O* and (f) removal by reverse-Boudouard reaction with ZPE, U and S correction all at temperature = 1000 K and $CO_2/CH_4 = 1$

(The colors from blue to red indicate the magnitude of log rate of each specified reaction. The dotted black line separating each of the 6 figures is the coking boundary where the left side of this line is the coke formation zone, while on the right side of this line is the coke removal zone)
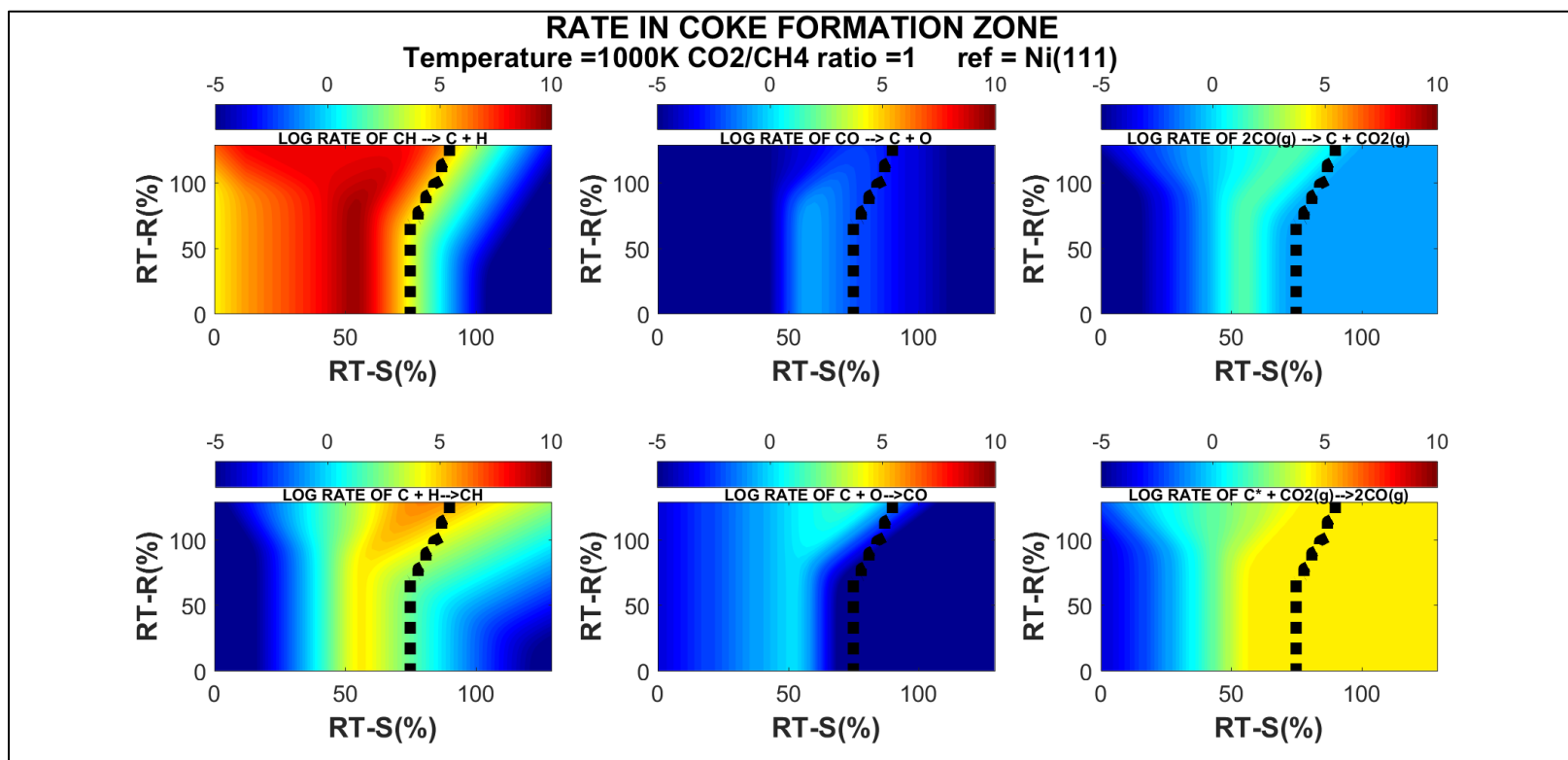
Figure A 8 The stability surface (SS) showing individual coke formation reaction as (a) C from CH* dissociation, (b) C from CO* dissociation, (c) C from Boudouard reaction and individual coke removal reaction as (d) removal by H*, (e) removal by O* and (f) removal by reverse-Boudouard reaction with ZPE, U and S correction all at temperature = 1000 K and $CO_2/CH_4 = 2$

(The colors from blue to red indicate the magnitude of log rate of each specified reaction. The dotted black line separating each of the 6 figures is the coking boundary where the left side of this line is the coke formation zone, while on the right side of this line is the coke removal zone)
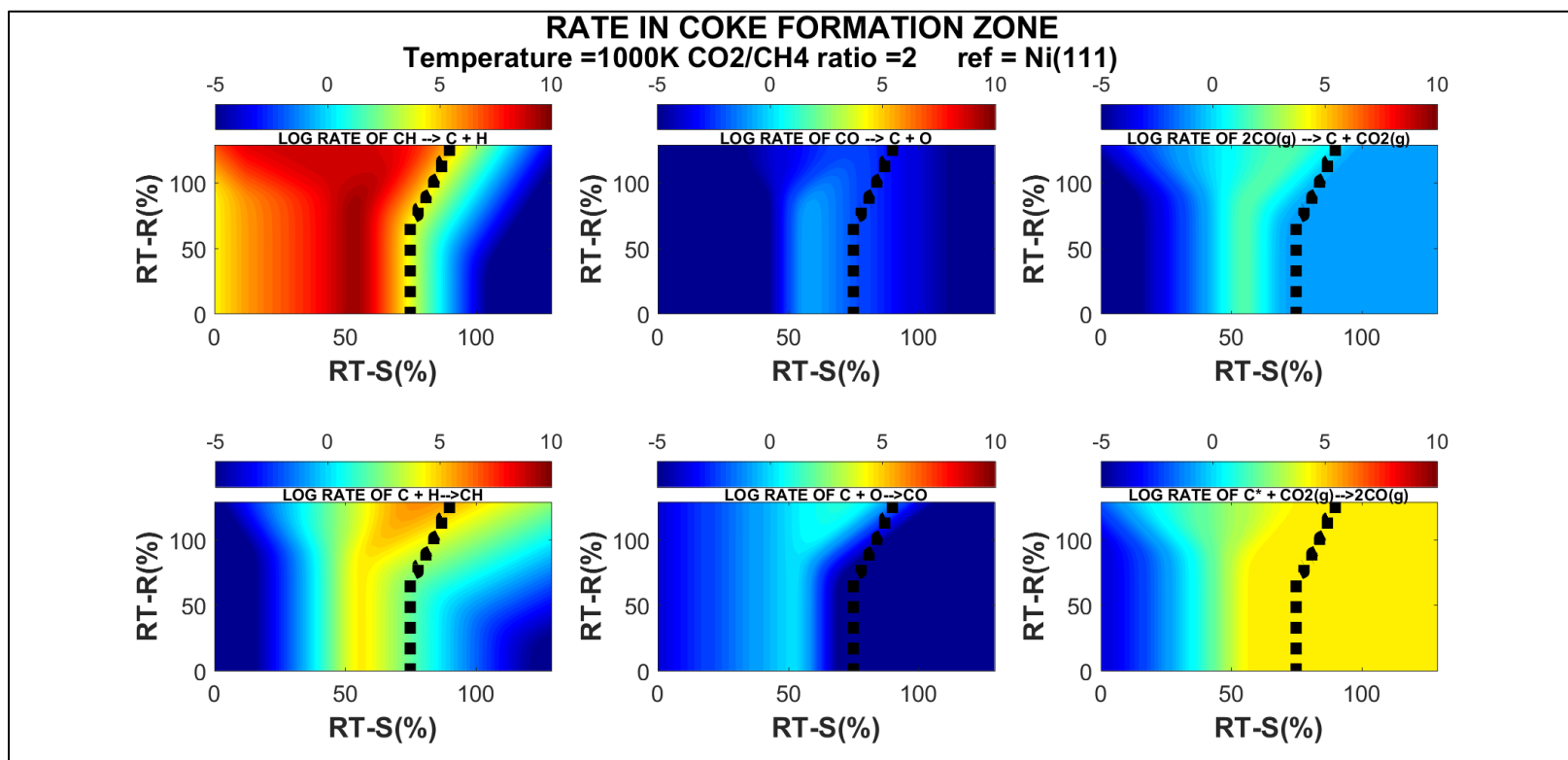
121
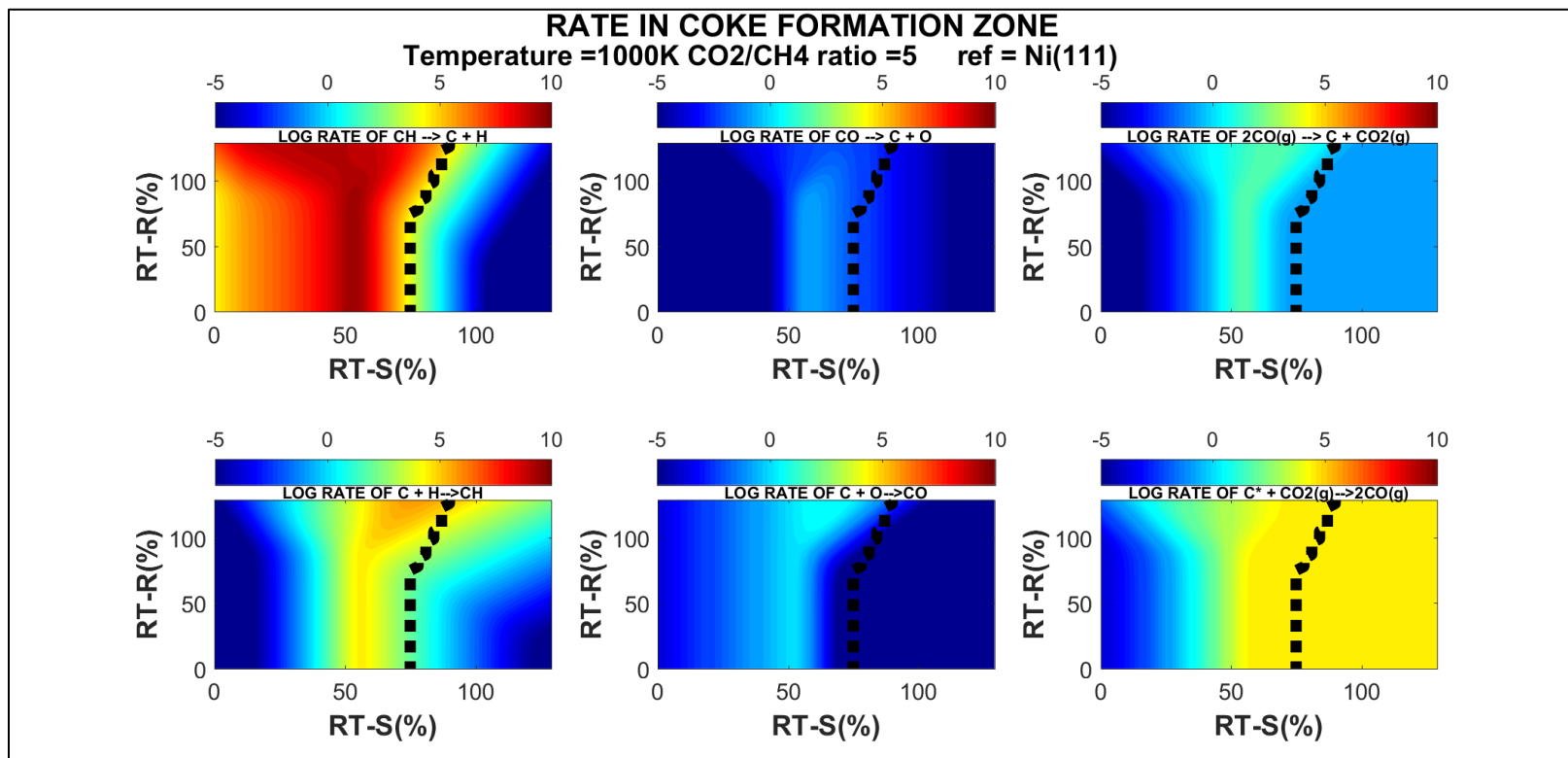
Figure A 9 The stability surface (SS) showing individual coke formation reaction as (a) C from CH* dissociation, (b) C from CO* dissociation, (c) C from Boudouard reaction and individual coke removal reaction as (d) removal by H*, (e) removal by O* and (f) removal by reverse-Boudouard reaction with ZPE, U and S correction all at temperature = 1000 K and CO_2/CH_4 = 5

(The colors from blue to red indicate the magnitude of log rate of each specified reaction. The dotted black line separating each of the 6 figures is the coking boundary where the left side of this line is the coke formation zone, while on the right side of this line is the coke removal zone)

REACTION COORDINATE, BOND LENGTH AND CONFIGURATIONS OF INITIAL
STATE (IS), TRANSITION STATE (TS) AND FINAL STATE (FS)

B1)   Reaction coordinate, bond length and configurations of the initial state (IS),
       transition state (TS) and final state (FS) for Ni(111) slab model system. (the reaction
       is designated on the plot)

Figure B 1 CH$_4$ dissociation reaction (CH$_4$ + 2* ⇄ CH$_3$* + H*) on Ni(111)

Figure B 2 H$_2$ formation reaction (2H* ⇄ H$_2$* + *) on Ni(111)
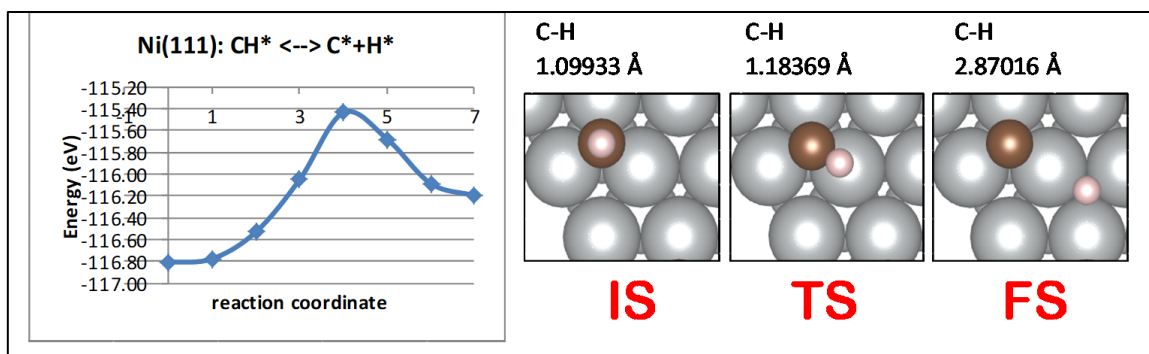
Figure B 3 CH dissociation reaction (CH + * ⇌ C* + H*) on Ni(111)
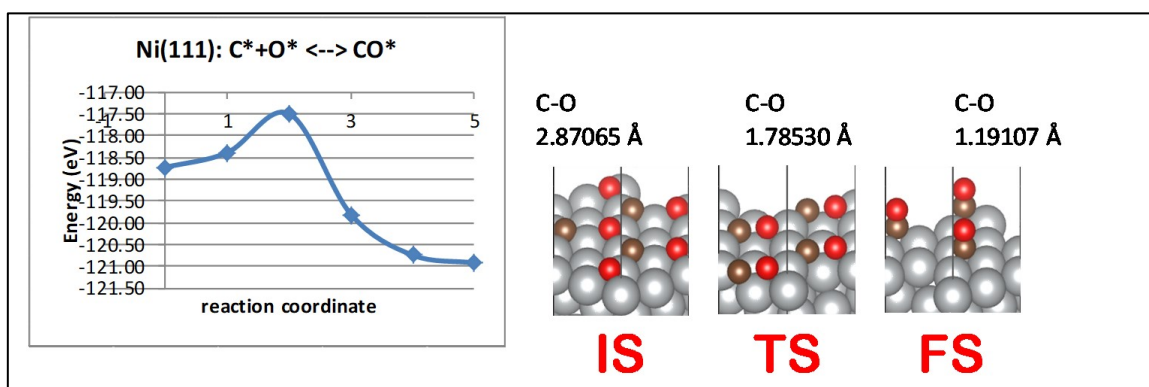
Figure B 4 CO dissociation reaction (CO + * ⇌ C* + O*) on Ni(111)

B2) Reaction coordinate, bond length and configurations of the initial state (IS), transition state (TS) and final state (FS) for Ni$_3$C(001) slab model system. (the reaction is designated on the plot)
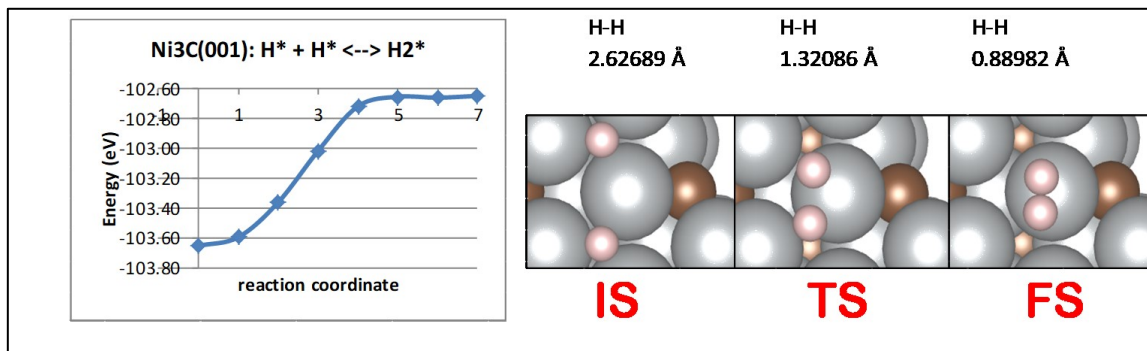
Figure B 5 H$_2$ formation reaction (2H* $\rightleftarrows$ H$_2$* + *) on Ni$_3$C(001)
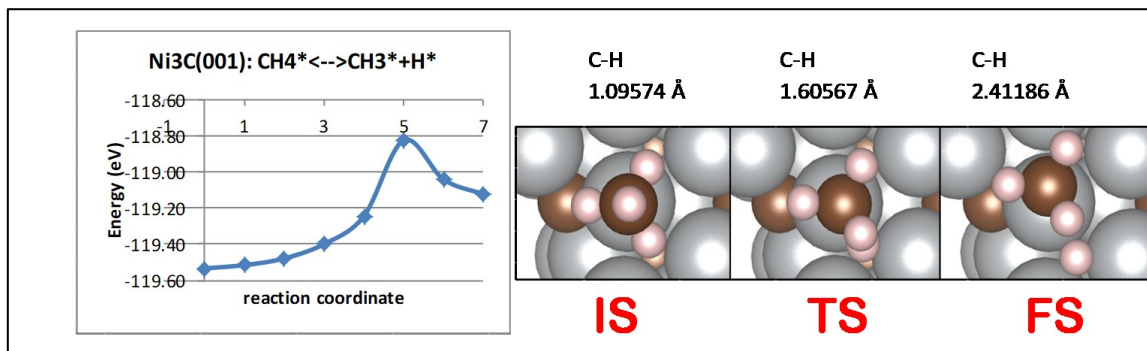
Figure B 6 CH$_4$ dissociation reaction (CH$_4$ + 2* $\rightleftarrows$ CH$_3$* + H*) on Ni$_3$C(001)

B3)   Reaction coordinate, bond length and configurations of the initial state (IS), transition state (TS) and final state (FS) for NiO(111)-p(2x2) slab model system. (the reaction is designated on the plot)
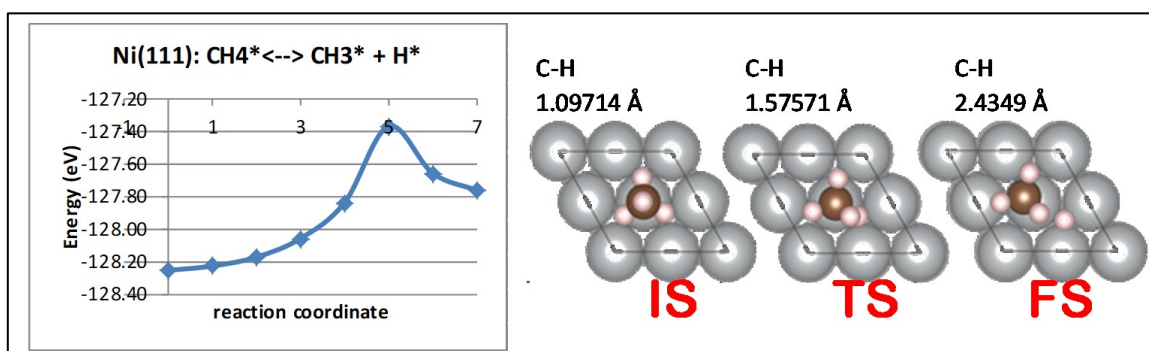

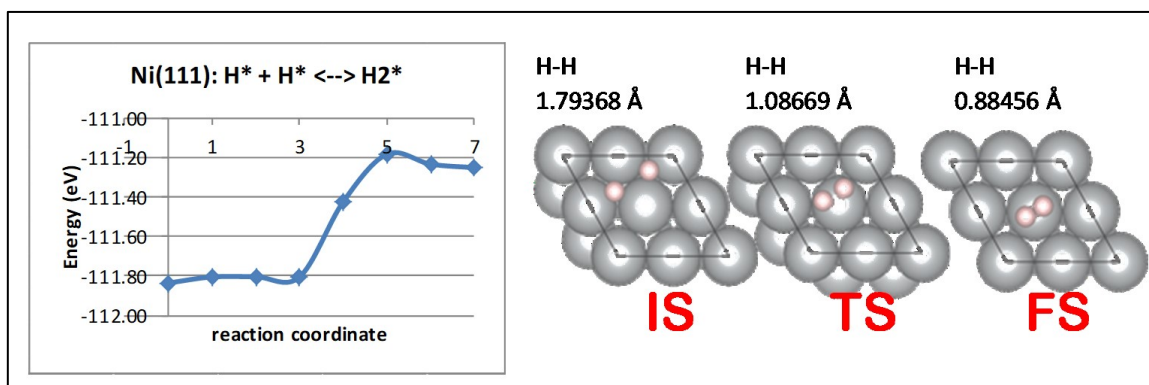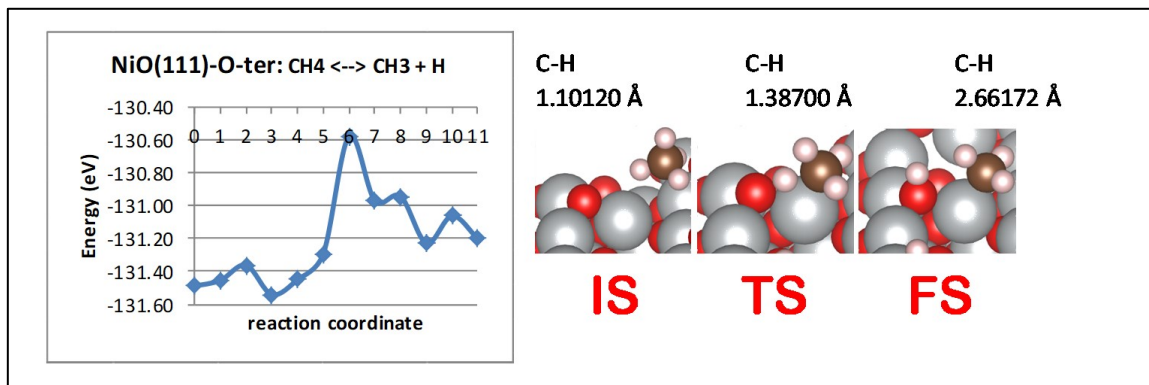Figure B 7 CH_4 dissociation reaction ($CH_4 + 2* \rightleftarrows CH_3* + H*$) on NiO(111)-$p$(2x2)
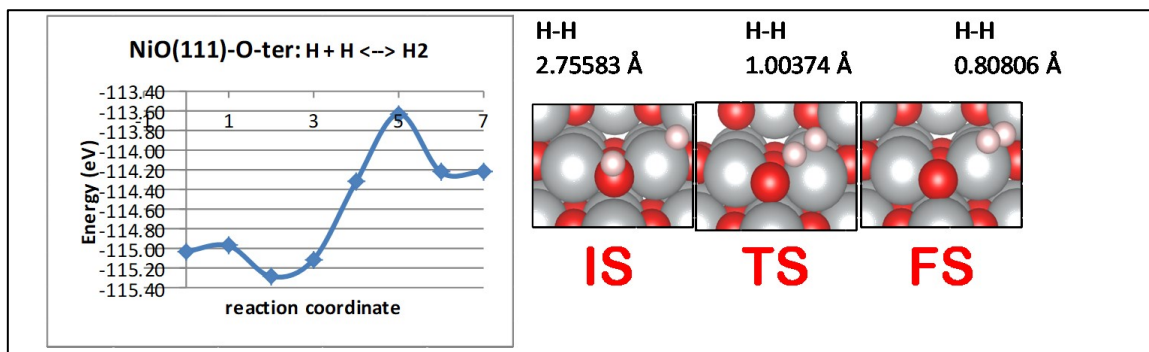
Figure B 8 H_2 formation reaction ($2H* \rightleftarrows H_2* + *$) on NiO(111)-$p$(2x2)

VALUE OF ACTIVATION ENERGY, CALCULATED STABILITY AND REACTIVITY RATINGS

Table C 1 Activation energy for each elementary step of Ni(111), Ni(100), Ni(211), Ni₃C(001) and NiO(111)-p(2x2)

set	reaction	Ni(111) E_a (eV)	Ni₃C(001) E_a (eV)	NiO(111)-p(2x2) E_a (eV)	Ni(100) E_a (eV)	Ni(211) E_a (eV)
Y	$CH_{4(g)} + 2* \rightleftarrows CH_3* + H*$	0.89	0.71	0.91	0.80	0.62
Y	$H* + H* \rightleftarrows H_{2(g)} + 2*$	0.92	1.00	1.65	0.81	0.77
X2	$CH* + * \rightleftarrows C* + H*$	1.38	1.14	1.47	0.52	0.68
X2	$CO* + * \rightleftarrows C* + O*$	3.43	2.92	*N/D	1.80	1.95
X1	$C* + H* \rightleftarrows CH* + *$	0.76	1.02	1.4	0.74	0.92
X1	$C* + O* \rightleftarrows CO* + *$	1.23	2.25	*N/D	2.16	1.74

N/D: not determined
ref: obtained from Fan et al., Ind Eng Chem Res, 54 (2015) 5901-5913.
cNEB: calculated in this paper

Table C 2 Sources of data for each elementary step of Ni(111), Ni(100), Ni(211), Ni$_3$C(001) and NiO(111)-p(2x2)

set	reaction	Ni(111) E_a (eV)	Ni$_3$C(001) E_a (eV)	NiO(111)-p(2x2) E_a (eV)	Ni(100) E_a (eV)	Ni(211) E_a (eV)
Y	$CH_{4(g)} + 2* \rightleftarrows CH_3* + H*$	cNEB	cNEB	cNEB	ref	ref
Y	$H* + H* \rightleftarrows H_{2(g)} + 2*$	ref	cNEB	cNEB	ref	ref
X2	$CH* + * \rightleftarrows C* + H*$	cNEB	ref	cNEB	ref	ref
X2	$CO* + * \rightleftarrows C* + O*$	cNEB	ref	N/D	ref	ref
X1	$C* + H* \rightleftarrows CH* + *$	cNEB	ref	cNEB	ref	ref
X1	$C* + O* \rightleftarrows CO* + *$	cNEB	ref	N/D	ref	ref
N/D: not determined						
ref: obtained from Fan et al., Ind Eng Chem Res, 54 (2015) 5901-5913.						
cNEB: calculated in this paper						

Table C 3 Stability and Reactivity ratings and their average values for each elementary step of Ni(111), Ni(100), Ni(211), Ni$_3$C(001) and NiO(111)-p(2x2)

set	reaction	Ni(111) RT (%RT)	Ni$_3$C(001) RT (%RT)	NiO(111)-p(2x2) RT (%RT)	Ni(100) RT (%RT)	Ni(211) RT (%RT)
Y	$CH_{4(g)} + 2* \rightleftarrows CH_3* + H*$	100	113	100	107	119
Y	$H* + H* \rightleftarrows H_{2(g)} + 2*$	100	94	51	107	110
X2	$CH* + * \rightleftarrows C* + H*$	100	87	110	46	57
X2	$CO* + * \rightleftarrows C* + O*$	100	99	*N/D	24	34
X1	$C* + H* \rightleftarrows CH* + *$	100	86	61	105	93
X1	$C* + O* \rightleftarrows CO* + *$	100	56	*N/D	62	90
	average RT-S	100	82	86	59	68
	average RT-R	100	104	76	114	107

VALUE OF ZERO-POINT ENERGY, ENTROPY AND INTERNAL ENERGY CORRECTIONS FOR EACH DRR
ELEMENTARY STEP

Table D 1 Zero-point energy, entropy and internal energy corrections for every DRR elementary step on Ni(111) at temperature = 1000 K and CO_2/CH_4 ratio = 1

Elementary step	reaction	E_a (eV)	ΔZPE (eV)	ΔU (eV)	$T\Delta S$ (eV)	ΔG (eV)
1	CH4(g)+2*⇄CH3*+H*	0.89	-0.04	0.20	-1.29	2.34
2	CH3*+*⇄CH2*+H*	0.70	-0.13	-0.01	-0.03	0.59
3	CH2*+*⇄CH*+H*	0.35	-0.12	-0.02	0.04	0.17
4	CH*+*⇄C*+H*	1.33	-0.17	-0.01	-0.02	1.17
5	CO2(g)+2*⇄CO*+O*	0.67	-0.04	0.17	-1.44	0.62
6	C*+O*⇄CO*+*	1.59	-0.04	-0.05	-0.09	1.59
-1	CH3*+H*⇄CH4(g)+2*	0.90	0.01	-0.05	-0.04	0.90
-2	CH2*+H*⇄CH3*+*	0.63	-0.02	-0.03	0.03	0.55
-3	CH*+H*⇄CH2*+*	0.69	-0.07	-0.02	0.12	0.48
-4	C*+H*⇄CH*+*	0.81	-0.10	-0.01	0.03	0.67
-5	CO*+O*⇄CO2(g)+2*	1.65	0.02	-0.01	-0.03	1.69
-6	CO*+*⇄C*+O*	2.94	-0.05	-0.06	-0.26	3.09

E_a = activation energy obtained directly from cNEB calculation without any ZPE, U and S corrections
ΔZPE = zero-point energy change from the initial state (IS) to the transition state (TS)
ΔU = internal energy change from the initial state (IS) to the transition state (TS)
ΔS = entropy change from the initial state (IS) to the transition state (TS)
ΔG = Gibbs free energy change from the initial state (IS) to the transition state (TS)

MODEL CONSTRUCTION OF THE INTERMEDIATE MODELS IN THE SURFACE
TRANSFORMATION NETWORK

E1)   The O/Ni models

E1.1)   Oxidation route

The construction of the model describing the oxidation of the metallic Ni is illustrated in the figure below. First of all, although, the process occurs in the direction from the left to right, the initial structure to start with is system number 5, the pure 5-layer NiO(100) slab model which is cleaved from the optimized NiO bulk.
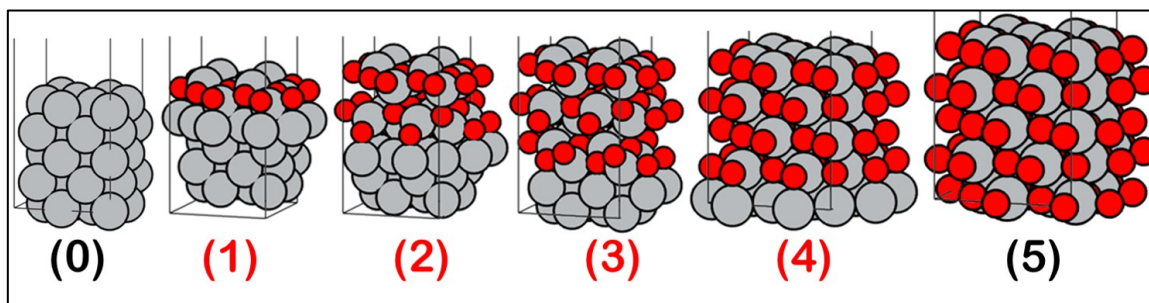
Figure E 1 Models for the oxidation route and the formula in the unit cell for each system is (0) = Ni_{40} // (1) = $Ni_{40}O_8$ // (2) = $Ni_{40}O_{16}$ // (3) = $Ni_{40}O_{24}$ // (4) = $Ni_{40}O_{32}$ // (5) = $Ni_{40}O_{40}$. (atomic color label: grey = Nickel, red = Oxygen)

After system number 5 is optimized with the setup stated in the "Method" section in the paper. As this calculation is run on VASP, the ISIF tag which designated whether the stress tensor is calculated or not, and whether any degree-of-freedom is allowed to change in the relaxation is adjusted in the following manner. Starting with the un-optimized structure, the ISIF is set to 2 calculating both the force and stress tensors, while cell shape

and volume is fixed let alone the ionic position to change. Thereafter, the ISIF is adjusted to 4 in order to let cell shape and ionic position change but still fixing the cell volume. In the final step, ISIF is set to 3 to allow cell volume to change, where at this point the system is completely relaxed confirmed by the energy decrease of the system.

Note that when the volume changes, relaxation the cutoff energy is increased in order to avoid the incorrect calculation of the stress tensor (reference: http://cms.mpi.univie.ac.at/vasp/guide/node161.html#pullay). Next for the construction of system number 5, 4, 3, 2 and 1. The oxygen atom in a system number 6 is removed from the bottom layer step-wise, while all atoms were relaxed followed by the optimization by the mentioned step using ISIF = 2 ➔ ISIF = 4 ➔ ISIF = 3.

E1.2)   Deoxygenation route

Like in the case of the oxidation route, this deoxygenation also starts from the pure 5-layer NiO(100) slab model denoted as system number 5 in the figure below.

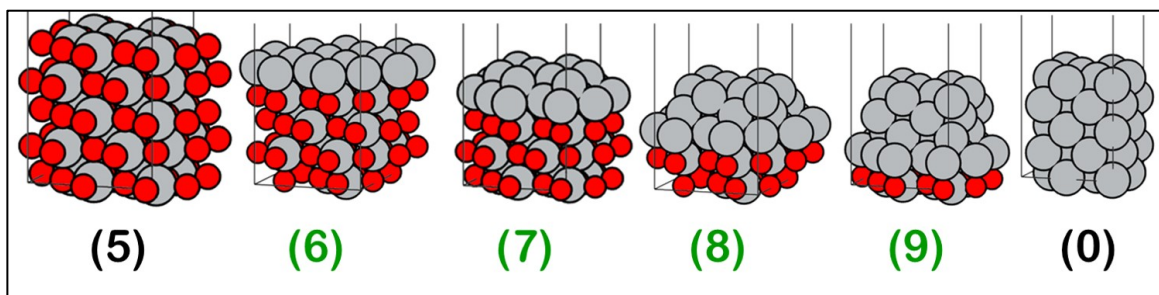Figure E 2 Models for the deoxygenation route and the formula in the unit cell for each system is (5) = $Ni_{40}O_{40}$ // (6) = $Ni_{40}O_{32}$ // (7) = $Ni_{40}O_{24}$// (8) = $Ni_{40}O_{16}$ // (9) = $Ni_{40}O_8$// (0) Ni_{40}. (atomic color label: grey = Nickel, red = Oxygen)

However, the slab models in system number 6, 7, 8 and 9 have the bottom 2 layers (Ni and O layers) fixed to the lattice parameter of the optimized NiO bulk and to imitate the situation where the prepared catalyst in the reduction step undergoes the reduction resulting in the metallic surface with the NiO core, the same step-wise removal of the oxygen but now from the top surface is carried out, where the same procedure using ISIF 2 ➔ 4 ➔ 3 is applied.

E2)   The C/Ni models

E2.1)   Carburization route

The model construction illustrating the carburization of the metallic Ni is depicted in the following figure.
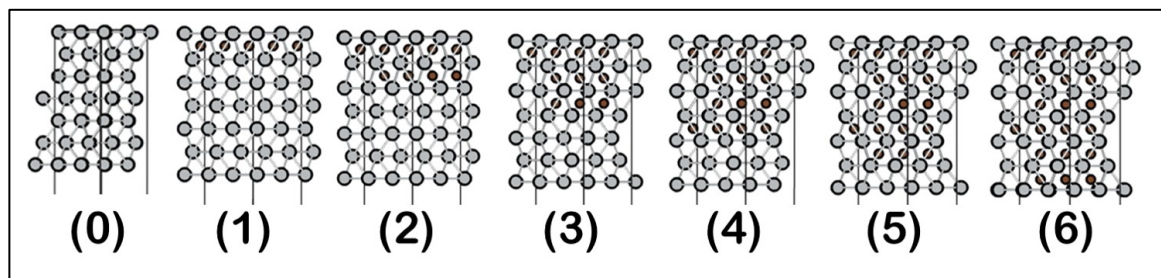
Figure E 3 Models for the carburization route and the formula in the unit cell for each system is $(0) = Ni_{84}$ // $(1) = Ni_{84}C_4$ // $(2) = Ni_{84}C_8$ // $(3) = Ni_{84}C_{12}$ // $(4) = Ni_{84}C_{16}$ // $(5) = Ni_{84}C_{20}$ // $(6) = Ni_{84}C_{24}$. (atomic color label: grey = Nickel, brown = Carbon)

The process occurs in the direction from the left to right but again the initial structure is the pure 7-layer $Ni_3C(001)$ slab model which is cleaved from the optimized Ni_3C bulk described in the "Method" section in the paper. For the construction of system number 6, 5, 4, 3, 2, 1 and 0. The carbon atom is removed step-wise from the bottom layer, while all

atoms are relaxed and followed by the optimization via the mentioned step of ISIF = 2 ➔ ISIF = 4 ➔ ISIF = 3.

E2.2) Decarburization route

Similar to the carburization route, this route starts from the pure $Ni_3C(001)$ slab model with 7 Ni-C layers. The slabs in system number 8, 9, 10, 11, 12 and 13 have the bottom 2 layers (Ni and O layers) fixed to the lattice parameter of the optimized Ni_3C bulk to imitate the coke removal process, in which the oxidizer reacts with the carbide transforming it into the metallic surface with the Ni_3C core. In addition, the step-wise removal of the carbon is carried out from the top surface down with the same procedure using ISIF 2 ➔ 4 ➔ 3.
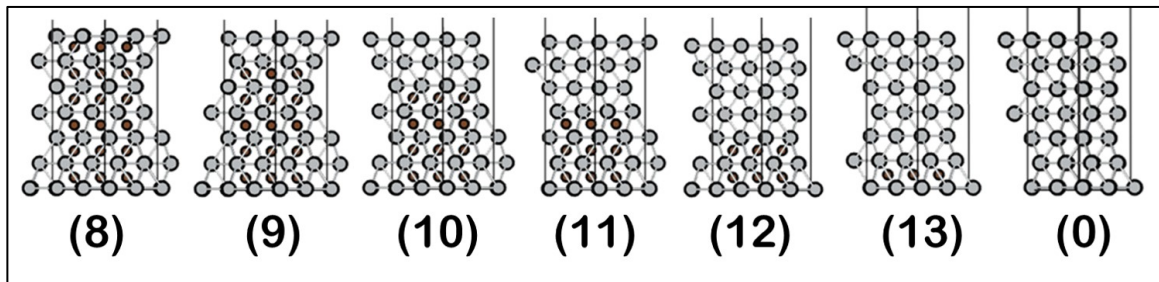

Figure E 4 Models for the decarburization route and the formula in the unit cell for each system is (8) = $Ni_{84}C_{24}$ // (9) = $Ni_{84}C_{20}$ // (10) = $Ni_{84}C_{16}$ // (11) = $Ni_{84}C_{12}$ // (12) = $Ni_{84}C_8$// (13) = $Ni_{84}C_4$// (0) = Ni_{84}. (atomic color label: grey = Nickel, brown = Carbon)

MATLAB CODE FOR MICROKINETIC CALCULATIONS

F1)   Matlab code for the calculation of surface coverage of all species at all (RT-S, RT-R) indexes

Declare parameters

```
syms th th_CH3 th_CH2 th_CH th_CO th_O th_C th_H
syms k1 k2 k3 k4 k5 k6 k7 k8 k9 k10 k11
syms k_1 k_2 k_3 k_4 k_5 k_6 k_7 k_8
syms P_CH4 P_CO2 P_H2 P_CO P0 yCH4 yCO2
```

Specify operating temperature and CO_2/CH_4 ratio

```
T = 1000; % K
CMratio = 1;
```

Specify values of constants

```
kB = 8.617e-5; %eV/K
h = 4.135e-15; %eV*s
```

Calculation of each species pressure

```
PCH4CO2 = 2; PCOH2 = 0.2; Ptot = PCH4CO2+PCOH2;
P_CH4 = PCH4CO2/(CMratio+1); P_CO2 = P_CH4*CMratio; P_H2 = 0.1;  P_CO = 0.1;
P0 = P_CH4+P_CO2+P_H2+P_CO;
yCH4 = (P_CH4/P0); yCO2 = (P_CO2/P0); yH2 = (P_H2/P0); yCO = (P_CO/P0);
```

Specify all elementary E_a for reference catalyst

```
%all Ea and ki (Ea ref = Ni(111), Fan et al(2014))
Ea_f0 = [0.91, 0.70, 0.35, 1.33, 0.67, 1.59];
Ea_r0 = [0.90, 0.63, 0.69, 0.81, 1.65, 2.94];
refcat = 'ref = Ni(111)';
```

Specify the range of RT-S and RT-R on the RS and SS
(in this case from ratings of 0-120 %RT)

```
RT = (0:3:120);
```

Pre-specify the zeros matrix for each E_a for faster iteration

Eax = zeros(size(RT,2));

Ea1 = Eax; Ea5 = Eax; Ea_4 = Eax; Ea_6 = Eax;

nk1 = Eax; nk5 = Eax; nk_4 = Eax; nk_6 = Eax;

Ea4 = Eax; Ea6 = Eax; nk4 = Eax; nk6 = Eax;

Ansth = Eax; Ansth_CH3 = Eax; Ansth_CH2 = Eax; Ansth_CH = Eax;

Ansth_O = Eax; Ansth_C = Eax; Eax; Ansth_H = Eax; Ansth_CO = Eax;

rCH4 = Eax; rCO2 = Eax; CHECK = Eax;

Ansr1 = Eax;Ansr2 = Eax;Ansr3 = Eax;Ansr4 = Eax;Ansr5 = Eax;Ansr6 = Eax;

Specify the ratings scale ratio (unit of eV/%RT)

phivalue = 0.015; %eV/%RT

Specify the default value of the reference catalyst, Ni(111)

% from TST: k(i) = (kB*T/h)*exp(-(EaX(i)-dSX(i)*T)/kB/T)

k1 = 1.01e-2; %k1 = nk1(m);

k2 = 1.83e10; %k2 = nk(2);

k3 = 1.31e12; %k3 = nk(3);

k4 = 3.18e7; %k4 = nk4(i);

k5 = 1.82e8; %k5 = nk5(m);

k6 = 4.91e5; %k6 = nk6(i);

k7 = 7.16e7;

k8 = 1.03e6;

k_1 = 1.42e10; %k_1 = nk_(1);

k_2 = 2.16e10; %k_2 = nk_(2);

k_3 = 2.81e10; %k_3 = nk_(3);

k_4 = 6.72e9; %k_4 = nk_4(i);

k_5 = 5.47e5; %k_5 = nk_(5);

k_6 = 3.69e-3; %k_6 = nk_6(i);

k_7 = 2.7e1;

k_8 = 4.89;

Add the ZPE, thermal (U) and entropy (S) correction to the E_a

% This is the correction for the Ea by adding ZPE, U and S in eV

% now we have real G for the calculation of the ki

corf = [1.45,-0.11,-0.18,-0.16,1.57,0,0,0]; % correction for forward reaction

corr = [0,-0.08,-0.21,-0.14,0.04,0.15,0,0]; % correction for reverse reaction

Calculation of the new E_a at each (RT-S, RT-R) on the plot

for i=1:size(RT,2) %Ea change for step 1 4 -4 5 6 -6

%RT-S : 4 6   %RT-R : 1 -4 5 -6

phi = -phivalue; %reverse relation for Ea 1, -4, 5, 6

Ea1(i) = Ea_f0(1)+(phi*(RT(i)-100));

Ea_4(i) = Ea_r0(4)+(phi*(RT(i)-100));

Ea5(i) = Ea_f0(5)+(phi*(RT(i)-100));

Ea6(i) = Ea_f0(6)+(phi*(RT(i)-100));

phi = phivalue; %direct relation for Ea 4, -6

Ea_6(i) = Ea_r0(6)+(phi*(RT(i)-100));

Ea4(i) = Ea_f0(4)+(phi*(RT(i)-100));

Check if the calculate value of E_a at the location is less than zero, if so, set it to zero.

(since E_a must remain positive)

if Ea1(i)<0

   Ea1(i) = 0;

end

if Ea_4(i)<0

   Ea_4(i) = 0;

end

if Ea5(i)<0

   Ea5(i) = 0;

end

if Ea_6(i)<0

   Ea_6(i) = 0;

end

if Ea4(i)<0

```matlab
    Ea4(i) = 0;
end
if Ea6(i)<0
    Ea6(i) = 0;
end
```

Calculation of rate constant (k_i)

```matlab
% with ZPE/U/S correction
nk1(i) = kB*T/h*exp(-(Ea1(i)+corf(1))/kB/T);
nk_4(i) = kB*T/h*exp(-(Ea_4(i)+corr(4))/kB/T);
nk5(i) = kB*T/h*exp(-(Ea5(i)+corf(5))/kB/T);
nk6(i) = kB*T/h*exp(-(Ea6(i)+corf(6))/kB/T);
nk_6(i) = kB*T/h*exp(-(Ea_6(i)+corr(6))/kB/T);
nk4(i) = kB*T/h*exp(-(Ea4(i)+corf(4))/kB/T);
end

N = size(Ea_f0, 2);
Ea = zeros(1,N); nk = zeros(1,N); Ea_ = zeros(1,N); nk_ = zeros(1,N);
for i = 1:N %constant Ea -1 2 -2 3 -3 -5 (use Ea(i))
if i ~= 1&&i ~= 4&&i ~= 5&&i ~= 6
Ea(i) = Ea_f0(i);
nk(i) = kB*T/h*exp(-(Ea(i)+corf(i))/kB/T);
end
if i ~= 4&&i ~= 6
Ea_(i) = Ea_r0(i);
nk_(i)= kB*T/h*exp(-(Ea_(i)+corr(i))/kB/T);
end
end
```

Start solving for all surface coverage (θ_i)

```matlab
for m=1:size(RT,2) % this is RT-R loop
for i=1:size(RT,2) % this is RT-S loop (x change)
% i for RT-S = 4 6 -4 -6 % m for RT-R = 1 5
```

```
clearvars th th_CH3 th_CH2 th_CH th_CO th_O th_C th_H;
syms th th_CH3 th_CH2 th_CH th_CO th_O th_C th_H
%constant Ea -1 2 -2 3 -3 -5 7 8 -7 -8
k1 = nk1(m);
k2 = nk(2);
k3 = nk(3);
k4 = nk4(i);
k5 = nk5(m);
k6 = nk6(i);
k_1 = nk_(1);
k_2 = nk_(2);
k_3 = nk_(3);
k_4 = nk_4(i);
k_5 = nk_(5);
k_6 = nk_6(i);
K7 = k7/k_7; K8 = k8/k_8;
th_H = th*(yH2/K7)^0.5;
th_CO = th*(yCO/K8);


r1 = (k1*yCH4*th*th)-(k_1*th_CH3*th_H);
r2 = (k2*th_CH3*th)-(k_2*th_CH2*th_H);
r3 = (k3*th_CH2*th)-(k_3*th_CH*th_H);
r4 = (k4*th_CH*th)-(k_4*th_C*th_H);
r5 = (k5*yCO2*th*th)-(k_5*th_CO*th_O);
r6 = (k6*th_C*th_O)-(k_6*th_CO*th);
 eq1 = r1-r2 ==0; %CH3
eq2 = r2-r3 ==0; %CH2
eq3 = r3-r4 ==0; %CH
eq4 = r4-r6 ==0; %C
eq5 = r5-r6 ==0; %O
```

```matlab
 %solve eq1 to get CH3 = f(CH2)
eqCH3 = solve(eq1, th_CH3);
%sub CH3 = f(CH2) into eq2
eq2 = subs(eq2, th_CH3, eqCH3);
%solve eq1 to get CH2 = f(CH)
eqCH2 = solve(eq2, th_CH2);
% solve eq5 for O = f(C)
eqO = solve(eq5, th_O);
% get eqZ = eq4-eq5 = f(CH, C, O)
eqZ = eq4-eq5;
% sub th_CH2
eq3 = subs(eq3, th_CH2, eqCH2);
% solve eq3 for CH = f(C)
eqCH = solve(eq3, th_CH);
% subs eqZ to be f(C) only
% sub th_CH and th_O
eqZ = subs(eqZ, { th_CH , th_O }, { eqCH , eqO });
% solve for th_C
th_C = solve(eqZ, th_C);
%For Matlab ver. 2012-4 % Positive answer is picked first
th_C = th_C(1);
version = 'Matlab 2012-14';
%For Matlab ver. 2016 % Positive answer is picked second
%th_C = th_C(2);
%version = 'Matlab 2016';
%sub back and find all coverage
% CH = f(C)
th_CH = subs(th_CH, th_C);
% CH2 = f(CH) = f(C)
th_CH2 = subs(th_CH2, th_CH);
% O = f(C)
```

```
th_O = subs(th_O, th_C);
% CH3 = f(CH2) = f(CH) = f(C)
th_CH3 = subs(th_CH3, th_CH2);
% carry out total site balance sum(th,i) = 1 %don't change
eqth = 1 - th_CH3 - th_CH2 - th_CH - th_C - th_H - th_O - th_CO-th;
% solve th from the total site balance
solveth = solve(eqth, th);
%In this calculation, ANS = f(RT-R, RT-S)
% pick only positive th
Ansth(i,m) = solveth(1);
%solve for each coverage
Ansth_CH(i,m) = double(subs(th_CH, Ansth(i,m)));
Ansth_CH2(i,m) = double(subs(th_CH2, Ansth(i,m)));
Ansth_CH3(i,m) = double(subs(th_CH3, Ansth(i,m)));
Ansth_C(i,m) = double(subs(th_C, Ansth(i,m)));
Ansth_H(i,m) = double(subs(th_H, Ansth(i,m)));
Ansth_CO(i,m) = double(subs(th_CO, Ansth(i,m)));
Ansth_O(i,m) = double(subs(th_C, Ansth(i,m)));
end %end of RT-S loop
end %end of RT-R loop
```

F2)   Matlab code for the calculation of each reaction rate at all (RT-S, RT-R) indexes

To get the rate = f(RT-S, RT-R)

for m=1:size(RT,2) % this is RT-R loop

for i=1:size(RT,2) % this is RT-S loop (x change)

[m,i];

k1 = nk1(m);

k4 = nk4(i);

k5 = nk5(m);

k6 = nk6(i);

k_4 = nk_4(i);

k_6 = nk_6(i);

Get rate of all elementary steps

Ansr1(m,i) = (k1*yCH4*Ansth(i,m)*Ansth(i,m))-(k_1*Ansth_CH3(i,m)*Ansth_H(i,m));

Ansr2(m,i) = (k2*Ansth_CH3(i,m)*Ansth(i,m))-(k_2*Ansth_CH2(i,m)*Ansth_H(i,m));

Ansr3(m,i) = (k3*Ansth_CH2(i,m)*Ansth(i,m))-(k_3*Ansth_CH(i,m)*Ansth_H(i,m));

Ansr4(m,i) = (k4*Ansth_CH(i,m)*Ansth(i,m))-(k_4*Ansth_C(i,m)*Ansth_H(i,m));

Ansr5(m,i) = (k5*yCO2*Ansth(i,m)^2)-(k_5*Ansth_CO(i,m)*Ansth_O(i,m));

Ansr6(m,i) = (k6*Ansth_C(i,m)*Ansth_O(i,m))-(k_6*Ansth_CO(i,m)*Ansth(i,m));

Ansr7(m,i) = (k7*Ansth_H(i,m)*Ansth_H(i,m))-(k_7*yH2*Ansth(i,m)^2);

Ansr8(m,i) = (k8*Ansth_CO(i,m))-(k_8*yCO*Ansth(i,m));

Get rate of all forward elementary steps

% rate of Boudouard reaction (rBD) and reverse boudouard (RBD)

% BD = 2*r-8 + r-6 + r-5

rBDrev(m,i) = -(2*Ansr8(m,i)+Ansr6(m,i)+Ansr5(m,i));

rRBDrev(m,i) = -rBDrev(m,i);

Ansr1F(m,i) = (k1*yCH4*Ansth(i,m)*Ansth(i,m));

Ansr2F(m,i) = (k2*Ansth_CH3(i,m)*Ansth(i,m));

Ansr3F(m,i) = (k3*Ansth_CH2(i,m)*Ansth(i,m));

Ansr4F(m,i) = (k4*Ansth_CH(i,m)*Ansth(i,m));

Ansr5F(m,i) = (k5*yCO2*Ansth(i,m)^2);

Ansr6F(m,i) = (k6*Ansth_C(i,m)*Ansth_O(i,m));

Ansr7F(m,i) = (k7*Ansth_H(i,m)*Ansth_H(i,m));

Ansr8F(m,i) = (k8*Ansth_CO(i,m));

Get rate of all reverse elementary steps

Ansr1R(m,i) = Ansr1F(m,i)-Ansr1(m,i);

Ansr2R(m,i) = Ansr2F(m,i)-Ansr2(m,i);

Ansr3R(m,i) = Ansr3F(m,i)-Ansr3(m,i);

Ansr4R(m,i) = Ansr4F(m,i)-Ansr4(m,i);

Ansr5R(m,i) = Ansr5F(m,i)-Ansr5(m,i);

Ansr6R(m,i) = Ansr6F(m,i)-Ansr6(m,i);

Ansr7R(m,i) = Ansr7F(m,i)-Ansr7(m,i);

Ansr8R(m,i) = Ansr8F(m,i)-Ansr8(m,i);

Get Log rate of all forward elementary steps

LOG10r1F(m,i) = log10(Ansr1F(m,i));

LOG10r2F(m,i) = log10(Ansr2F(m,i));

LOG10r3F(m,i) = log10(Ansr3F(m,i));

LOG10r4F(m,i) = log10(Ansr4F(m,i));

LOG10r5F(m,i) = log10(Ansr5F(m,i));

LOG10r6F(m,i) = log10(Ansr6F(m,i));

LOG10r7F(m,i) = log10(Ansr7F(m,i));

LOG10r8F(m,i) = log10(Ansr8F(m,i));

Get Log rate of all reverse elementary steps

LOG10r1R(m,i) = log10(Ansr1R(m,i));

LOG10r2R(m,i) = log10(Ansr2R(m,i));

LOG10r3R(m,i) = log10(Ansr3R(m,i));

LOG10r4R(m,i) = log10(Ansr4R(m,i));

LOG10r5R(m,i) = log10(Ansr5R(m,i));

LOG10r6R(m,i) = log10(Ansr6R(m,i));

LOG10r7R(m,i) = log10(Ansr7R(m,i));

LOG10r8R(m,i) = log10(Ansr8R(m,i));

Get rate for DRR with Boudouard and reverse-Boudouard reactions

%corrected rDRR with shared rate with Boudourd and reverse-Boudouard rxn

%DRR = r1+r2+r3+r4+ 0.5*r5 + 0.5*r6 + 2*r7 + 0.5*(2*r8)

rDRR(m,i) = Ansr1(m,i) + Ansr2(m,i) + Ansr3(m,i) + Ansr4(m,i) + (0.5)*Ansr5(m,i) + (0.5)*Ansr6(m,i) + 2*Ansr7(m,i) + 2*(0.5)*Ansr8(m,i);

Get rate of CH$_4$ decomposition in the case of Pt and Rh supported catalysts

rCH4(m,i) = double(k1*yCH4*Ansth(i,m)^2);

Get rate for each coke formation and removal reaction

% BD = 0.5*(2*r8R) + (0.5)*r6R + (0.5)*r5R

% RBD = 0.5*(2*r8F) + (0.5)*r6F + (0.5)*r5F

rCgenCH(m,i) = (k4*Ansth_CH(i,m)*Ansth(i,m));

rCgenCO(m,i) = (k_6*Ansth_CO(i,m)*Ansth(i,m));

rBD(m,i) = 0.5*2*Ansr8R(m,i)+0.5*Ansr6R(m,i)+0.5*Ansr5R(m,i);

rCremH(m,i) = (k_4*Ansth_C(i,m)*Ansth_H(i,m));

rCremO(m,i) = (k6*Ansth_C(i,m)*Ansth_O(i,m));

rRBD(m,i) = 0.5*2*Ansr8F(m,i)+0.5*Ansr6F(m,i)+0.5*Ansr5F(m,i);

Get total coke formation rate

%%%%%%%%%% total coke formation

rCgen(m,i) = ((k4*Ansth_CH(i,m)*Ansth(i,m))+(k_6*Ansth_CO(i,m)*Ansth(i,m)));

rCgenrev(m,i) = Ansr4(m,i)+(-Ansr6(m,i));

rCgenBD(m,i) = rCgen(m,i)+rBD(m,i);

Get total coke removal rate

%%%%%%%%%% total coke removal

rCrem(m,i) = (k_4*Ansth_C(i,m)*Ansth_H(i,m))+(k6*Ansth_C(i,m)*Ansth_O(i,m));

rCremBD(m,i) = rCrem(m,i)+rRBD(m,i);

Generate coking zone

rCtotBD(m,i) = rCremBD(m,i)-rCgenBD(m,i); %this is to make coking zone

Eliminate negative rates and calculate the log rate

% this is to eliminate negative rate. When in log plot, the rate at any location with negative rate is assigned to -100 to avoid plotting of that location

```
if rCH4(m,i)>0
        LOG10rCH4(m,i) = log10(rCH4(m,i));
        LOG10_rCH4(m,i) = -100;
end
if rCgenBD(m,i)>0 %total C gen (CO* + CH* + BD)
        LOG10rCgenBD(m,i) = log10(rCgenBD(m,i));
end
if rCremBD(m,i)>0 %total C rem (O* + H* + RBD)
        LOG10rCremBD(m,i) = log10(rCremBD(m,i));
end
if rBD(m,i)>0
        LOG10rBDrev(m,i) = log10(rBDrev(m,i));
end
if rRBD(m,i)>0
        LOG10rRBDrev(m,i) = log10(rRBDrev(m,i));
end
if rBD(m,i)>0
        LOG10rBD(m,i) = log10(rBD(m,i));
end
if rRBD(m,i)>0
        LOG10rRBD(m,i) = log10(rRBD(m,i));
end
if rCO2(m,i)>0
        LOG10rCO2(m,i) = log10(rCO2(m,i));
        LOG10_rCO2(m,i) = -100;
end
if Ansr1(m,i)>0
    LOG10r1(m,i) = log10(Ansr1(m,i));
```

```
        LOG10r_1(m,i) = -100;
end
if Ansr2(m,i)>0
        LOG10r2(m,i) = log10(Ansr2(m,i));
        LOG10r_2(m,i) = -100;
end
if Ansr3(m,i)>0
        LOG10r3(m,i) = log10(Ansr3(m,i));
        LOG10r_3(m,i) = -100;
end
if Ansr4(m,i)>0
        LOG10r4(m,i) = log10(Ansr4(m,i));
        LOG10r_4(m,i) = -100;
end
if Ansr5(m,i)>0
        LOG10r5(m,i) = log10(Ansr5(m,i));
        LOG10r_5(m,i) = -100;
end
if Ansr6(m,i)>0
        LOG10r6(m,i) = log10(Ansr6(m,i));
        LOG10r_6(m,i) = -100;
end
if rCtotBD(m,i)>0%more C removal
        LOG10rCremtotBD(m,i) = log10(rCtotBD(m,i));
        LOG10rCgentotBD(m,i) = -100;
end
if Ansr_4(m,i)>0
        LOG10r_4(m,i) = log10(Ansr_4(m,i));
end
if Ansr_6(m,i)>0
        LOG10r_6(m,i) = log10(Ansr_6(m,i));
```

```matlab
end
if rDRR(m,i)>0
        LOG10rDRR(m,i) = log10(rDRR(m,i));
end
% This is the individual step to generate/remove coke
if rCgenCH(m,i)>0
        LOG10rCgenCH(m,i) = log10(rCgenCH(m,i));
end
if rCgenCO(m,i)>0
        LOG10rCgenCO(m,i) = log10(rCgenCO(m,i));
end
if rCremH(m,i)>0
        LOG10rCremH(m,i) = log10(rCremH(m,i));
end
if rCremO(m,i)>0
        LOG10rCremO(m,i) = log10(rCremO(m,i));
end
% this is to eliminate negative rate
if rDRR(m,i)<0
        LOG10rDRR(m,i) = -100;
end
if rCgenBD(m,i)<0 %total C gen (CO* + CH* + BD)
        LOG10rCgenBD(m,i) = -100;
end
if rCremBD(m,i)<0 %total C rem (O* + H* + RBD)
        LOG10rCremBD(m,i) = -100;
end
if rBD(m,i)<0
        LOG10rBD(m,i) = -100;
end
if rRBD(m,i)<0
```

```matlab
        LOG10rRBD(m,i) = -100;
end
if rCH4(m,i)<0
        LOG10rCH4(m,i) = -100;
        LOG10_rCH4(m,i) = log10(-rCH4(m,i));
end
if Ansr1(m,i)<0
        LOG10r1(m,i) = -100;
        LOG10r_1(m,i) = log10(-Ansr1(m,i));
end
if Ansr2(m,i)<0
        LOG10r2(m,i) = -100;
        LOG10r_2(m,i) = log10(-Ansr2(m,i));
end
if Ansr3(m,i)<0
        LOG10r3(m,i) = -100;
        LOG10r_3(m,i) = log10(-Ansr3(m,i));
end
if Ansr4(m,i)<0
        LOG10r4(m,i) = -100;
        LOG10r_4(m,i) = log10(-Ansr4(m,i));
end
if Ansr5(m,i)<0
        LOG10r5(m,i) = -100;
        LOG10r_5(m,i) = log10(-Ansr5(m,i));
end
if Ansr6(m,i)<0
        LOG10r6(m,i) = -100;
        LOG10r_6(m,i) = log10(-Ansr6(m,i));
end
if rAll(m,i)<0
```

```matlab
            LOG10rAll(m,i) = -100;
    end
    if rCgen(m,i)<0
            LOG10rCgen(m,i) = -100;
    end
    if rCrem(m,i)<0
            LOG10rCrem(m,i) = -100;
    end
    if rCtotBD(m,i)<0 %more C formation
            LOG10rCremtotBD(m,i) = -100;
            LOG10rCgentotBD(m,i) = log10(abs(rCtotBD(m,i)));
    end
    % This is the individual step to generate/remove coke
    if rCgenCH(m,i)<0
            LOG10rCgenCH(m,i) = -100;
    end
    if rCgenCO(m,i)<0
            LOG10rCgenCO(m,i) = -100;
    end
    if rCremH(m,i)<0
            LOG10rCremH(m,i) = -100;
    end
    if rCremO(m,i)<0
            LOG10rCremO(m,i) = -100;
    end
        end %end of RT-S loop
end %end of RT-R loop
```

APPENDIX G

VITA

Mr. Supareak Praserthdam graduated *summa cum laude* from Chulalongkorn University, Bangkok, Thailand, with a Bachelor of Engineering (Chemical Engineering) in 2014. He started his Ph.D. program in chemical engineering at the Artie McFerrin Department of Chemical Engineering, Texas A&M University, College Station, Texas, USA under the supervision of professor Perla B. Balbuena in Fall 2014. His research focuses on the utilization of computational techniques such as density functional theory (DFT) in the field of catalysis. The research includes electrocatalysis, Zeolites and metal supported catalysts for methane utilization and the development of the ratings concept as a catalyst performance evaluation tool used in the dry reforming reaction of methane (DRR). He obtained his Ph.D. in chemical engineering from Texas A&M University in August 2018.

Mr. Praserthdam can be reached at Jack E. Brown Engineering building, 3122 TAMU Room 632, College Station, TX 77843-3122. His email addresses are sigmasup47124@tamu.edu and sigmaupsilonpi@hotmail.com. In addition, his homepage is https://sigmaupsilonpi.wixsite.com/supcatalyst.

Permanent address: 154, Soi. Chareonakorn 28, Chareonakorn road, Klongsan district,
Bangkok 10600, Thailand